

UNIVERSITY OF CAPE TOWN

DOCTORAL THESIS

Monte Carlo simulation of slot-scanning
X-ray imaging systems

Author:
Mayuresh KULKARNI

Supervisor:
Prof. Tania S. DOUGLAS
Co-supervisor:
Assoc. Prof. Fred NICOLLS

A thesis presented for the degree of
DOCTOR OF PHILOSOPHY
in the

Division of Biomedical Engineering
Department of Human Biology
University of Cape Town

February 2015

Declaration of Authorship

I, Mayuresh KULKARNI, declare that this thesis titled, ‘Monte Carlo simulation of slot-scanning X-ray imaging systems’ and the work presented in it are my own. I confirm that:

- This work was done wholly or mainly while in candidature for a research degree at this University.
- Where any part of this thesis has previously been submitted for a degree or any other qualification at this University or any other institution, this has been clearly stated.
- Where I have consulted the published work of others, this is always clearly attributed. Where I have quoted from the work of others, the source is always given. With the exception of such quotations, this thesis is entirely my own work.
- I have acknowledged all main sources of help.
- Where the thesis is based on work done by myself jointly with others, I have made clear exactly what was done by others and what I have contributed myself.

I, Mayuresh KULKARNI, hereby declare that the work on which this thesis is based is my original work (except where acknowledgements indicate otherwise) and that neither the whole work nor any part of it has been, is being, or is to be submitted for another degree in this or any other university. I authorise the University to reproduce for the purpose of research either the whole or any portion of the contents in any manner whatsoever.

Signed:

Date:

“It always seems impossible until it is done.”

Nelson Mandela

Abstract

Monte Carlo simulation of slot-scanning X-ray imaging systems

by Mayuresh KULKARNI

This thesis presents simulation of slot-scanning X-ray systems using the general-purpose Monte Carlo simulation package PENELOPE and penEasy_Imaging. Different phantoms can be defined with the help of the PENGEOM package, which defines bodies as combinations of volumes limited by quadric surfaces. The source-detector geometry and the position of the object with respect to the system is defined for the slot-scanning imaging system, which also motivates the collimation used, the X-ray tube properties and the detector material and resolution. The output of the time-delay integration (TDI) detector is simulated using sequential slot outputs derived from penEasy_Imaging.

A full-body slot-scanning X-ray imaging system is simulated based on the parameters in the imaging chain. The applications of the simulation system to scatter reduction techniques and filtration are described. The effects of slot-width on scatter-to-primary ratio and different thicknesses of filtration on image quality are studied. A tissue-equivalent three-dimensional breast phantom is simulated using a slot-scanning digital mammography system. The breast phantom is also used for simulating digital breast tomosynthesis using angular width, angular interval and number of projections. Filtered back-projection is used to reconstruct planar slices from the projections. The effect of tomosynthesis parameters on the reconstructed slices is investigated.

The simulations are validated using tungsten test objects, which are both simulated and imaged. The simulations are compared to X-ray images using standard image quality metrics namely MTF, NPS and DQE. The comparison of real and simulated X-ray images shows that this simulation process may be used to represent, analyse and compare the output of physical X-ray imaging systems. The implementation of the simulation can be modified to simulate a wide range of slot-scanning X-ray imaging systems.

Acknowledgements

This thesis is the result of nearly four years of work at the Medical Imaging Research Unit (MIRU) and the Digital Image Processing (DIP) lab at the University of Cape Town. I would like to thank many people who have helped and supported me during these years.

Firstly, I would like to thank my supervisors, Tania Douglas and Fred Nicolls, for their help and guidance at every stage of this project. Thank you for your patience and time. I cannot forget the long discussions and debates with Stef Steiner, from whom I have learnt a lot about the Lodox Statscan and slot-scanning imaging in general. Contributions, via email, from Andreu Badal-Soler and Josep Sempau were very important in helping me understand the workings of the PENELOPE and penEasy_Imaging programs.

The love and support received from friends and family was equally important. Special thanks to Tejashree Phadke for supporting me through many tough times. I would also like to thank my parents for their help and motivation. I am indebted to Mark Ferris for his special brand of ‘support’, Nicole Ferris for the best date pudding in the world and Elizabeth Ferris for always making me smile. The coffee breaks spent with Mark Pikker and Sello Phetla were priceless.

Finally, I gratefully acknowledge the financial support I have received from CapeRay Medical (Pty) Ltd, Lodox Systems, the Technology and Human Resources for Industry Programme (THRIP) of the South African National Research Foundation (NRF) and the Cancer Association of South African (CANSA).

Contents

Declaration of Authorship	i
Abstract	iii
Acknowledgements	iv
Contents	v
List of Figures	viii
Abbreviations	xiii
1 Introduction	1
1.1 Project purpose and scope	1
1.2 Objectives	3
1.3 Document Overview	4
2 Background	6
2.1 X-ray source simulation	6
2.2 X-ray transport simulation	7
2.2.1 Monte Carlo simulation tools	8
2.3 Simulation of slot-scanning X-ray systems	11
2.4 Image quality metrics	12
2.4.1 Region-based metrics	12
2.4.2 System-based metrics	12
2.4.3 Image contrast and CNR	13
2.4.4 Modulation Transfer Function, Noise Power Spectra and Detective Quantum Efficiency	13
2.5 Mammography and Digital Breast Tomosynthesis	15
2.6 Summary	20
3 Simulation tools: PENELOPE and penEasy	21
3.1 Introduction	21
3.2 Geometry	23
3.3 Material properties	25

3.4	Source Models	25
3.5	Detector Models	26
3.6	Scattered Radiation	26
3.7	Tallies	27
3.8	Summary	29
4	System requirements for Linear Slot-Scanning X-ray imaging	30
4.1	System design and requirements	31
4.1.1	Mechanical design	31
4.1.2	X-ray tube	32
4.1.3	Detector specifications	32
4.1.4	Time delay integration mode	33
4.2	Modelling the imaging system and its performance	33
4.2.1	Geometric definitions	34
4.2.2	X-ray detector simulation	36
4.2.3	Imaging task	37
4.3	A sample simulation	38
4.3.1	X-ray energy spectrum definition	38
4.3.2	Geometric definitions	38
4.3.3	Material properties	39
4.3.4	Input file definitions	40
4.3.5	Simulation results	42
4.4	Summary	44
5	Simulating a slot-scanning X-ray imaging system	45
5.1	Lodox Statscan: System parameters	45
5.2	Test objects	47
5.3	Modification of penEasy_Imaging code	48
5.4	Image quality metrics	49
5.4.1	System resolution MTF	49
5.4.2	Noise Power Spectrum	50
5.4.3	Detective Quantum Efficiency	52
5.5	Results and validation	53
5.6	Discussion	56
5.7	Summary	57
6	Applications of slot-scanning simulation	58
6.1	Scatter reduction techniques	58
6.1.1	Background	59
6.1.2	Methodology	61
6.1.3	Results	61
6.1.4	Discussion	64
6.2	Filtration	65
6.2.1	Background	65
6.2.2	Methodology	67
6.2.3	Results	67
6.2.4	Discussion	69

7	Simulating a breast phantom on a slot-scanning digital mammography system	71
7.1	System parameters	71
7.2	Phantom definition	73
7.3	Modification of penEasy_Imaging code	75
7.4	Results and validation	76
7.5	Discussion	81
7.6	Summary	82
8	Simulating digital breast tomosynthesis	83
8.1	Simulating digital breast tomosynthesis	83
8.2	Results	85
8.3	Discussion	90
8.4	Summary	91
9	Conclusions and Recommendations	92
	References	93
A	Program structure for slot-scanning X-ray imaging	101
A.1	Description of files	101
A.1.1	Input energy spectrum file	101
A.1.2	Geometry (*.geo) file	102
A.1.3	Material (*.mat) data file	102
A.1.4	Input (*.in) file	102
A.1.5	Output (*.out) file	102
A.1.6	Image (*.dat) file	103
A.1.7	Dose distribution file	103
A.2	Modifications to the program structure	103
A.3	Parallelisation of the simulation process	105
B	PENELOPE, PENGEO and penEasy_Imaging programs	106
B.1	Input energy spectrum file	106
B.2	Geometry file	107
B.3	Material file	109
B.4	Input and Output files	110
B.5	Image file	112

List of Figures

3.1	Graphical representation of the quadric surfaces used in PENGEOM in reduced form (image taken from the PENELOPE manual (Salvat et al., 2006)).	24
3.2	Basic interactions of photons with matter causing scattered radiation ((Salvat et al., 2006)).	27
4.1	The differences in the geometries of a full-field digital radiographic system on the left and a slot-scanning system on the right. The effects of collimation and the narrow fan beam on the detector and the exposed patient volume are shown, adapted from (Irving et al., 2008).	31
4.2	A typical slot-scanning X-ray system. SDD is the source-to-detector distance, CDD is the collimator to detector distance and x is the thickness of the object to be scanned. The width of the collimator is C_w and the beam-width at the detector is B_w . The slot direction is coming out of the page and the scan direction is from left to right on the page.	32
4.3	TDI detector operation, with two consecutive slots shown in top view and front view. The beam-width, B_w , is also the width of the slot. The step is the space between the beginning of two slots. The detector output is an integration of the slots. The beam width and the step are shown in the top and front view.	34
4.4	A block diagram of the simulation process using PENELOPE, PENGEOM and penEasy_Imaging.	35
4.5	Examples of two X-ray spectra from a 90kV source (the continuous line) and a 28kV source (the dotted line) simulated using methods presented by (Poludniowski et al., 2009).	37
4.6	Coefficients of a 90kV energy spectrum simulated using methods presented by (Poludniowski et al., 2009).	39
4.7	The geometric definitions of the surfaces to form the square object. Each surface is given a thickness and an identification number.	40
4.8	The surfaces shown in Figure 4.7 are used to form the square test object. The material assigned is ‘2’ which is the second material in the material file. A list of all modules and surfaces is provided at the end of the file.	41
4.9	An example of the materials in the material definition file.	42
4.10	A sample simulation using two test objects and two slots covering the detector. Two overlapping slots are shown in (A) and (B).	43
4.11	A sample simulation using two test objects and four slots covering the detector. Four overlapping slots are shown in (A), (B), (C) and (D)	43
4.12	Locations of overlapping slots with 2 slots in (A) and 4 slots in (B). The combination of averaging of data is shown in (C).	43

5.1	The Lodox Statscan machine at the UCT Faculty of Health Sciences. . . .	46
5.2	The components of a slot-scanning X-ray detector with the scintillator, fibre optic taper and CCD. Picture taken from (Mohajer, 2012).	47
5.3	The test objects used for simulation and validation of X-ray images using the Lodox Statscan. The aluminium step wedge (left) has 5 blocks of aluminium with thicknesses of 1mm, 2mm, 3mm, 4mm and 5mm. The 3mm tungsten block (right) is placed at an angle to the detector for the calculation of DQE. Both test objects are visualised using <i>gview2d</i>	48
5.4	Examples of two imaged slots at different locations on the detector. The images have been inverted, each pixel value in the image has been subtracted from 1, for the ease of viewing.	49
5.5	The calculation of the edge spread function (ESF). The angle ϕ is between 0 and 5 degrees.	50
5.6	The simulated X-ray image of the tungsten test object in (A) and the edge spread function in (B).	51
5.7	The line spread function in (A) and then modulation transfer function in (B).	51
5.8	An example of three partially overlapping pixel regions, in a uniformly exposed region, is shown in (A). Squares overlap by half a square in both directions. Three of the squares are shown by thick lines. For each square the noise power spectrum is determined; averaging these spectra yields a smooth spectrum. The 1D window functions that can be used to avoid frequency leakage for $N = 16$ are shown in (B). Hamming (blue), Bartlett (green), Blackman (red) and triangular (black) windows are shown.	52
5.9	A sample NPS curve shown in (A) and a sample DQE curve shown in (B). 53	53
5.10	The simulated (top) and real (bottom) X-ray images of the (A) aluminium and (B) tungsten test objects. The tungsten test object is at a slight angle (less than 2 degrees) to the detector for the DQE calculation.	54
5.11	The image contrast and contrast-to-noise ratio for real (circles) and simulated (squares) X-ray images of the the aluminium test object using Equations 2.1 and 2.2.	54
5.12	The MTF and the NPS of the real (continuous line) and simulated (dashed line) X-ray images.	55
5.13	The DQE of the real (continuous line) and simulated (dashed line) X-ray images.	56
6.1	The effects of the depth of the post-collimator slot h and slot width w on scattered radiation. The red and blue lines show the scattered photons, outside and inside of the slot respectively, and the top-view shows where these photons landed using red and blue squares. The green lines and squares are the paths and locations of photons if there was no scatter. The black dot is placed in the top and front views for reference.	60
6.2	An example of a graph showing the relation between slot-width and SPR, drawn by (Hussein, 2008) (page 38) based on (Boone et al., 2000, Jing et al., 1998).	61
6.3	A 3mm tungsten block is simulated with and without the use of scatter reduction techniques. The image with scattered radiation (left) has blurry edges compared to the image with reduced scattered radiation (right). . .	62

6.4	(A) The contributions of the different types of scatter at 90kV including Rayleigh scattering (red), Compton scattering (blue), multi-scatter (green) and secondary scattering (black) plotted against increasing slot width (in mm). The scatter-to-primary ratio versus the increasing slot width is shown in (B).	62
6.5	The contributions of Rayleigh scattering in (A) and secondary scattering in (B) in the X-ray image. These images are for one slot, 0.5mm wide with the 3mm tungsten block as the object being imaged.	63
6.6	The contributions of multiple scattering in (A) and Compton scattering in (B) in the X-ray image. These images are for one slot, 0.5mm wide with the 3mm tungsten block as the object being imaged.	63
6.7	The X-ray image with no scattered radiation in (A), and only primary radiation and the X-ray image containing primary and scattered radiation in (B). These images are for one slot, 0.5mm wide with the 3mm tungsten block as the object being imaged.	64
6.8	The changes in the X-ray energy spectrum due to the different filters. The low energy photons are filtered out to reduce dose.	68
6.9	The modulation transfer function, shown in (A), calculated for different thicknesses of Al filters. The amplitude of the MTF decreases with an increase in the thickness, but the frequency characteristics are retained. The noise power spectrum, shown in (B), averaged over 200 overlapping sub-images. A Bartlett window is used to avoid frequency leakage and the DC offset has been excluded.	69
6.10	The detective quantum efficiency, for the different filters calculated using the MTF and the NPS. The DQE is normalised to compare the filtered image DQEs with the unfiltered image DQE.	69
7.1	The CapeRay Soteria mammography machine.	72
7.2	A simple schematic diagram of a slot-scanning mammography system. The X-ray source is collimated to create a slot on the detector, the grey region. The slot direction is coming out of the page and the scan direct is from right to left on the page. The object, a breast or a breast phantom, is compressed to improve the image quality.	73
7.3	The mathematical tissue-equivalent phantom for digital mammography. Areas within the phantom simulating (1) 100% glandular, 70:30 glandular/adipose, 50:50 glandular/ adipose, 30:70 glandular/adipose, and 100% adipose tissues. (2) four spheric regions simulating 70:30 glandular/adipose tissue; (3)nylon fibres of different size; (4) microcalcifications of different sizes (CaCO_3); (5) line pair tools for measuring the system resolution.	74
7.4	The tissue-equivalent phantom used simulation, viewed using <i>gview2d</i> . The different colours are used to visualise different components of the model.	75
7.5	Examples of two imaged slots at different locations on the detector. The images have been inverted for the ease of viewing.	76
7.6	The simulated image of the tissue-equivalent breast phantom. All the components are visible and their positions and orientations are correctly simulated. The image displays raw, unprocessed data.	77

7.7	The location, orientation and thickness of the Nylon fibres is correctly simulated. The image displays raw, unprocessed data.	78
7.8	The spheric masses with the same material properties but different diameters are simulated correctly in (A). The CaCO_3 specks are also clearly visible in (B). The image displays raw, unprocessed data.	78
7.9	The simulation of the line pair tool showing the difference between the edges in two directions. The image displays raw, unprocessed data.	79
7.10	The edge spread functions (ESF) in (A) and the line spread functions (LSF) in (B) of the real (continuous) and simulated (dashed) X-ray images. These functions are based on experiments done using a 3mm tungsten block and the edge-test method.	80
7.11	The modulation transfer functions (MTF) in (A) and the detective quantum efficiencies (DQE) in (B) of the real (continuous) and simulated (dashed) X-ray images. These functions are based on experiments done using a 3mm tungsten block and the edge-test method.	80
8.1	A simple schematic of the DBT system. The angular width is θ and the angular interval is ϕ . In case of a slot-scanning system, the source is collimated and its projection is made up of many slots, as shown in Figure 4.2.	84
8.2	The horizontal (dashed line) and vertical (dotted line) planar reconstructions shown with respect to the test object and source. The planar reconstructions are named with respect to the detector. The source is shown to provide context to the orientation of the object, and its location is not drawn to scale.	86
8.3	Some of the angular projections of the tungsten block. Simulations are done from 0 to 180 degrees from the detector. The projections shown in the images are (A) 90, (B) 105, (C) 120, (D) 135, (E) 140, (F) 150, (G) 165 and (H) 180 degrees.	86
8.4	Reconstructions of vertical slices through the center of the tungsten block. The three reconstructions are performed using data from different angular intervals. The angular range is from 0 to 180 degrees and the intervals are (A) 2, (B) 5 and (C) 10 degrees.	87
8.5	The top view or 90 degree projection in (A) and a horizontal planar reconstruction using filtered backprojection in (B).	87
8.6	Projections shown in the images are (A) 92, (B) 98, (C) 104, (D) 88, (E) 82 and (F) 76 degrees with respect to the detector.	88
8.7	The horizontal planar slices at different depths.	89
8.8	Horizontal planar reconstructions using filtered backprojection over angular ranges of 70 to 110 degrees in (A) and (C) and 80 to 100 degrees in (B) and (D). The angular intervals used are 2 degrees in (A) and (B) and 4 degrees in (C) and (D).	89
B.1	The columns in the input energy spectrum file for a 28 kVp spectrum (Mo anode with 0.03 mm Mo filtration). The columns are rearranged for ease of viewing.	107
B.2	The X-ray energy spectrum generated using the input energy spectrum file for a 28 kVp spectrum (Mo anode with 0.03 mm Mo filtration).	108
B.3	Geometric definition of the six planar surfaces forming the detector layer.	109

B.4	Geometric definition of the detector layer module using the planar surfaces shown in Figure B.3. The X, Y, Z shifts define the position of the module in the geometry and omega, theta and phi are used to change the angles.	109
B.5	The listing of all the modules and surfaces at the end of the geometry file. The detector layer, module number 2, is included along with other modules and surfaces that have not been assigned to modules.	110
B.6	A part of the material file showing the material properties of Cesium Iodide (CsI).	111
B.7	The description of the configuration section.	112
B.8	The description of the X-ray source section.	112
B.9	The description of the PENGEOM section.	112
B.10	The description of the material section.	112

Abbreviations

PENELOPE	PEN etration and E nergy L oss of P ositrons and E lectrons
MC	M onte C arlo
TDI	T ime D elay I ntegration
CCD	C harge C ouple D evice
DQE	D etective Q uantum E fficiency
MTF	M odulation T ransfer F unction
CNR	C ontrast-to- N oise R atio
SNR	S ignal-to- N oise R atio
NPS	N oise P ower S pectrum
FFDM	F ull F ield D igital M ammography
DBT	D igital B reast T omosynthesis
SPR	S catter-to- P rimary R atio

*In memory of
Digambar and Chinmay Kulkarni*

Chapter 1

Introduction

This chapter provides a brief introduction to topics related to the work done in this thesis. Monte Carlo methods, slot-scanning radiography, full field digital mammography and digital breast tomosynthesis are discussed. The purpose and scope are presented in Section 1.1, objectives of the work are outlined in Section 1.2 and the document structure for this report is described in Section 1.3.

1.1 Project purpose and scope

Computer simulations are useful tools for the design and optimisation of digital X-ray imaging systems. They also allow the testing and comparison of different X-ray imaging systems and geometries without the need to build prototypes, which saves time and money.

The simulation of X-ray images can be formulated as a radiation transport problem, tracking X-ray photon paths as they pass through matter. Radiation transport through matter has been a subject for research since the 1900s and was initially based on the Boltzmann transport equation. This problem formulation is limited to simple geometries, giving errors when applied to complex phantoms and geometries (Zheng-Ming and Brahme, 1993). Computer simulations are useful tools to describe the radiation transport problem in general, and the X-ray radiation transport problem in the context of this thesis. X-ray simulations can be used to study a wide range of medical applications (eg. mammography, full-body X-rays, tomosynthesis, etc.), they are inexpensive and

can be useful to estimate information that would be very difficult, or even impossible, to measure experimentally (eg. scattered radiation, 3D fluence maps, etc.). They can be used to perform exploratory studies while selecting operating variables in new X-ray imaging systems or to improve existing systems. With the advancement in computer technology, Monte Carlo methods were developed as alternatives to solve the radiation transport problem. These methods are based on the use of random numbers, and the Monte Carlo simulation of the X-ray transport problem consists of the generation of random photon showers and histories, tracking of photon interactions and placing large photon samples in generated images. There are many Monte Carlo implementations for X-ray transport problems; PENELOPE is the one used in this thesis.

Linear slot-scanning radiography (LSSR) is a method of taking X-ray images using an X-ray source and detector combination that moves across a patient during image acquisition. The X-ray source beam is collimated using a narrow slot, resulting in a fan beam that passes through the patient and is received at the detector, rather than a cone beam used in conventional radiography. As the X-ray source and detector move across the patient, the fan beam produces slots of image data at the detector. These slots are combined to form the final X-ray image of the patient. This slot-scanning imaging technique produces low scattered radiation and reduces radiation dose in patients (Irving et al., 2008).

Several models have been developed to aid the design and optimisation of X-ray imaging systems, but they either only simulate parts of the imaging chain like the X-ray energy spectrum (Poludniowski et al., 2009, Rogers et al., 2004) and scattered radiation (Boone et al., 2000, Jing et al., 1998), or are not sufficiently flexible to simulate different phantoms and X-ray imaging systems (Freud et al., 2000, Viswanathan and Balasubramaniam, 2009). Furthermore, very few simulation methods are available for slot-scanning imaging systems, and those that exist are application specific and limited in their use. Thus a flexible and multi-purpose simulation system for slot-scanning X-ray imaging systems is required.

Full-field digital mammography (FFDM) takes X-ray images of the breast by compressing it using compression paddles for the detection of breast cancer. A slot-scanning

mammography system uses a fan beam instead of a cone beam. Digital breast tomosynthesis creates three-dimensional volumetric reconstructions of the breast based on two-dimensional X-ray projections taken at different angles. DBT is used along with digital mammography and has the potential to improve cancer detection and reduce the number of biopsies (Helvie, 2010). Although initial DBT studies are positive and support the use of DBT, further investigations are necessary to study this new modality in detail. A simulation tool that simulates a comprehensive set of the mammography and DBT parameters using three-dimensional geometry would aid such studies.

The purpose of the project presented in this thesis was to develop an accurate, flexible, easy-to-use and general-purpose simulation system for slot-scanning X-ray imaging systems. The following requirements were considered in the design of the simulation tool: the simulation of X-ray photon physics, modularity to enable easy of use, flexibility and adaptation for different applications and three dimensional capability to accommodate the simulation of DBT.

The simulation system was validated by comparing simulated and real X-ray images using standard image quality metrics. This quantitative validation provides an objective assessment of image quality.

1.2 Objectives

The aim of the project was to develop modelling and simulation tools for slot-scanning X-ray imaging systems. The objectives were:

- to simulate and validate X-ray images from a slot-scanning X-ray imaging system,
- to apply the simulation process to common X-ray imaging modifications to demonstrate its use,
- to simulate and validate a three-dimensional, tissue-equivalent breast phantom using a mammography system,
- to simulate digital breast tomosynthesis and to study the effect of tomosynthesis parameters on the resulting reconstructions, and

- to provide a user-friendly and flexible framework for further experiments and simulations in slot-scanning imaging.

1.3 Document Overview

Chapter 2 provides a review of the relevant literature and defines image quality parameters. Previous work done in the field of Monte Carlo simulation, X-ray imaging simulation, mammography and tomosynthesis is presented.

PENELOPE, with its subroutines and improvements, is described in Chapter 3. The different components of the simulation namely source, detector models, materials and geometric set up are discussed. Previous work using the PENELOPE package is reviewed.

Linear slot-scanning X-ray imaging systems are described in Chapter 4. The individual components of the imaging chain are listed and the imaging task is introduced. The parameters required for modelling slot-scanning imaging systems are also described in this chapter.

Chapter 5 discusses the simulation of the Lodox Statscan, a full-body X-ray imaging system. The system parameters that define the X-ray system are noted and the simulation process is formulated accordingly. Simulated X-ray images are validated using real X-ray images and different image quality measures.

Two applications of the simulation process are explored in Chapter 6. The effects of slot-width on scattered radiation and filter thickness on image quality are studied.

Digital Mammography is simulated in Chapter 7. A tissue-equivalent breast phantom is simulated and a 3D mathematical model of the phantom is defined. The simulations from the new system are validated using standard image quality metrics.

Chapter 8 describes the application of the simulation system to digital breast tomosynthesis (DBT). DBT parameters angular width, angular interval and number of projections are varied and their effects on the final reconstructions are studied.

Chapter 9 presents conclusions and recommendations for future work.

The details of the workings of PENELOPE, penEasy Imaging and PENGEOM are discussed in Appendices A and B.

Chapter 2

Background

This chapter reviews the literature relevant to the work done in this thesis. Previous work done in the simulation of X-ray images is discussed and the literature on simulating components of the imaging chain is also presented. Image quality metrics, used to compare real and simulated X-ray images for validation, are defined in this chapter. A review of investigations performed to study mammography and tomosynthesis is also provided. The previous work related to X-ray source and transport simulation is presented in Section 2.1 and 2.2. The simulation of slot-scanning X-ray systems is discussed in Section 2.3, image quality metrics are described in Section 2.4 and an overview of the previous work done related to mammography and tomosynthesis is presented in Section 2.5.

2.1 X-ray source simulation

Inside the X-ray tube, an electron beam is directed to a focal point on a metal (generally tungsten, rhodium or molybdenum) anode that produces emissions that constitute the energy spectra. As the electron beam penetrates the target, the electrons scatter from the nuclei in the target resulting in Bremsstrahlung and characteristic emissions. The angle of the target in relation to the anode can give rise to a directional distribution of X-rays. This directional distribution results in a distorted fan beam shape for the radiation, and is called the anode heel effect. There have been various methods of measuring, calculating and simulating X-ray spectra. Measured spectra are parameterised

using polynomial interpolations by Boone (1997) based on the physical measurements of energy spectra made by Fewell and Shuping (1978). SpekCalc (Poludniowski et al., 2009), a program for calculating X-ray spectra from tungsten anodes, uses deterministic equations for Bremsstrahlung combined with pre-calculated electron distributions. Poludniowski et al. (2009) compared results from SpekCalc to the X-ray energy spectrum estimations using two other simulation methods, namely BEAMnrc (Rogers et al., 2004) and (Cranley et al., 1997). The results were observed to be similar.

2.2 X-ray transport simulation

Radiation transport through matter has been widely studied since the 1900s (Salvat et al., 2006). High-energy electrons, positrons and photons penetrating through matter are subjected to various interactions which produce other particles. Each interaction reduces the energy of the penetrating particles and the flight path of the particles, often called a shower, represents the energy degradation.

Interaction models are build to track the interactions of X-ray photons in the random histories. These photon histories, also known as cross sections, define the probability distribution functions that parameterise a track. More random histories can be generated based on the probability distribution functions. Using sampling methods and a large sample size for the generated histories, the quantitative information of the transport process can be obtained. This information, in the case of the X-ray photon transport problem, is the information of the destinations of the photons which results in the formation of the X-ray image.

X-ray simulation entails tracking the paths of X-ray photons from the source, through the test object to the detector, and is essentially a radiation transport problem. Computer simulations are useful tools to describe the latter (Badal-Soler, 2008). The Boltzmann equation was initially used to study radiation transport problems, but it had considerable limitations for simple geometries (Salvat et al., 2006, Zheng-Ming and Brahme, 1993). In the early 1960s, with computing advances, Monte Carlo (MC) simulations developed as a powerful tool for radiation transport problems. Several MC implementations are available, such as ETRAN (Berger and Seltzer, 1988), ITS3 (Halbleib et al.,

1992), EGS4 (Nelson et al., 1985), EGS5 (Hirayama et al., 2005), GEANT3 (Brun et al., 1986), GEANT4 (Agostinelli et al., 2003, 2006) and others. These simulation procedures are categorised as ‘condensed’ MC methods (Bielajew and Rogers, 1986), because they are approximations and can result in systematic errors (Berger, 1963).

2.2.1 Monte Carlo simulation tools

ITS3 (Halbleib et al., 1992) was the third iteration of the ITS software, which was a Monte Carlo solution for the photon radiation transport problems. ITS3 modelled the production and transport of photons through matter based on the model described in (Berger and Seltzer, 1988). ITS3 also solved the electron transport problem, combining both electrons and photons as part of the simulation. The primary (unscattered) photons, scattered photons and leakage radiation were tracked. The photon and electron energy deposition profiles could be plotted. Despite being an improvement on the simulation methods that preceded it, ITS3 was fairly basic and had its limitations. The model only accommodated 100 elements and complex material properties were difficult to model. There were limitations on the geometry used for simulation as the model concentrated on photon transport and not system geometry. Furthermore, the simulation system was not specifically designed for X-ray imaging so it lacked the basic components of such a system, like the detector.

EGS4 (Nelson et al., 1985) and EGS5 (Hirayama et al., 2005) were the 4th and 5th iterations of the Electron-Gamma Shower (EGS) code system. EGS4 extended EGS3 by including low-energy radiation transport, which was already covered by ETRAN (Berger and Seltzer, 1988). A few notable updates in EGS4 were the inclusion of scattering models like Rayleigh scattering and improved geometric packages. EGS5, the 5th version of the code, added a Compton scattering model and updated the photon physics to model photon transport and behaviour more accurately. A new random number generator was implemented to improve the performance of Monte Carlo methods. The EGS code system is limited in terms of geometry and it is difficult to simulate a large number of photon showers using EGS (Salvat et al., 2006). Furthermore, the EGS system was not designed specifically for X-ray imaging simulation so it lacks features like X-ray imaging geometry and components like X-ray source and detectors. This makes the code system less useful compared with other systems that can be modified easily for

X-ray imaging.

GEANT3 and GEANT4, iterations of the GEometry ANd Tracking platform, are improvements that simulate the passage of particles (electrons, positrons and photons) through matter. The features of the platform include geometry, tracking and detection of particles. The geometry is flexible so it can analyse the physical layout of detectors and sources. and can simulate the way they affect the photon path. Tracking involves collision libraries and subroutines to simulate the interaction of the particles as they pass through matter. GEANT4 also implements procedures to improve the efficiency of the code using parallel programming. An expert-level knowledge of C++ is needed to run GEANT4 and the installation of the system requires more than basic computer skills. This is a limiting factor in the use of GEANT4 (Salvat et al., 2006).

Bottigli et al. (2004) describe a Monte Carlo based simulation method for X-ray imaging and spectroscopy experiments performed on samples defined on a three-dimensional grid. The grid consisted of three-dimensional voxels whose mass density and chemical composition could be set. Radiation transport effects like photoelectric absorption, fluorescent emission, and Rayleigh and Compton scattering models were included in the code. The flight paths of each photon shower were simulated from a source to a detector. The starting position, orientation and energy of each simulated photon was generated randomly based on X-ray source definition files. The code was considered to be unreliable for energies above 100keV and was not tested below the energy level of 1keV. Some basic testing showed that the simulated tool could be used for X-ray imaging and spectroscopy experiments, but a thorough validation was not performed.

Golosio et al. (2014) improved the efficiency of the code system introduced by (Bottigli et al., 2004) by using variance reduction techniques and Monte Carlo simulations. The XRMC program, presented in (Golosio et al., 2014), extends the implementation in (Bottigli et al., 2004) to quadric surfaces instead of voxels. The use of surfaces improves the execution time of the program and reduces the voxel definitions needed by (Bottigli et al., 2004). The X-ray imaging geometry is well defined because of the use of quadric surfaces and material properties are assigned to each surface. The material properties consist of the mass density and the elemental composition of a given surface. It is noted that XRMC does not simulate the output of real detectors and post-processing of the

data may be required to achieve this. XRMC also lacks support and the code system is not documented thoroughly, making it difficult to learn and use.

PENELOPE (Salvat et al., 2006), developed and maintained by the Nuclear Energy Agency since 1996, is a Monte Carlo simulation code system used for modelling the particle transport problem. The essential components like a flexible geometry, photon scattering models, material databases and particle interaction models were included over the years by updating and modifying the code system. Extensions presented in (Badal et al., 2009) and (Badal-Soler, 2008) increased the functionality of PENELOPE to include X-ray sources, use triangular meshes to improve the geometric descriptions of objects and produce X-ray image simulations. The modular nature of the code system makes it easy to understand and modify. Parallel programming and variance reduction techniques can be used to improve the speed and efficiency of the simulation. The pen-Vox extension presented by (Badal-Soler, 2008) was used to introduce three-dimensional voxel geometry for PENELOPE simulations, in addition to the quadric surface geometry that is inherent to the package.

XRaySim (Viswanathan and Balasubramaniam, 2009) is an open-source simulation package for industrial non-destructive testing and medical imaging applications. It uses C++ and open-source libraries to simulate X-rays. The input energy spectra are simulated using standard MC methods, while phantoms and their material properties are used to acquire simulated X-ray images on specified detectors. Phantom geometry can be modified using commercial CAD packages, custom materials can be defined and defects in test objects can be simulated. Detector characteristics can be defined and various scan geometries can be simulated. XRaySim does not support slot-scanning X-ray imaging and is not able to do high resolution simulations (e.g. 50microns/pixel).

Freud et al. (2000) explain a simulation setup similar to XRaySim based on triangular mesh geometry, radiation transfer and ray-tracing. Ray-tracing is used with the X-ray attenuation law to simulate 3D phantoms for non-destructive testing (NDT). The X-ray imaging process specification comprises defining X-ray source, beam, test object and detector. The work has potential applications beyond NDT, but development is in the early stages and the code is not publicly available. The simulation does not currently have the flexibility for extension to slot-scanning X-ray imaging systems.

2.3 Simulation of slot-scanning X-ray systems

Scheelke (2005) presented a system model for the slot-scanning imaging system of the Lodox Statscan machine. A linear cascaded model of the detector was developed and validated using MTF, NPS and DQE measurements. The effect of the parameters of the detector on the resulting DQE were studied. The system performances evaluated using the DQE for detectors at different thicknesses, modelled at different CCD noise levels and binned using various binning factors were studied. An expression for “system DQE”, a measure proposed by other authors to compare different imaging systems, was presented based on the cascaded model and the DQE. The scatter to primary ratio, a component of the system DQE calculation, was based on the scattered radiation modelled as additive system noise. It was observed that a higher system DQE can be achieved by using slot-scanning, suggesting that slot-scanning results in better image quality compared to conventional X-ray imaging systems. The modelling was not based on Monte Carlo methods and was focused on the effects of the detector parameters on the DQE.

Irving (2008) studied the dose measurements made using a linear slot-scanning radiography system and developed a dose estimation model. The measurements and calculations used for the entrance and effective doses in conventional X-ray systems were verified and extended to slot-scanning systems. An ionisation chamber and dosimeter were used to measure the entrance dose and a Monte Carlo simulator was used to estimate the effective dose based on the entrance dose. The effective dose for the slot-scanning system was estimated based on the energy spectrum generated by the source and the simulation of a filter through which the beam was attenuated. The dose was calculated using organ energy absorption data based on a standard sized patient. The simulations were limited to the estimation of the effective dose and the imaging system was not simulated. The model used for the estimation of dose was accurate for linear slot-scanning radiography techniques and was found to be faster than Monte Carlo simulations. It was also concluded that the reasons for the low dose in slot-scanning imaging systems compared to conventional radiography systems was the reduction of scattered radiation due to the beam geometry.

2.4 Image quality metrics

Imaging simulation tools can be validated by comparing their output images with real images. While human visual inspection is useful to judge the quality of an image from a clinical perspective, it remains subjective, and various metrics have been used to determine X-ray image quality in an objective way. The image quality measures are divided here into two categories, region-based and system-based.

2.4.1 Region-based metrics

Region-based metrics are calculated using region(s) or group(s) of pixels in the X-ray image. Image contrast and contrast-to-noise ratio (CNR) are examples of region-based metrics. The work done in (Hussein, 2008) uses Equations 2.1 and 2.2 below to calculate image contrast and CNR.

In Hussein (2008), the contrast and CNR are calculated using four different and mutually-exclusive regions in the X-ray image. This generates four different values for the same metric and using more regions can result in a wide range of values for the same metric. Although region-based metrics can be useful in evaluating image quality in a specific region, they are not robust enough to quantify the entire system.

2.4.2 System-based metrics

System-based metrics are more robust and objective in quantifying the entire imaging system. While human inspection remains a good subjective measure to decide the quality of an image from a medical perspective, the detective quantum efficiency (DQE) is the most objective way to compare two X-rays from different imaging systems (Martin et al., 1999, Stierstorfer and Spahn, 1999).

The edge spread function (ESF) is the step response of the imaging system because it plots the output of the system when the input is a step. The line spread function (LSF), the derivative of the ESF, is the impulse response of the system. The modulation transfer function (MTF) is the Fourier transform of the LSF, or alternatively the

frequency response of the system. The DQE can be viewed as a signal-to-noise ratio of the modulation transfer function (MTF) and the noise power spectrum (NPS).

2.4.3 Image contrast and CNR

Image quality measures like image contrast, contrast-to-noise ratio and photon noise were discussed in the context of comparing X-ray images to simulations in Hussein et al. (2009). The contrast-to-noise ratio was defined as the ratio of object contrast against a uniform background to the standard deviation of image noise by (Rose, 1973). According to Rose (1973), if $S_{\text{background}}$ and S_{roi} are mean intensities of the background and regions of interest (ROI), image contrast is defined as

$$C_{img} = \frac{S_{\text{background}} - S_{\text{roi}}}{S_{\text{background}}} \quad (2.1)$$

and the contrast-to-noise ratio is

$$\text{CNR}_{img} = \frac{S_{\text{roi}} - S_{\text{background}}}{\text{noise}}. \quad (2.2)$$

The noise was defined as a result of quantum noise, dark noise, electronic and digitisation noise. The standard deviation of pixel values from the mean of a uniform area in the background was measured as noise. A statistically uncorrelated distribution of image photons is assumed in the model described by Rose (1973), but in reality the contribution of scattered X-ray and secondary photons may introduce statistical correlation. A more general definition of signal-to-noise ratio, which accounts for signal and noise propagation in a linear system and the frequency dependent task of the detected signal can be defined using the Modulation Transfer Function and the Noise Power Spectrum.

2.4.4 Modulation Transfer Function, Noise Power Spectra and Detective Quantum Efficiency

A more detailed and objective assessment of X-ray images is discussed in ICRU (1996), using three broad types of parameters. The objective assessment can be used to compare images from different imaging systems, geometries and machines. The three parameters are a macro (over a large area) system transfer function, measures of spatial resolution

and a measure of noise. The macro system transfer function is a relationship between the input X-ray quanta and the output optical density. Measures of spatial resolution are the response of the system to small features, for example the blurring and displacement of the input signal. Generally the imaging system is considered a linear and time invariant system and the measures of spatial frequency are the edge spread and the line spread functions. The modulation transfer function (MTF) is described as the frequency response of the line spread function. The final measure to analyse the image quality is the noise measure. Noise can have a number of sources and can be complicated to measure (de Villiers and de Jager, 2003). Noise is therefore measured in terms of the spatial frequency content, known as the noise power spectrum (NPS). The detective quantum efficiency (DQE) is the combination of all three measures.

The resolution properties of an image are defined by the MTF. The MTF is dependent on the edge spread function (ESF) and the line spread function (LSF) which are based on the sharpness of an edge in the image. Specifically, the MTF of a radiographic system can be determined by evaluating the response of the system to periodic patterns or by calculating the line spread function using a narrow slit formation (Martin et al., 1999, Samei et al., 1998). The same method has been used previously to calculate the MTF on the Lodox StatScan slot-scanning X-ray imaging system by (de Villiers and de Jager, 2003).

The DQE is defined as (Stierstorfer and Spahn, 1999) as

$$DQE(\nu) = \frac{(S/N)_{out}^2(\nu)}{(S/N)_{in}^2(\nu)}, \quad (2.3)$$

where S is the signal amplitude, N is the noise power spectrum and ν is the spatial frequency. The spatial frequency ν is a vector in the case of X-ray images. There is some ambiguity with respect to the definition of the input signal and noise in the literature (Stierstorfer and Spahn, 1999). Most papers consider detectors as energy integrating devices so the energy is the relevant quantity.

The work done in de Villiers and de Jager (2003) extends the definition of MTF and DQE for slot scanning imaging systems in particular. The basic formulation of the DQE based on (de Villiers and de Jager, 2003, International Electrotechnical Commission,

2003, Stierstorfer and Spahn, 1999) is

$$DQE(\nu_x, \nu_y) = G^2 MTF^2 \frac{W_{in}^2(\nu_x, \nu_y)}{W_{out}^2(\nu_x, \nu_y)}, \quad (2.4)$$

where

- (ν_x, ν_y) = spatial frequency coordinates
- $W_{in}^2(\nu_x, \nu_y)$ = input noise power spectrum
- $W_{out}^2(\nu_x, \nu_y)$ = output noise power spectrum
- G = incremental gain used in converting pixel raw data to photon count
- MTF = modulation transfer function.

2.5 Mammography and Digital Breast Tomosynthesis

Full-field digital mammography (FFDM) is useful in the detection, diagnosis and management of breast cancer. FFDM is considered as an improvement of conventional screen-film mammography producing true positive rates of 75% and true negative rates of 90%. FFDM overcomes the widely acknowledged drawbacks of screen-film mammography of limited dynamic range, poor contrast and susceptibility to poor film generation conditions. FFDM is especially useful to image subtle lesions in denser breasts better than screen-film mammography (Karellas and Vedantham, 2008).

Three-dimensional anatomical data is projected on to two dimensions using the formation of a two-dimensional FFDM image. One of the limitations of FFDM is that the FFDM image may show overlapping breast tissue, and small tumours can be obscured due to overlapping tissue. This can result in a high number of patient recalls, more screenings and possible biopsies. Approximately 20% tumours are missed by mammography and about half of the women screened annually will experience a false-positive result with the call-backs and biopsies. This creates anxiety in the patient and increases the cost of healthcare (National Cancer Institute, 2014). Digital Breast Tomosynthesis (DBT) provides a 3D alternative to FFDM which has been shown in several studies to improve detection rates compared to FFDM and to be superior in detecting multiple

breast tumours and microcalcifications (Helvie, 2010).

Multiple images, also known as projections, of the compressed breast are acquired at different angles in DBT. These projections are reconstructed using backprojection algorithm to display planar slices through the breast. The acquisition of DBT data is based on three parameters namely number of projections, total angular range and angular intervals. The optimisation of these parameters to improve image quality of the 3D reconstructions while keeping radiation dose to a minimum, is an area of active research interest (Choi et al., 2012). Image quality improves with increasing number of projections but the radiation dose also increases. This trade-off between image quality and radiation dose is present in any X-ray imaging. Optimising the DBT parameters, in conjunction with the FFDM parameters, is essential in the design of new and better breast imaging systems.

The commercially available DBT machines use various methods to acquire the DBT data (Helvie, 2010). The DBT machines vary the arc of the machine movement, the number of projections, angular range and angular intervals while acquiring the data. In addition to these DBT parameters, the mammography parameters like breast thickness, system geometry, system resolution, binning of image data and filtered/unfiltered X-ray source can also be varied. Any combination of these DBT and mammography variables will result in image variations, making clinical comparisons difficult.

Choi et al. (2012) developed a prototype DBT system to study the effect of the tomosynthesis parameters on the projections and the resulting reconstruction. The CIRS (Computerised Imaging Reference Systems, Norfolk, VA, USA) breast phantom was used as a test object, and reconstructions resulting from 32 different combinations of parameters, with six angular ranges and eight projections, were studied and compared using contrast-to-noise ratio and artifact spread function. The study concluded that a wide angular range improves image quality, especially in the vertical direction, but a large number of projections increases the electronic noise and decreases the contrast-to-noise ratio. A wider angular range can also increase scan time, leading to more patient motion which degrades the image quality. This prototype system only tested the effects of tomosynthesis parameters and did not vary parameters related to mammography like the X-ray source, binning, system geometry and system resolution.

Very few simulation systems are available for the simulation of slot-scanning imaging systems and to the author's knowledge there are no simulation systems for slot-scanning DBT. Helvie (2010) recognises DBT as a new modality and concludes that favourable initial trial results need to be confirmed with more representative trials and the effect of DBT parameters on the detection of microcalcifications needs to be explored further. A flexible simulation system that models the physics of X-ray photon transport accurately and includes the geometric requirements of DBT is lacking.

Several 2D and 3D mathematical simulations of breast tissues and microcalcifications have been developed. Bakic et al. (2002) developed a three dimensional breast phantom based on a realistic distribution of tissue structures. A compression model was used to change the size and placement of structures in the phantom. A mammogram acquisition model was used to simulate synthetic mammograms using a monoenergetic parallel beam source applied to the compressed breast phantom. Mammograms simulated using this system were printed on film and shown to radiologists. Although the simulated images were not validated with real X-ray images it was concluded that the proposed model could be used to study the correlation between 3D breast composition and 2D mammogram images.

Hussein et al. (2009) defined a tissue-equivalent mathematical breast phantom, based on the commercially available CIRS phantom, and simulated the phantom using a prototype of a linear slot-scanning mammography system. Pixel intensities in different areas of the phantom were estimated using empirical equations for variables in the X-ray imaging chain. The simulated and real images of the phantom were compared using image contrast, contrast-to-noise ratio, signal-to-noise ratio and detective quantum efficiency. Monte Carlo methods were not used by (Hussein et al., 2009) and although images from a slot-scanning system were simulated, individual slots were not simulated. The effects of different methods of combining the slots to acquire the final image could therefore not be studied. Pixel intensities for the defined phantom were simulated, thus the simulation process was not independent of the phantom used. Furthermore, the phantom was two-dimensional so it was only useful for simulating mammography and did not accommodate different geometries, materials and phantom configurations, and 3D modelling.

Hunt et al. (2005) used high-resolution voxelised phantoms in modelling the breast to study and optimise the performance of digital mammography systems. The voxelised phantoms simulated adipose and fibroglandular tissue, ligaments, ducts and skin in three dimensions. The performance of digital mammography systems, specifically the radiation dose, noise in each voxel and scatter-to-primary ratios were studied. The scatter-to-primary ratios for different points in the image were estimated using a Monte Carlo based simulation process. The simulation results were compared to measurements on images of sheets of polymethyl methacrylate obtained using a GE Senographe digital mammography unit. Based on the comparisons of contrast, scatter-to-primary ratios, radiation dose and signal-to-noise ratios it was concluded that the phantoms were an improvement on the homogeneous phantom used in the past for modelling breast tissue.

Reiser et al. (2006) developed an analytic breast phantom consisting of simple shapes, aiming to capture the main features of the breast, to study DBT reconstruction. Projection data at various angles were computed analytically and the three dimensional volumes were reconstructed using filtered backprojection, expectation maximisation and total variation algorithms. The total variation algorithm is a denoising technique that removes unwanted detail from the signal while preserving important details such as edges. The reconstruction results showed that the total variation denoising techniques used with filtered backprojection achieved highest contrast for mass lesions and best in-depth resolution.

Sechopoulos and Ghetti (2009) evaluated different combinations of angular range and number of projections using DBT computer simulations in order to characterise their effects on the reconstructed image. The study was restricted to the effects of these two parameters and the reconstructed images were compared using contrast and artifact spread function. Although the angular intervals were not part of the study, it was concluded that increasing the angular range always increases the vertical resolution of the reconstruction. Vertical resolution decreased when the number of projections in the reconstruction set went over a certain threshold, which depended on the angular range. It was noted that the angular range was more important than other DBT variables to attain good reconstructed images.

Baptista et al. (2014) used the MC N-Particle eXtended (MCNPX) code (Pelowitz,

2011) to generate DBT projection data of a homogeneous breast phantom. Dose and image quality measures were used to evaluate DBT reconstruction using different combinations of parameters and at different X-ray source energies to optimise image quality and dose.

Skaane et al. (2014) compared cancer detection using FFDM versus using FFDM and DBT according to changing breast densities. It was observed that the use of FFDM and DBT together increased the rate of cancer detection in women with breast densities BI-RADS 2 to 4 but observed no difference in women with breast density 1. It was concluded that FFDM and DBT used together can significantly improve cancer detection rates in denser breasts.

The clinical trials analysed by Helvie (2010) also suggested that there was an increase in the cancer detection rates with the use of DBT, which considerably decreased the false-positive rate and reduced the number of patient call-backs. There was also a significant decrease in biopsy rates and DBT yielded better image quality. Helvie concluded by pointing out that although initial studies have favoured the use of DBT, further studies and investigations need to be carried out. It also suggested that more clinical trials and experiments were necessary before conclusively stating that DBT is better for detecting microcalcifications.

The concept of virtual trials and virtual performance assessments was proposed by Elangovan et al. (2014) as an alternative to large and representative clinical trials of FFDM and DBT. Two virtual approaches, based on simulation chains of modelling tools, were presented to save the investment of time and resources in clinical trials. The two simulation chains were called total image simulation, which represented the image acquisition process, and inserted lesion simulation, which simulated radiologists' assessment by including lesions and microcalcifications into the simulated images. The simulation chains, validated using real images, modelled mammographic and tomosynthesis images of comparable quality to real images. Contrast-to-noise and image sharpness measures were used for the comparison of real and simulated data.

2.6 Summary

X-ray image simulation using Monte Carlo methods has been a subject of considerable research with several implementations and their advantages and drawbacks. Some implementations, like Viswanathan and Balasubramaniam (2009), Hirayama et al. (2005) and Halbleib et al. (1992), are not flexible enough to accommodate slot-scanning while others like, Agostinelli et al. (2003, 2006), are difficult to use. Other simulation methods are focused on simulating a part of the imaging chain, for example the X-ray input energy spectrum is simulated in SpekCalc (Poludniowski et al., 2009). Scheelke (2005) studied the scattered radiation in slot-scanning systems using Monte Carlo simulation methods, without simulating the X-ray image generation process. Irving (2008) used Monte Carlo simulations to estimate the entrance and effective dose of a slot-scanning system. A flexible, easy-to-use, three-dimensional and general purpose simulation system for slot-scanning imaging is lacking. A flexible system which can be modified for various geometries and phantoms is necessary for slot-scanning X-ray image simulation.

Digital breast tomosynthesis is a new modality that needs further investigation. A tool that can simulate the effect of DBT parameters on the final reconstructions is desirable. For slot-scanning tomosynthesis, a simulation system that can be used to model the angular projections is needed.

Chapter 3

Simulation tools: PENELOPE and penEasy

PENELOPE is a set of Fortran subroutines used for X-ray transport problems. The development of the code system started in 1996 and it has continuously evolved since then because of the work done by the Nuclear Energy Agency. The PENELOPE package, including its subroutines and modifications, forms the basis of the simulation techniques discussed in this thesis. The PENELOPE package, with the workings of its subroutines, is described in this chapter. The components of PENELOPE like the geometry, material properties, X-ray source and detector models are discussed in Sections 3.2 to 3.5. The subroutines to estimate the dose and to generate the X-ray image are presented in Sections 3.6 to 3.8.

3.1 Introduction

PENELOPE is a general-purpose Monte Carlo simulation package that describes the transport of electrons, positrons and photons in any material for the energy range from 50eV to 1GeV. PENELOPE, which stands for PENetration and Energy LOss of Positrons and Electrons, is an open software package. It is actively developed and maintained by the *Universitat de Barcelona* and the Nuclear Energy Agency.

The PENELOPE package was chosen due to its accurate physics models (Badal-Soler,

2008, Salvat et al., 2006), especially for low energy radiation transport and because it is widely used to model radiation transport problems. The low energy radiation transport modelling allows PENELOPE to simulate any photon beam radiation field currently used in medical imaging. Another advantage of PENELOPE is the flexibility of the physics and geometric operations in the simulation algorithm. The geometric operations are separate from the physics of radiation, so new and complex geometric models can be implemented without compromising the accuracy of the physics aspect using Rational Inverse Transform with Aliasing (RITA) subroutines. In PENELOPE, RITA subroutines are used to model the elastic and inelastic photon collisions.

PENELOPE has been extensively benchmarked with experiments and with other Monte Carlo codes in the past. For low-energy photon transport, PENELOPE was benchmarked with dose comparisons to MCNP4 and EGS4 (presented in Nelson et al. (1985)) by Ye et al. (2004). A comparative study between PENELOPE, GEANT3, GEANT4, EGSnrc and MCNPX for simulation of electron transport through thin slabs was performed by Vilches et al. (2007). Panettieri simulated MOSFET detectors for high energy photon beams using PENELOPE in (Panettieri et al., 2007). A realistic anatomical phantom described using triangular meshes in penMesh (Badal et al., 2009) was simulated using PENELOPE and an application to prostrate brachytherapy imaging was discussed. An efficient depth and energy dependent Monte Carlo model for a CsI detector using PENELOPE and PENGEOM was defined by Kyprianou et al. (2008).

PenEasy is a modular main program for PENELOPE that includes various sources (see Section 3.4) and tallies (see Section 3.7). PenEasy provides a tool to simulate a wide spectrum of problems, and its modular nature enables adaptation to different scenarios. PenVox (Badal-Soler, 2008), the geometric subroutines linked to penEasy, extend the standard PENELOPE geometry, based on quadric surfaces, to voxelised geometry. PenVox is useful in simulating phantoms with free-form (or arbitrary) shapes and is used to simulate anatomical phantoms of patients. PenMesh (Badal et al., 2009) uses closed triangular meshes to define test objects and phantoms, and is used to define anatomical phantoms that require a high amount of detail.

PenEasy_Imaging is an extension to PENELOPE that provides capabilities for the simulation of X-ray imaging systems (Badal-Soler, 2008). The two main additions in penEasy_Imaging are the image tally and the rectangular beam source. The image tally module is used to generate radiographic images as an output of the penEasy X-ray transport simulation. The images can be generated in many ways, described in Section 3.7. The rectangular beam source, or fan-beam source, is a X-ray source model (see Section 3.4) that produces a rectangular field of radiation on the detector plane. The MC-GPU package is a GPU-accelerated X-ray transport simulation package, implementing a massively multi-threaded Monte Carlo simulation algorithm for X-ray radiation transport based on PENELOPE. This package can be used to simulate realistic radiographic projections and computed tomography (CT) scans of the human anatomy.

3.2 Geometry

The PENGEOM package contains the geometry subroutines used in PENELOPE. PENGEOM implements a simple constructive geometry model which defines objects by the volume enclosed between quadric surfaces. The PENGEOM package is a standard part of the PENELOPE code distribution, and the geometry is written in a text file which contains the different modules involved in a given geometry. The geometry information is divided into different modules and bodies that can be defined using quadric surfaces. Figure 3.1 shows the quadric surfaces used in PENGEOM. The reduced form (eg. 1,1,1,0,-1 for a sphere) is used to define particular surfaces in the geometry file.

The quadric geometry model defined by PENGEOM is robust in its surface definitions but is limited in the shapes it can represent. Free-form surfaces can not be accurately defined. Improvements like penVox and penMesh (Badal et al., 2009) enable the user to simulate voxelised geometries and triangular mesh geometries respectively, which include free-form surfaces. PenMesh (Badal et al., 2009) combines the simplicity of the objects defined using quadric surfaces and the geometric detail of objects represented using triangle meshes. Complex anatomically realistic phantoms can be simulated using penVox and penMesh (Badal et al., 2009) geometries.

The PENELOPE package includes two tools to visualise the geometry in two dimensions

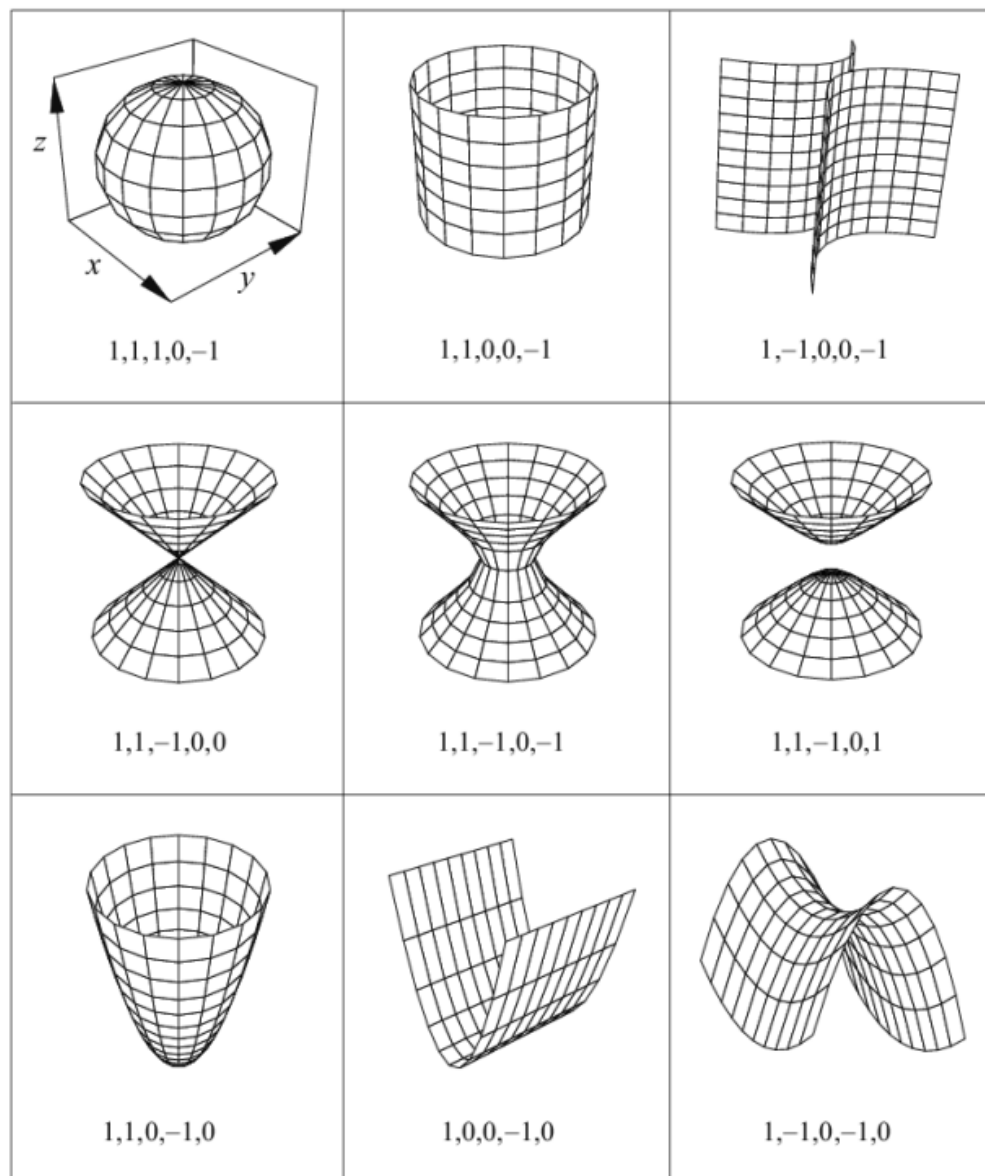


FIGURE 3.1: Graphical representation of the quadric surfaces used in PENGINEOM in reduced form (image taken from the PENELOPE manual (Salvat et al., 2006)).

using *gview2d* and three dimensions using *gview3d*. These programs are only applicable to the basic quadric geometry that PENGINEOM defines and other CAD packages can be utilised to view voxel and triangular mesh geometries.

3.3 Material properties

The PENELOPE package has predefined material properties for 280 materials (Salvat et al., 2006) ranging from basic elements like hydrogen and carbon to complex substances like bones, muscles and tissues. The material properties of these substances include mass densities, attenuation coefficients and atomic numbers. Complex substances contain the material properties of their constituting components in the given ratios.

Materials that are not predefined can be defined using their components and their material properties, and files can be generate accordingly. The components can be mixed together based on their molar mass, atomic weights and molecular structure.

Each material is assigned a number and a material file that can be combined with other materials to prepare a material file for any particular simulation. Materials can be visualised using the PENGEOM package.

3.4 Source Models

Two configurable X-ray source models are included in penEasy. Their configuration variables can be set by the user and only one source can be active in any given simulation. The flexibility granted by the configuration variables make the source models useful for simulating different X-ray imaging geometries.

The Box Isotropic Gaussian Spectrum (BIGS) source can be used to define volumetric sources limited by quadric surfaces given in the PENGEOM geometry. The particle type emitting from the source can be chosen and the input spectrum is defined using a Gaussian function. The Phase-Space File source reads the initial state of the particles to simulate from an external file. The Phase-Space File source is generally used to model very specific radiation fields and plays an important part in computing the statistical uncertainty.

A rectangular beam source is introduced in the penEasy Imaging extension to PENELOPE and is not a part of the standard PENELOPE package. This source emits a

collimated beam of radiation that produces a rectangular field of radiation on the detector. The emitted beam is equivalent to a cone beam from a collimated point focal spot. The user can define the source angles to control the width of the collimation and the dimensions of the radiation field. The energy spectrum emitted by the source and the source-to-detector distance can be defined by the user.

3.5 Detector Models

The X-ray image is formed by scoring the energy deposited inside the detecting object, which is typically a thin layer of scintillating material. The detector geometry can be defined as a thin plane in the quadric geometry setup of PENGEOM. Triangular meshes or voxelised geometries can also be used to define the detector. The location, orientation (direction and tilt angles), size and the number of pixels can be defined using the input file. The detector material is typically CsI, but can be changed depending on the detector being modelled. The configuration variables of the detector, such as number of pixels and location in the geometry, are useful to model different resolutions and geometries.

3.6 Scattered Radiation

The dominant particle interactions for the energy range from 50eV to 1GeV are the photoelectric effect, electron-positron pair production, coherent (Rayleigh) scattering and incoherent (Compton) scattering. These scattering factors are modelled by PENELOPE using photon collision models in each photon shower history. Other interactions like photo-nuclear absorption are disregarded as the probability of their occurrence is low. The four causes of scattered radiation (Salvat et al., 2006), shown in Figure 3.2, are explained as follows:

- In the photoelectric effect, a photon of energy E is absorbed by the target atom pushing it to an excited state.
- Coherent or Rayleigh scattering is a process by which photons scatter in such a way that the energies of the incident and scattered photons are the same.

- Incoherent or Compton scattering happens when a photon of energy E is absorbed by an electron and a secondary photon of a different energy E' is released in a different direction to that of the incident photon.
- Electron-positron pairs are produced when a massive charged particle, like an electron, absorbs the photon energy and momentum so that the two quantities are conserved. The electron-positron production can give rise to photons if the target electrons are at rest.

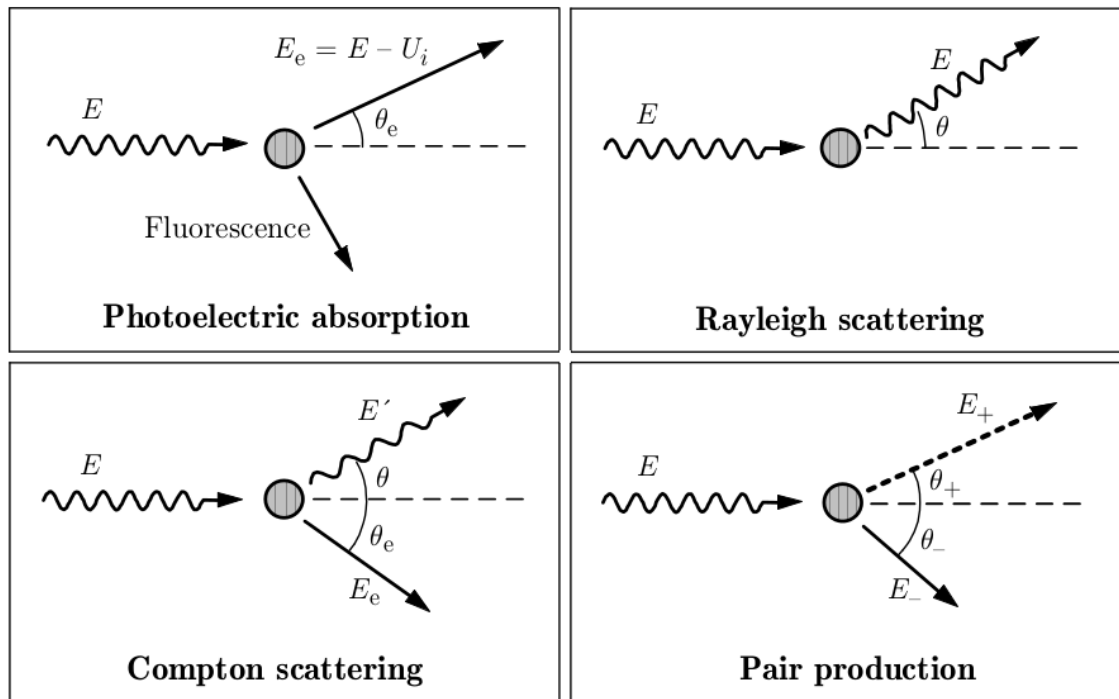


FIGURE 3.2: Basic interactions of photons with matter causing scattered radiation ((Salvat et al., 2006)).

3.7 Tallies

PenEasy includes subroutines called tallies to calculate common quantities of interest in the simulation. A selection of useful tallies, in the context of this thesis, are as follows:

Dose distribution There are three different types of tallies that can be used to calculate dose distribution in the imaging geometry. The 3D spatial distributions of absorbed dose in homogeneous regions can be calculated using cubic, cylindrical

or spherical bins. The 3D dose distribution data for cubic bins can be integrated over the x , y or z directions to obtain the 1D and 2D dose distributions. The cylindrical and spherical bins are more constrained in terms of geometry, but the cubic bins can be used for most applications.

Voxelised dose distribution The dose distribution can be calculated in terms of voxels where the defined geometry is voxelised.

Pulse height spectra The distribution of energy deposition in a certain detection material can be calculated using this tally.

Particle trajectories The 3D tracks of particles can be calculated and recorded. This is particularly useful to study effects of collimation or other changes in the X-ray beam.

Image tally The image tally is used to generate radiographic images as the output of the penEasy X-ray transport simulation. The detector object and its properties, like pixel resolution and detector material, can be defined as a plane in the simulation geometry using subroutines mentioned in Section 3.2.

The output X-ray image can be produced by scoring the 2D energy deposition inside the detector object. The pixel values in the image have the units of eV/cm^2 and the image is equivalent to the energy fluence in each pixel if the detector is set to have completely absorbent material. The user can choose to generate an output image that has only primary particles (no scattered particles), scattered particles, or primary and scattered particles. The scattered particles can be further separated into Rayleigh, Compton and multiple scattering events.

Another useful option for generating the output image is the analytical ray-tracing model. A ray-tracing process is used to simulate a noise and scatter free image, with the Monte Carlo simulation. In this model a reduced number of rays are cast on each pixel of the detector to estimate the X-rays reaching the pixel without interacting in the track. This model can be used for checking the test object and geometry and is usually faster than the Monte Carlo simulation option.

The image tally is defined in the penEasy_Imaging extension to PENELOPE and is not part of the standard PENELOPE package.

3.8 Summary

The PENELOPE package, its subroutines and extensions are described. A brief overview of the benchmark testing and applications of PENELOPE is given. This chapter also provides an overview of the PENELOPE structure, including system geometry, source and detector models, materials and information on image formation. These subroutines and extensions form a part of the simulation process presented in this thesis.

Chapter 4

System requirements for Linear Slot-Scanning X-ray imaging

The system requirements for linear slot-scanning X-ray imaging are described in this chapter. The system design and components of a general purpose linear slot-scanning X-ray imaging system are described. This general purpose system can be modified to cover a wide range of X-ray imaging systems. For example, it is used in Chapters 5 and 7 to simulate a full-body X-ray imaging system and a digital mammography system respectively. The parameters and imaging geometries involved in slot-scanning X-ray imaging systems are defined in this chapter.

A slot-scanning X-ray imaging system is designed to provide a linear scanning geometry with a narrow fan beam to offer good scatter rejection. The narrow fan beam scans the patient by horizontal movement in the scan direction, as shown in Figure 4.1. The differences in geometry between a full-field digital X-ray imaging system and a slot-scanning system are shown in Figure 4.1. The linear slot-scanning radiographic geometry uses a narrow fan beam that moves linearly in synchrony with a narrow detector to provide good signal-to-noise ratio by reducing scatter radiation. The result is high resolution image with good contrast while keeping the patient dose to a minimum (Beningfield et al., 2003, Jing et al., 1998, Samei et al., 2005).

Section 4.1 defines the different components in the imaging system and Section 4.2 describes the simulation of the system using PENELOPE and penEasy_Imaging. The

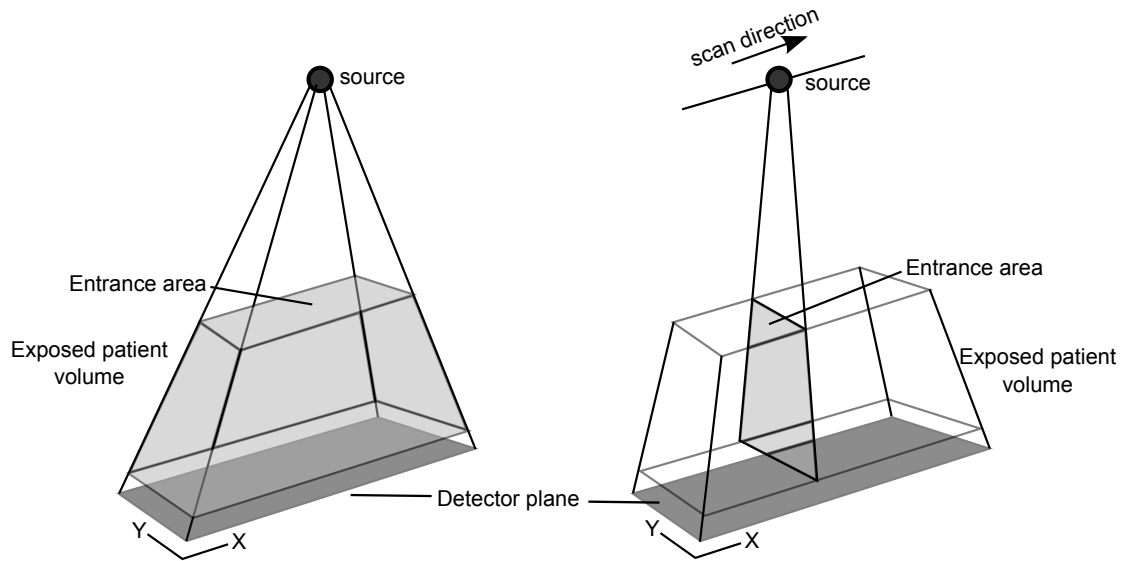


FIGURE 4.1: The differences in the geometries of a full-field digital radiographic system on the left and a slot-scanning system on the right. The effects of collimation and the narrow fan beam on the detector and the exposed patient volume are shown, adapted from (Irving et al., 2008).

calculations for the MTF, NPS and DQE measures used in this thesis are explained. A sample simulation is presented in Section 4.3 to demonstrate the modifications of the code and their impact on the resulting X-ray image.

4.1 System design and requirements

4.1.1 Mechanical design

The mechanical design used in this project is based on the LODOX design used in Irving (2008) and Scheelke (2005). A typical linear slot-scanning X-ray imaging system consists of a X-ray source, a collimator (and also a post-collimator in some cases), X-ray filters and the detector, as shown in Figure 4.2. The X-ray source generates the X-ray energy spectra, while the collimator and filters produce the X-ray beam which passes through the object to reach the detector. The X-ray filters attenuate the low energy X-ray photons that reduce image quality and increase patient dose. The collimator gap defines the beam-width B_w in Figure 4.2.

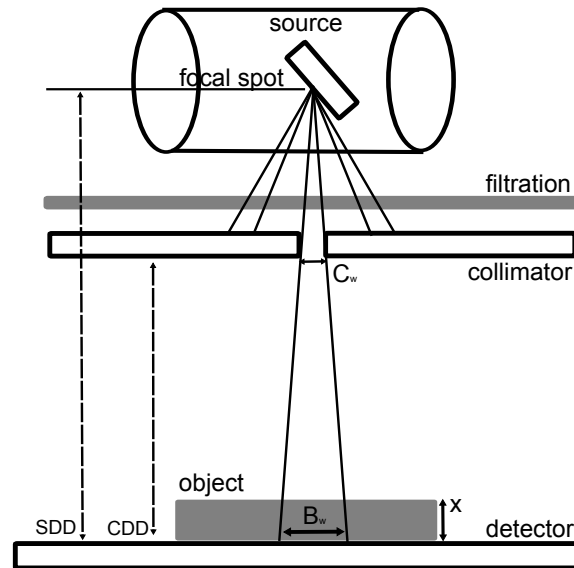


FIGURE 4.2: A typical slot-scanning X-ray system. SDD is the source-to-detector distance, CDD is the collimator to detector distance and x is the thickness of the object to be scanned. The width of the collimator is C_w and the beam-width at the detector is B_w . The slot direction is coming out of the page and the scan direction is from left to right on the page.

4.1.2 X-ray tube

X-ray sources are vacuum tubes that produce X-ray energy which is a part of the electromagnetic spectrum. The X-ray tube is defined by its voltage and current ratings. For example a 45kV-100mA tube is common in digital mammography systems. X-ray tubes are also characterised by the material properties of their anodes and cathodes and the size of their focal spots. Very small focal spots generate very high-resolution images. The selection of the focal spot in the X-ray tube is a tradeoff between the maximum power limit and the spatial resolution: increasing the focal spot size decreases the spatial resolution but increases the power limit. The power limit of the tube is the point at which the tube starts overheating.

4.1.3 Detector specifications

The detector comprises a scintillator which converts X-ray photons to scintillation light photons, a fiber optic plate or taper and the CCD which converts light photons into an electrical signal. The choice of scintillator material and dimensions depends on the imaging application. The scintillator is coupled to the CCD using a fiber-optic face

plate. These different components of the detector and the electronic circuits connected to them add to the noise of the system.

4.1.4 Time delay integration mode

In slot-scanning X-ray imaging systems, the source and the detector are mounted in the same C-arm and move across the patient to acquire the X-ray image. The time delay integration (TDI) read-out technique, also known as drift scanning, is a rapid read-out technique for reading data out of the detector CCDs. As the source moves across the patient in a continuous motion, the data captured at each position is written out so that the data from the next position can be captured.

While modelling the TDI mode of the detector, the simulation process divides the detector into parts or slots representing the collimated beam. The continuous motion of the source across the patient is modelled in a discrete manner. The source and detector move in the simulation geometry and during the simulation, the data captured is stored in the computer's memory. The physical movement of the source is modelled using distance between two slots on the detector. The slots generally overlap each other to ensure that a certain area on the detector occurs in many slots. The combining of the slots averages the output at the detector, reducing the noise while keeping the input signal energy low. All the individual scans are integrated to produce the final X-ray image. Figure 4.3 shows two consecutive slots in the detector. The number of slots depends on the size of each slot, also the beam width, and the step size between two slots.

The step is the distance between the beginning of consecutive slots. The step width can be varied in simulation. A larger step size can be used to reduce the run time of the simulation.

4.2 Modelling the imaging system and its performance

The simulation process consists of three major components: PENGEOM, which includes the geometric and material properties of the system, PENELOPE, which keeps a record of the flight paths of the photons through matter and penEasy_Imaging which generates

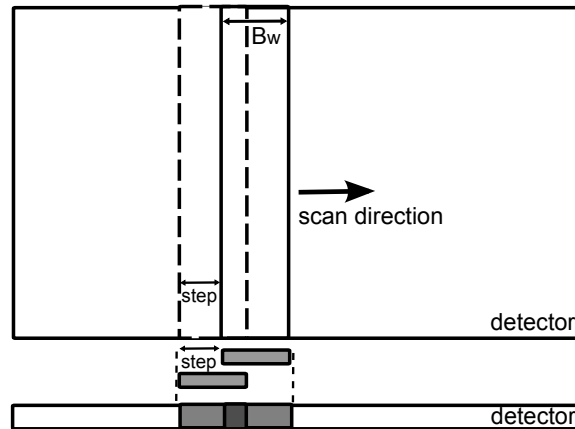


FIGURE 4.3: TDI detector operation, with two consecutive slots shown in top view and front view. The beam-width, B_w , is also the width of the slot. The step is the space between the beginning of two slots. The detector output is an integration of the slots. The beam width and the step are shown in the top and front view.

the final X-ray image based on the detector models and simulation parameters. Figure 4.4 shows a block diagram of the simulation process.

The inputs are the X-ray source, detector and object to be imaged. The properties of the X-ray source, like the number of photons, energy spectra, local and focal spot, can be defined. The collimator and the components forming the final X-ray beam also form part of the source. The material of the collimator, collimator gap width and the dimensions of the collimator can be set. Three different detector models can be defined namely the primary model, the scatter model and the ray-tracing model. The primary model contains the geometric information including scatter and collects photons to generate the final image. The scatter model separates the primary radiation and the scattered radiation to produce X-ray images with and without scatter. The ray-tracing model is a simple model that traces the rays from the source to the detector. This model is faster to implement and run, and is a useful tool for checking the geometric setup quickly. Experiments related to the geometry of the X-ray imaging system can be conducted based on this model.

4.2.1 Geometric definitions

Figure 4.2 displays a typical slot-scanning system. The effect of collimation and the relationship between collimator width and beam width is shown. The X-ray source and the detector are mounted on the same C-arm. An image is formed as the source and

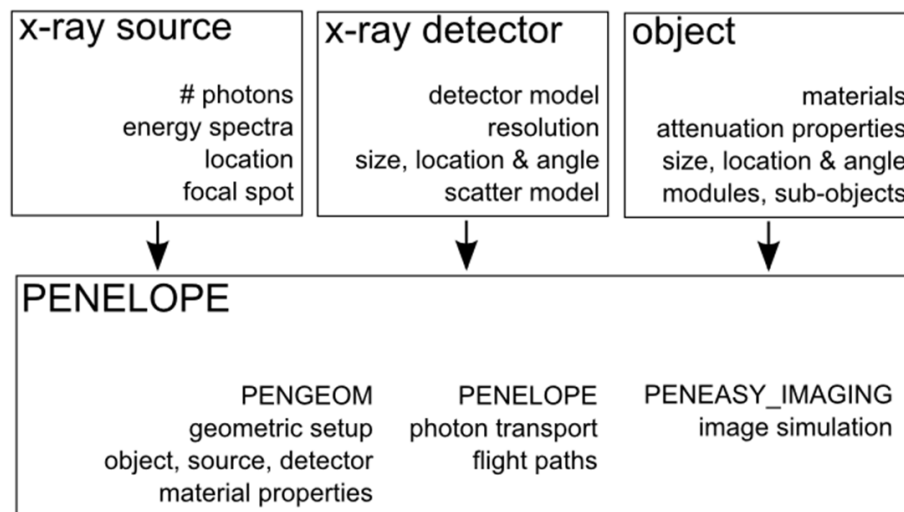


FIGURE 4.4: A block diagram of the simulation process using PENELOPE, PENGEOm and penEasy_Imaging.

detector move synchronously with respect to the patient in the scan direction, which is perpendicular to the slot direction.

The imaging geometry can be divided into two parts, namely the object geometry and the system geometry. The object geometry defines the shape and size of the object being scanned. PENGEOm splits an object into its quadric components and assigns to them material properties described in Section 3.3. The position of the object between the source and the detector also forms part of the geometry.

The system geometry contains information about the locations of the source, the detector and the object. The apertures of the source and the source-detector distance provide information about the detector size to be used. The number of pixels on the detector, and hence the resolution, can also be set. All the components in the imaging chain are located on a single coordinate system. Their relative placement, angles and distances can be simulated.

The penEasy_Imaging package provides tools to obtain the X-ray image output from PENELOPE (Badal-Soler, 2008). Thus PENELOPE handles the physics of photon travel, RITA provides scatter modeling, PENGEOm contains the geometrical information, and penEasy_Imaging converts the detector signal into output. The system

geometry shown in Figure 4.2 is defined and modified using the PENGINE package.

A rectangular beam source, described in Section 3.4, is defined using `penEasy_Imaging`. It provides a collimated beam of radiation that produces a rectangular radiation field on the detector. This source is the same as a cone beam source emitted from a point focal spot and then collimated using lead. The anode heel effect, the variation of the intensity of X-rays emitted by the anode depending on the direction of emission, is undone by using the appropriate collimation, but if necessary can be simulated by setting the apertures. Variables like the polar and azimuthal apertures, the direction of the fan-beam and the source location in the overall geometry help the user to change the source to fit the physical one. Different energy spectra may be used. Post-collimation filters are frequently used to improve scatter or reduce X-ray dose. The use of post-collimation filters can be modelled by altering the energy spectra. Adding a filter to the geometry, at the desired location and with the desired material properties, is another way of modelling filters. A filter of a specific thickness and material can be added as a plane in the geometric system to model the effect of the filter. Examples of X-ray spectra from two X-ray sources are shown in Figure 4.6, simulated using `SpekCalc` (Poludniowski et al., 2009), using a tungsten target. The smooth continuous curve in the 90kV spectrum is due to *bremstrahlung* and the spikes are the characteristic K lines for tungsten atoms. Different target materials will have different characteristic K lines resulting in varying energy spectra. K lines, or K-alpha emission lines, result when electrons transit from upper shells into K shells. These lines cause the spikes in the energy spectrum based on the materials used for the anode.

4.2.2 X-ray detector simulation

In the geometric co-ordinate system, the X-ray detector can be simulated as a plane. The position and dimensions of the detector can be set and the source-to-detector, object-to-detector and other distances can be set accordingly. The detector resolution and the material properties can also be simulated using the methods presented in Sections 4.2.1 and 3.3.

The slot width for each slot can be simulated using the fan beam source, and the movement of the source and detector in slot-scanning can be modelled in the simulation. The

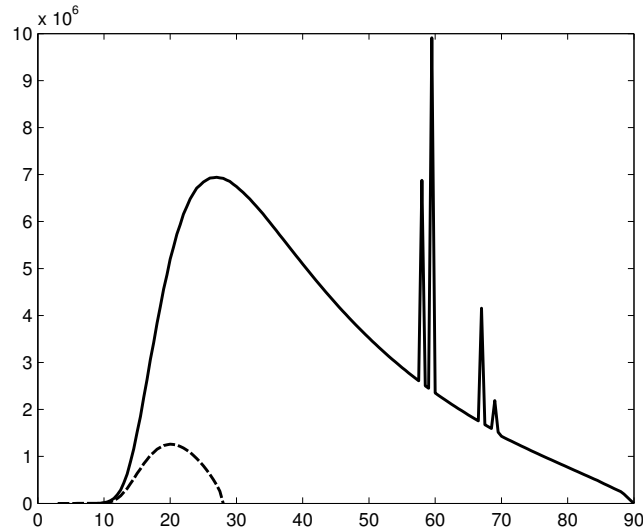


FIGURE 4.5: Examples of two X-ray spectra from a 90kV source (the continuous line) and a 28kV source (the dotted line) simulated using methods presented by (Poludniowski et al., 2009).

overlap between the slots can be modelled by shifting the source and detector and all the slots can be simulated independently. The TDI nature of the detector can be simulated by combining the simulated slots to generate the final X-ray image.

4.2.3 Imaging task

The code in PENELOPE, PENGEOM and penEasy Imaging was modified in this project for slot-scanning simulation. The source, the detector and the object are defined. The detector is divided into slots and each slot is simulated independently. For each slot, a random spray of X-ray photons is generated from the X-ray source. These X-ray photons travel through the filter, are transformed into a fan beam by the collimator and pass through the object to be collected at the detector. A random number generator is used to create the random spray of photons and then their flight path and physical interactions are tracked using the subroutines in PENELOPE. The geometry of the system is handled by the PENGEOM package and the timing modules are provided by RITA subroutines. The individual slots on the detector are combined to model the TDI detector mechanism.

4.3 A sample simulation

A sample simulation of two test objects is presented in this section. The use of slot-scanning and the necessary modifications to the code system are described to demonstrate the use of the simulation system. The X-ray energy spectrum simulation is defined in Section 4.3.1, the geometric properties of the test objects used are described in Section 4.3.2, the material properties of the geometric components are presented in Section 4.3.3 and the input file sections and definitions are shown in Section 4.3.4. The code structure used in this section is detailed in Appendix A. Sample simulations using 2 slots and 4 slots are shown.

4.3.1 X-ray energy spectrum definition

In this sample simulation, a 90kV X-ray source with a tungsten anode and 2.5mm aluminium filter is defined using SpekCalc (Poludniowski et al., 2009). The energy spectrum defined by SpekCalc is used to create the input energy spectrum file as described in Appendix A. The coefficients in the file are derived from SpekCalc and represent the graph shown in Figure 4.6.

4.3.2 Geometric definitions

Two test objects are defined, the first one is a square object and the second one is an ellipsoid. The square object has equal width and length and the height is half of the length. The ellipsoid is given unequal dimensions.

Figure 4.7 shows the geometric definitions of the six surfaces that are used to form the square object. The surfaces are given identification numbers in Figure 4.7 and these numbers are used to combine the surfaces to form modules as shown in Figure 4.8. The module is assigned material properties and the omega, theta and phi angles are used to control the orientation of the object. The x-, y- and z- shifts define the position of the object in the system geometry. A surface that is not part of any module is considered as a module in itself. A list of all the modules is given at the end of the geometry file. The number of modules and surfaces increases with the increase in the complexity of test objects.

1	180.0	38000.	39838.	62500.	24160.	87000.	2338.3
14000.	39.297	38500.	39982.	63000.	23680.	87500.	1948.5
14500.	78.535	39000.	40078.	63500.	23217.	88000.	1558.5
15000.	144.21	39500.	40157.	64000.	22756.	88500.	1167.8
15500.	247.01	40000.	40189.	64500.	22280.	89000.	778.26
16000.	399.7	40500.	40175.	65000.	21806.	89500.	388.97
16500.	608.07	41000.	40127.	65500.	21348.	90000.	-1.0
17000.	894.03	41500.	40034.	66000.	20877.		
17500.	1251.6	42000.	39927.	66500.	20408.		
18000.	1702.1	42500.	39809.	67000.	47247.		
18500.	2248.8	43000.	39629.	67500.	19475.		
19000.	2886.7	43500.	39467.	68000.	19011.		
19500.	3630.9	44000.	39237.	68500.	18548.		
20000.	4467.2	44500.	39016.	69000.	25343.		
20500.	5380.1	45000.	38748.	69500.	17161.		
21000.	6427.3	45500.	38492.	70000.	14457.		
21500.	7514.1	46000.	38199.	70500.	14167.		
22000.	8713.3	46500.	37872.	71000.	13862.		
22500.	9951.8	47000.	37576.	71500.	13561.		
23000.	11276.	47500.	37237.	72000.	13254.		
23500.	12588.	48000.	36875.	72500.	12934.		
24000.	14031.	48500.	36536.	73000.	12618.		
24500.	15407.	49000.	36165.	73500.	12289.		
25000.	16779.	49500.	35764.	74000.	11964.		
25500.	18247.	50000.	35386.	74500.	11626.		
26000.	19681.	50500.	34981.	75000.	11293.		
26500.	21055.	51000.	34575.	75500.	10947.		
27000.	22487.	51500.	34165.	76000.	10598.		
27500.	23829.	52000.	33732.	76500.	10253.		
28000.	25217.	52500.	33321.	77000.	9897.4		
28500.	26472.	53000.	32885.	77500.	9538.6		
29000.	27755.	53500.	32449.	78000.	9183.2		
29500.	28870.	54000.	32012.	78500.	8818.5		
30000.	29995.	54500.	31554.	79000.	8451.2		
30500.	31128.	55000.	31117.	79500.	8081.5		
31000.	32054.	55500.	30658.	80000.	7709.5		
31500.	33063.	56000.	30200.	80500.	7335.3		
32000.	33928.	56500.	29742.	81000.	6959.		
32500.	34765.	57000.	29285.	81500.	6580.9		
33000.	35520.	57500.	28828.	82000.	6205.3		
33500.	36207.	58000.	72993.	82500.	5823.6		
34000.	36833.	58500.	27897.	83000.	5440.5		
34500.	37422.	59000.	27443.	83500.	5056.1		
35000.	37908.	59500.	105830.	84000.	4667.4		
35500.	38374.	60000.	26499.	84500.	4281.		
36000.	38773.	60500.	26029.	85000.	3893.7		
36500.	39093.	61000.	25560.	85500.	3505.7		
37000.	39394.	61500.	25092.	86000.	3117.		
37500.	39625.	62000.	24625.	86500.	2727.8		

FIGURE 4.6: Coefficients of a 90kV energy spectrum simulated using methods presented by (Poludniowski et al., 2009).

4.3.3 Material properties

The test objects are assigned the chemical and physical properties of tungsten and the material file generated using the PENELOPE material database. The file is structured as described in Appendix A. The materials properties are listed one after another in the file and their order in this file corresponds to the material assignments in the geometry file. For example, if tungsten is the second material in the material file, then the test objects will be assigned the number ‘2’ in the geometry file to denote that they are made of tungsten. A sample material file definition is shown in Figure 4.9


```

PENELOPE (v. 2006) Material data file .....
Material: TUNGSTEN (74)
Mass density = 1.93000000E+01 g/cm**3
Number of elements in the molecule = 1
  atomic number = 74, atoms/molecule = 1.00000000E+00
Mean excitation energy = 7.27000000E+02 eV
Number of oscillators = 15 (E/P inelastic model)
  1 6.00000000E+00 0.00000000E+00 2.28694232E+01 0 30
  2 1.80000000E+01 3.31111111E+01 7.18146698E+01 74 30
  3 2.00000000E+00 4.40000000E+01 9.25312105E+01 74 30
  4 2.00000000E+00 7.40000000E+01 1.54936360E+02 74 30
  5 1.00000000E+01 2.47800000E+02 5.17720000E+02 74 30
  6 4.00000000E+00 4.23000000E+02 8.83634679E+02 74 30
  7 2.00000000E+00 4.89000000E+02 1.02141159E+03 74 30
  8 2.00000000E+00 5.92000000E+02 1.23653366E+03 74 30
  9 1.00000000E+01 1.83180000E+03 3.82552333E+03 74 8
 10 4.00000000E+00 2.27800000E+03 4.75799168E+03 74 7
 11 2.00000000E+00 2.57200000E+03 5.37204409E+03 74 6
 12 2.00000000E+00 2.81700000E+03 5.88376482E+03 74 5
 13 4.00000000E+00 1.02050000E+04 2.13147798E+04 74 4
 14 4.00000000E+00 1.18205000E+04 2.46821532E+04 74 2
 15 2.00000000E+00 6.95230000E+04 1.45209903E+05 74 1
Number of shells = 14 (Compton IA model)
  1 6.00000000E+00 0.00000000E+00 5.81368000E-01 0 30
  2 2.00000000E+01 3.42000000E+01 1.48370000E-01 74 30
  3 2.00000000E+00 7.40000000E+01 4.27000000E-01 74 30
  4 1.00000000E+01 2.47800000E+02 8.75000000E-02 74 30
  5 8.00000000E+00 4.81750000E+02 1.24500000E-01 74 30
  6 6.00000000E+00 1.80700000E+03 3.31000000E-02 74 9
  7 4.00000000E+00 1.86900000E+03 3.24000000E-02 74 8
  8 4.00000000E+00 2.27800000E+03 4.99000000E-02 74 7
  9 2.00000000E+00 2.57200000E+03 4.67000000E-02 74 6
 10 2.00000000E+00 2.81700000E+03 7.96000000E-02 74 5
 11 4.00000000E+00 1.02050000E+04 1.95000000E-02 74 4
 12 2.00000000E+00 1.15420000E+04 1.77000000E-02 74 3
 13 2.00000000E+00 1.20990000E+04 3.61000000E-02 74 2
 14 2.00000000E+00 6.95230000E+04 1.01000000E-02 74 1
*** RELAX: Z = 74, NO. OF SHELLS = 21, NO. OF TRANSITIONS = 726
 1 1s1/2 2 6.95230000E+04

```

FIGURE 4.9: An example of the materials in the material definition file.

the detector in the imaging geometry are also established in this section.

4.3.5 Simulation results

The simulation results using a 200×200 pixel, 10×10 cm detector are shown as samples. In the first simulation shown in Figure 4.10 the detector is divided into two parts which overlap each other. The X-ray source location and the beam width are changed to cover the entire detector using 2 slots. The test objects simulated using 2 slots are shown in Figure 4.10.

The simulations shown in Figure 4.11 show the same two test objects simulated using four slots which cover the whole detector. The X-ray source coordinates and beam width are controlled to get the data in the different regions of the detector.

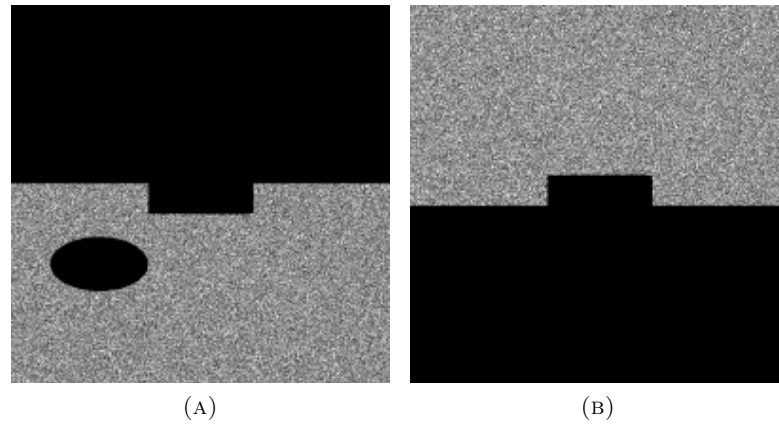


FIGURE 4.10: A sample simulation using two test objects and two slots covering the detector. Two overlapping slots are shown in (A) and (B).

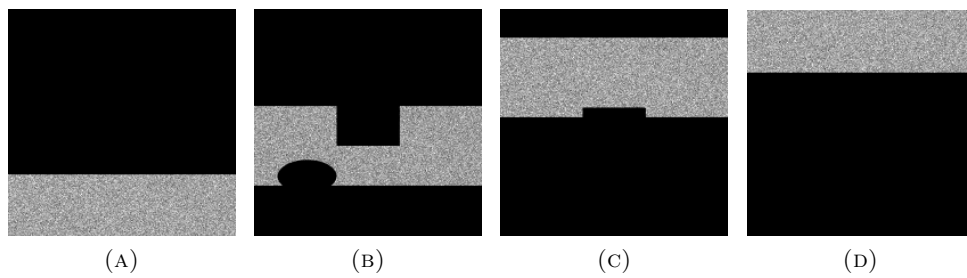


FIGURE 4.11: A sample simulation using two test objects and four slots covering the detector. Four overlapping slots are shown in (A), (B), (C) and (D)

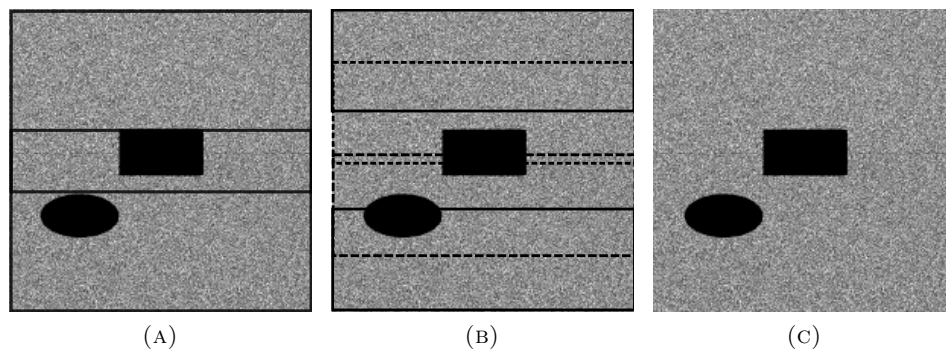


FIGURE 4.12: Locations of overlapping slots with 2 slots in (A) and 4 slots in (B). The combination of averaging of data is shown in (C).

The number of modules and surfaces increases as the complexity of the test object increases. The number of slots increase with the decreasing beam width to be able to cover the whole detector. The resolution of the detector, the beam width and the distance between two slots can be used to acquire overlapping data from the detector. As the overlap of the slots increases, the methods of combining the slots become important. The locations of the overlapping slots are shown in Figures 4.12A with 2 slots and Figure 4.12B with 4 slots. The slots were combined by averaging the data as shown in Figure 4.12C.

4.4 Summary

The various components, processes and parameters that are a part of slot-scanning imaging are discussed in this chapter. The modifications to the PENELOPE code system to extend it to slot-scanning imaging are also explained. A sample simulation of two objects is shown to demonstrate the effects of the different parameters like the slot width and location of the focal spot in the imaging chain on the resulting X-ray image. The parameters defined in the chapter are modified in Chapters 5 and 7 to represent different imaging systems.

Chapter 5

Simulating a slot-scanning X-ray imaging system

The simulation and validation of the Lodox Statscan (Lodox Systems, Sandton, South Africa), a slot-scanning X-ray imaging system, is described in this chapter. The system parameters for the Lodox Statscan and the imaging task are described and modifications to the PENELOPE code to simulate these are presented. An aluminium step wedge and a tungsten test object are simulated. These test objects are also imaged using the Statscan and the real and simulated images are compared using contrast, CNR, MTF, NPS and DQE. Section 5.1 describes the system parameters of the Lodox Statscan and Section 5.2 presents the test objects used for simulations. The modifications to the penEasy_Imaging code are discussed in Section 5.3, the calculations of MTF, NPS and DQE are explained in Section 5.4 and the results of the simulations are presented in Section 5.5. Section 5.6 discusses the results and compares it to previous work and Section 5.7 summarises the chapter.

5.1 Lodox Statscan: System parameters

The Lodox Statscan is a full body digital X-ray machine developed and manufactured by Lodox Systems (Sandton, South Africa). The Statscan produces a full body scan in 13 seconds. The slot-scanning feature of the Statscan results in low dose and good signal-to-noise ratio, producing a high resolution digital X-ray image. The effective dose

of an adult full body AP scan with tube parameters as 110kV, 140mA and collimator gap as 0.4mm is $99\mu\text{Sv}$ while the entrance dose is 0.12mGy (Irving et al., 2008). Figure 5.1 shows an image of the Lodox Statscan machine with the trolley, C-arm and the physical setup.



FIGURE 5.1: The Lodox Statscan machine at the UCT Faculty of Health Sciences.

A 90kV–100mA X-ray source with a narrow focal spot was used for simulations, and its energy spectrum was defined using Spekcalc (Poludniowski et al., 2009). The total scan time and the filtration and X-ray source properties were set to match those of the Statscan. The X-ray tube current and the charge per X-ray photon were used to determine the number of photon showers to be simulated. Spekcalc was used to define the filtration and the X-ray energy spectrum was modified accordingly. Collimation and beam formation was controlled using the PENGEOM package to be the same as that of the Statscan. The detector, a 10cm-by-10cm CsI layer of 0.6cm thickness, was defined

to have 2000-by-2000 pixels. The angles of the fan beam and the collimator width were set to cover a 10cm-2000pixel detector, with each slot having a beam width of 1mm. The step between slots was 1 pixel. The resolution of the detector was 50 microns for this work to match the resolution of the Lodox Statscan machine.

The detector of the Lodox Statscan consists of a scintillator, fibre optic taper and a CCD. The scintillator converts the X-ray photons into light photons. The scintillator also has specialised noise cancellation to reduce the noise in the output image. The fibre optic taper with the fibre optic face plate gather the light photons, transporting them to the CCD where the final X-ray image is formed. Figure 5.2 shows the basic workings of a X-ray detector with the different components.

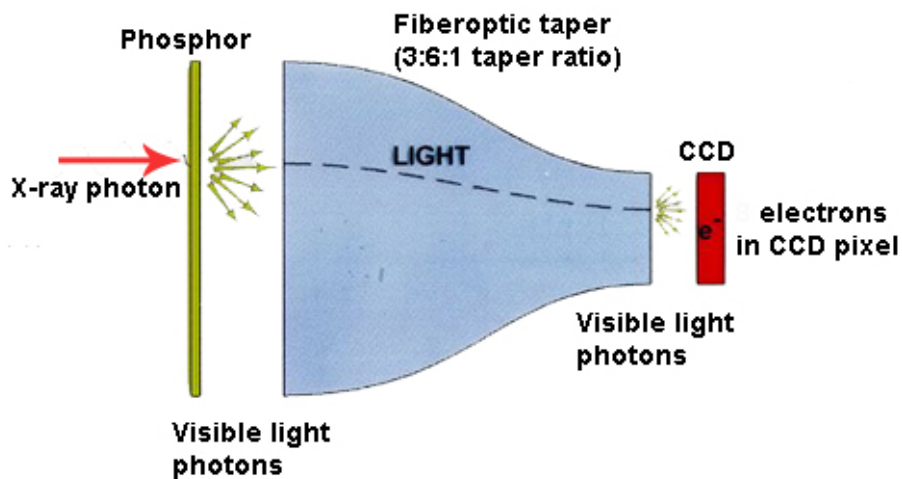


FIGURE 5.2: The components of a slot-scanning X-ray detector with the scintillator, fibre optic taper and CCD. Picture taken from (Mohajer, 2012).

5.2 Test objects

Two test objects were used to compare real and simulated X-ray images. An aluminium step wedge with 5 blocks of thickness 1mm, 2mm, 3mm, 4mm and 5mm was used to study the contrast and CNR of the simulated and real X-ray images. A 3mm tungsten block was placed at an angle to the detector for the calculation of the MTF, NPS and DQE functions, using the method described in de Villiers and de Jager (2003), described below. The aluminium wedge and the tungsten block were imaged using the

Lodox Statscan and simulated using a PENELOPE code that was modified for slot-scanning imaging. Both test objects are visualised using *gview2d* in Figure 5.3. The colours represent the different geometric components in the object geometry.

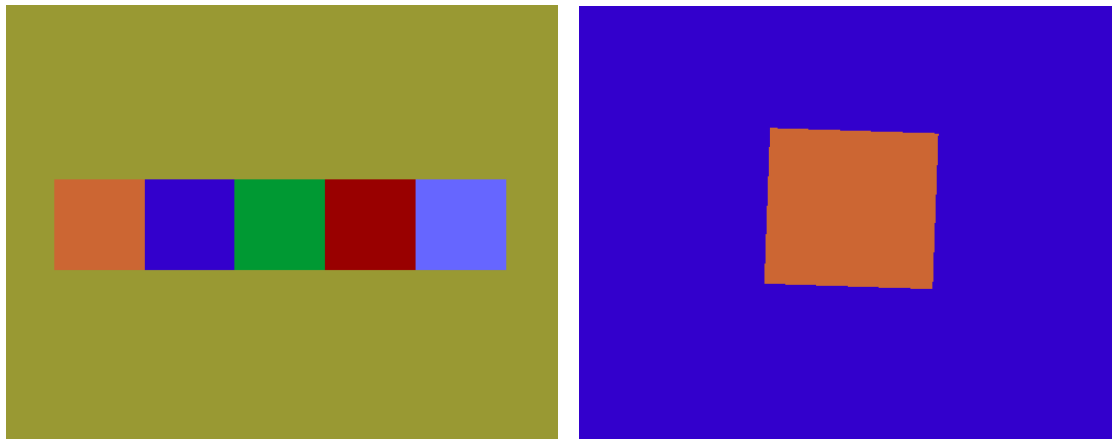


FIGURE 5.3: The test objects used for simulation and validation of X-ray images using the Lodox Statscan. The aluminium step wedge (left) has 5 blocks of aluminium with thicknesses of 1mm, 2mm, 3mm, 4mm and 5mm. The 3mm tungsten block (right) is placed at an angle to the detector for the calculation of DQE. Both test objects are visualised using *gview2d*.

5.3 Modification of `penEasy_Imaging` code

The simulation of X-ray images was performed using the parameters of the Lodox Statscan system. The filters were added to the X-ray source and the energy spectrum was modelled using `SpekCalc` (Poludniowski et al., 2009). The geometry, including variables like source-object-detector distances, object geometry, collimator width and effective beam width, was defined to reflect that of the Statscan machine. The simulation was divided into 1000 slots covering the area of the 10×10 cm detector, with a step size between slots of 1 pixel. The slots were simulated individually. The simulations were performed using a cluster of computers at the ICTS High Performance Computing (HPC) Center at the University of Cape Town, where slots were simulated in parallel to speed up the simulation process. Figures 5.4A and 5.4B show two individual slots being imaged. The images have been inverted, each pixel value in the image having been subtracted from 1, for ease of viewing. The imaged slots are filtered before they are combined in the Lodox Statscan. Gaussian filters are applied to each slot to attenuate the image data on the edges of each slot. Filtering reduces the edge noise on each

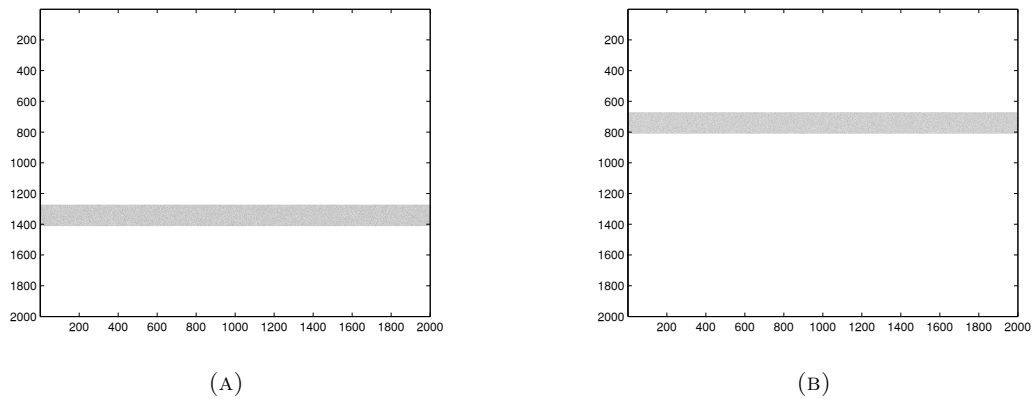


FIGURE 5.4: Examples of two imaged slots at different locations on the detector. The images have been inverted, each pixel value in the image has been subtracted from 1, for the ease of viewing.

slot. Such filtration is commonly to reduce noise. The simulated slots are filtered and combined in the same way as the slots in the real X-ray image.

5.4 Image quality metrics

The image quality metrics used to compare real and simulated X-ray images are described in this section. The MTF, NPS and DQE are introduced with respect to slot-scanning systems and the edge test method used to calculate them is described.

5.4.1 System resolution MTF

The edge test method to calculate the MTF in this thesis is based on (de Villiers and de Jager, 2003) which adapts the method specified in (International Electrotechnical Commission, 2003, Samei et al., 1998) to the LODOX slot-scanning X-ray imaging system. A polished tungsten object, with a sharp edge, is placed at 1 to 5 degrees in relation to the detector as shown in Figure 5.6A. The exact angle is calculated using the Nedler-Mead optimization method instead of a Hough transform, which is used in (de Villiers and de Jager, 2003). Nedler-Mead is a numerical method commonly used for nonlinear optimization. In this thesis it is used to optimise the angle of the object by rotating the image at different angles and detecting when the edge is parallel to the boundaries of the image. After the angle (angle ϕ in Figure 5.5) is determined, the image is rotated by that angle to make it perpendicular to the direction of the scan,

as shown in Figure 5.5. The edge spread function is obtained by projecting the pixels around the edge of the object to an axis which is parallel to the detector. The edge spread function comprises the raw image intensities at specific distances from the edge. A sample edge spread function is shown in Figure 5.6B. If the object in Figure 5.5 was perpendicular to the scan direction, and not at an angle, the edge spread function would look like a square wave. The line spread function in Figure 5.7A is obtained by numerical differentiation of the edge spread function and the MTF is the normalised magnitude of the one dimensional Fourier transform of the line spread function. The discrete Fourier transform is calculated using the fast Fourier transform (FFT) algorithm. The edge spread function and the line spread function can be considered the step response and the impulse responses of the system respectively. A sample MTF is shown in Figure 5.7B.

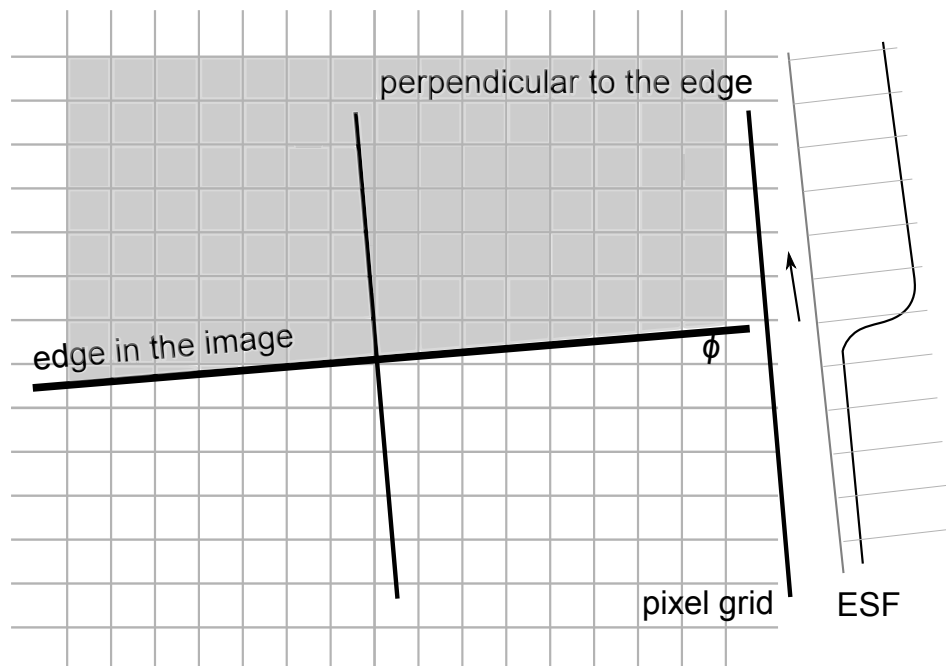


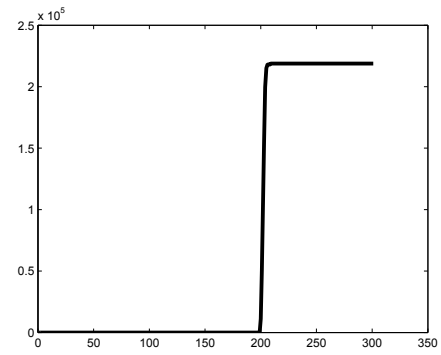
FIGURE 5.5: The calculation of the edge spread function (ESF). The angle ϕ is between 0 and 5 degrees.

5.4.2 Noise Power Spectrum

The noise power spectrum (NPS) is a measure of the noise in the X-ray image. In this thesis the NPS was calculated using the method described in (Stierstorfer and Spahn, 1999), using an uniformly exposed region in the image as shown in Figure 5.8A. It

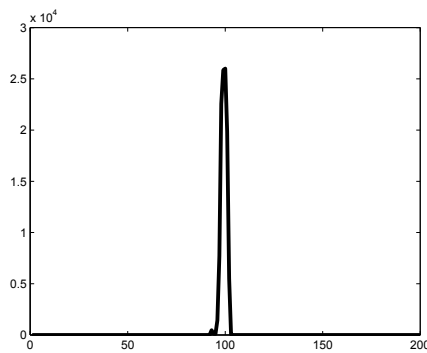


(A) Tungsten test object.

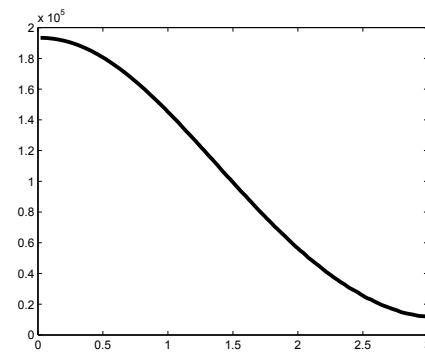


(B) Edge spread function.

FIGURE 5.6: The simulated X-ray image of the tungsten test object in (A) and the edge spread function in (B).



(A) Line spread function.



(B) Modulation transfer function.

FIGURE 5.7: The line spread function in (A) and then modulation transfer function in (B).

extends the one-dimensional technique of calculating the NPS to two dimensions. The uniformly exposed region is covered with overlapping $N \times N$ pixel squares, where N is a power of 2. For each of these partially overlapping squares the two-dimensional NPS is calculated using the following computationally efficient algorithm:

- The region is masked with a window function. A Bartlett or a Welch window is chosen to reduce frequency leakage due to the sharp edges of the square window. (Some window functions are shown in Figure 5.8B).
- The sums along the rows are calculated to produce a vertical slot, and the sums along the columns are calculated to produce a horizontal slot.
- The square of the one-dimensional FFT for the vertical and horizontal slots is calculated.

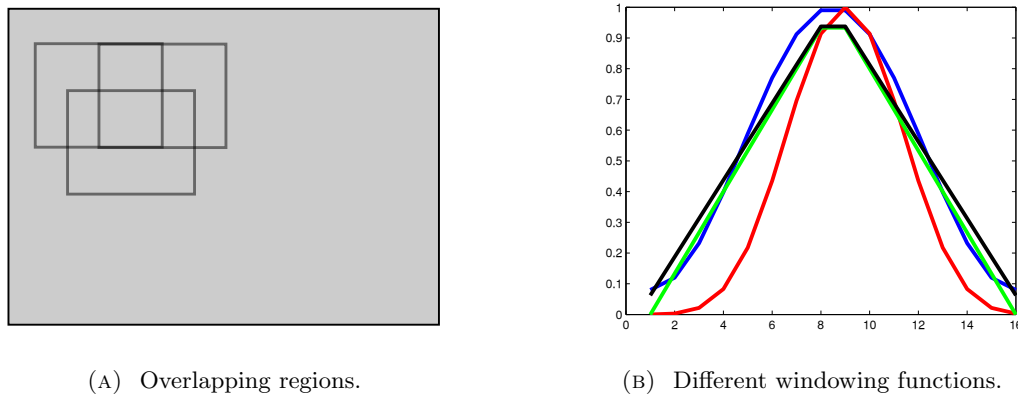


FIGURE 5.8: An example of three partially overlapping pixel regions, in an uniformly exposed region, is shown in (A). Squares overlap by half a square in both directions. Three of the squares are shown by thick lines. For each square the noise power spectrum is determined; averaging these spectra yields a smooth spectrum. The 1D window functions that can be used to avoid frequency leakage for $N = 16$ are shown in (B). Hamming (blue), Bartlett (green), Blackman (red) and triangular (black) windows are shown.

Spectra from all squares are averaged to get a smooth noise spectrum. A large value for N provides fine frequency binning, but there are fewer squares for averaging, resulting in a noisier NPS. Some papers use N values of 128 or 256, but a value of 16 or 64 is reasonable (Stierstorfer and Spahn, 1999). In this paper, a value of $N = 64$ is used and the number of sub-images or squares used is 200. The NPS at zero is not considered because it represents a DC offset.

5.4.3 Detective Quantum Efficiency

The DQE of any X-ray imaging system can be calculated using the MTF, NPS and dose measures with the help of Equation 2.4. In a slot-scanning imaging system, it is interesting to note that the MTF, NPS and DQE in the scanning direction will be different from those in the slot direction. The edges in the scanning direction will be sharper than the ones in the slot direction due to the scattered radiation. Edges in one direction being sharper than the other will lead to slightly different MTF, NPS and DQE functions. In the case of slot-scanning with TDI detectors the scattered radiation is very low, so these functions will be similar in value. Other factors like the binning of pixels can also affect the MTF, NPS and DQE measures. For these reasons it is important to use a consistent method of determining the DQE when comparing different systems.

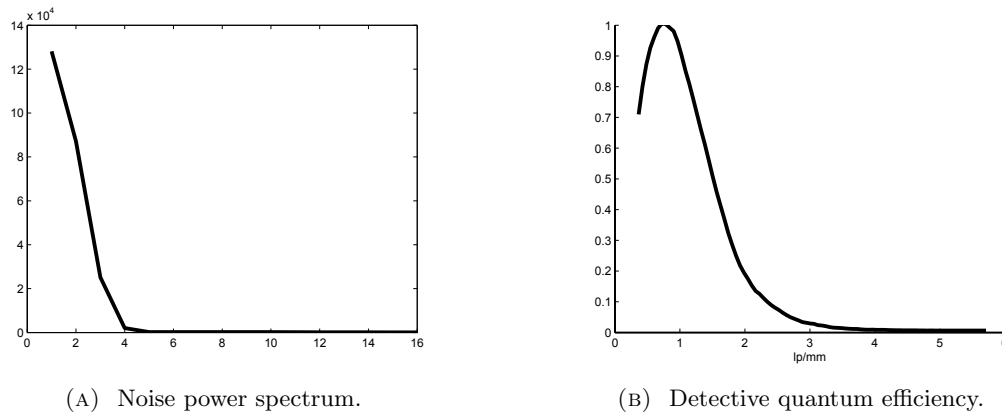


FIGURE 5.9: A sample NPS curve shown in (A) and a sample DQE curve shown in (B).

5.5 Results and validation

The real and simulated X-ray images for the aluminium and tungsten test objects are shown in Figures 5.10A and 5.10B respectively. A typical simulation time using the HPC cluster for a 10cm, 2000 pixel detector, with a slot width of 1mm and the step between slots of 1 pixel, was approximately 2 hours. This corresponds to 1000 slots and a detector resolution of 50 microns/pixel.

The real and simulated X-ray images are compared using region based quality parameters like contrast and CNR, and system-based quality parameters like MTF, NPS and DQE. Figures 5.11A and 5.11B show the image contrast and CNR for the real and simulated images. Four mutually independent regions are chosen in both images for the contrast and CNR calculations. The real and simulated images produce a range of image contrast and CNR ratios based on the region of pixels chosen. It can be seen from Figures 5.11A and 5.11B that the contrast and CNR calculated using regions in the simulated image fall inside the range of those calculated using regions in the real image. The CNR depends on pixel intensity and noise and a difference of approximately 20% between measured and simulated CNR is acceptable according to (Doyle et al., 2006). The results discussed in (Hussein et al., 2009) are obtained by estimating pixel values of the output X-ray image and comparing them to real X-rays using image contrast and CNR. The image contrast and CNR results in this paper are in agreement with Hussein et al. (2009); the contrast and CNR values for real and simulated X-ray images overlap. The limitation of region-based evaluation metrics is their dependence on the



FIGURE 5.10: The simulated (top) and real (bottom) X-ray images of the (A) aluminium and (B) tungsten test objects. The tungsten test object is at a slight angle (less than 2 degrees) to the detector for the DQE calculation.

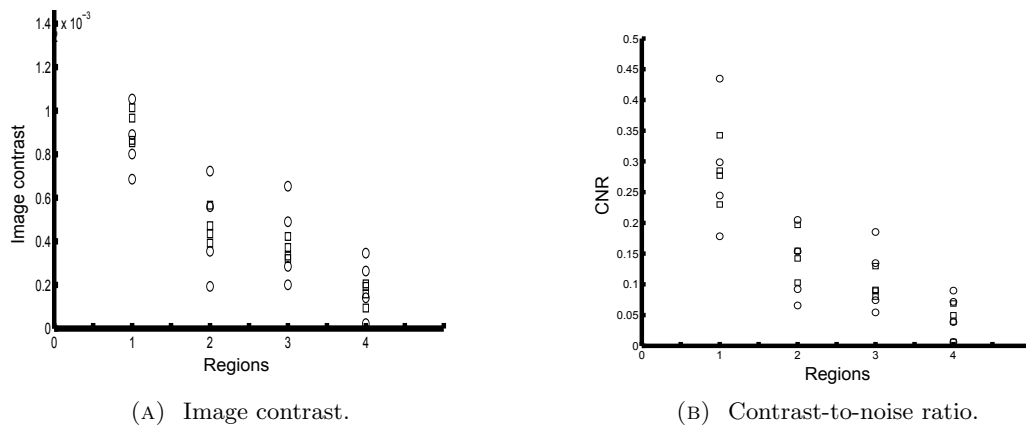


FIGURE 5.11: The image contrast and contrast-to-noise ratio for real (circles) and simulated (squares) X-ray images of the the aluminium test object using Equations 2.1 and 2.2.

pixel values in the particular region used to calculate them, as discussed in Section 2.4.1.

The binning of pixels was not simulated as it is an operation performed after the X-ray image acquisition. Binning was performed on the simulated data using localised filters to match the binning of the simulations to the binning of the Lodox scan.

A 3mm tungsten block, placed at an angle to the detector, was used for the calculation of the ESF, LSF and MTF. The MTF measures the transfer function characteristics of the system. The MTF is calculated using the ESF, the LSF and the edge-test method described in Section 2.4.4 (de Villiers and de Jager, 2003). The MTF of the real and

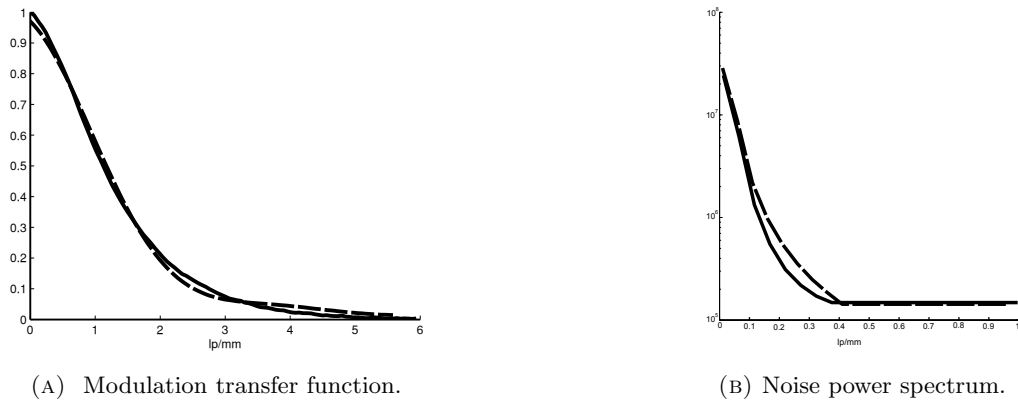


FIGURE 5.12: The MTF and the NPS of the real (continuous line) and simulated (dashed line) X-ray images.

simulated X-ray images is shown in Figure 5.12A. The MTFs are normalised between 0 and 1 for comparison, similar to the way it was done in (de Villiers and de Jager, 2003). The three parameters measured by the MTF are a macro (over a large area) transfer function, spatial resolution and image contrast. The MTF curves in Figure 5.12A show very similar characteristics for real and simulated images. The curves show similar transfer functions for the two images. The MTF of the simulated image has a lower magnitude for low frequencies but performs slightly better than that of the real image at higher frequencies.

The MTF curves for the real and simulated X-ray images, shown in Figure 5.12A, are high for low frequencies and have a similar fall-off. The MTF curves are normalised between 0 and 1, such that $\text{MTF}(0) = 1$, i.e., the zero frequency is set to 1 based on (de Villiers and de Jager, 2003). The similarity in the MTF curves shows that the spatial resolution of the real X-ray image is being correctly modelled in the simulated image. The magnitude of the NPS for the simulated image is similar to that of the real image and the fall-off is also consistent as shown in Figure 5.12B, plotted on a logarithmic scale. The shapes of the curves are similar. This is expected as the simulation is done for a flat-plane detector and does not simulate the specialised noise reduction mechanism used in the LODOX Statscan. The magnitude of the noise is higher for the simulated image but the nature of the noise is modelled correctly.

The DQE curves, calculated using Equation 2.4, are shown in Figure 5.13. The DQE is a combination of the MTF, NPS and the dose in the X-ray image. The DQE curves

show that the real and simulated systems have similar transfer function, noise and dose characteristics. The DQE curves have a low magnitude for low frequencies due to the high NPS. The fall-off of the DQE curves for real and simulated images are the same, showing similar system performances for higher frequencies.

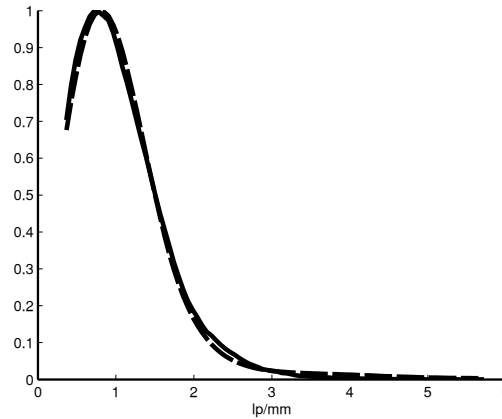


FIGURE 5.13: The DQE of the real (continuous line) and simulated (dashed line) X-ray images.

5.6 Discussion

Viswanathan and Balasubramaniam (2009) and Freud et al. (2000) provide X-ray simulation techniques useful for non-destructive testing. Although the basic geometric layout of the imaging chain is the same, there are some components that are specifically needed for X-ray imaging in a medical context, like specialised detector properties. The techniques described in Viswanathan and Balasubramaniam (2009) and Freud et al. (2000) are unable to simulate high resolution images. The work done in this thesis uses the basic geometric framework described in Freud et al. (2000) but extends it to medical imaging in general, and slot-scanning imaging in particular. Individual slots, specialised detectors and high resolution images can be simulated.

Boone et al. (2000) uses Monte Carlo methods and SIERRA code to estimate the scatter to primary ratios in mammography. Different parameters in the imaging chain are studied with respect to their effect on the scatter to primary ratio. The simulation system described in this thesis includes comprehensive photon scattering models and can be used to conduct experiments similar to the ones in (Boone et al., 2000). Different

parameters can be changed and their effect on the scattered radiation and the scatter to primary ratio can be studied.

There are several Monte Carlo implementations available and they can be used for simulating X-ray images. This work extends the general implementation of PENELOPE and penEasy.Imaging to model slot-scanning X-ray imaging systems. The validation of the simulated images with real X-ray images using objective image quality measures validates the simulation process. Such validation is the important ingredient that is missing from other Monte Carlo implementations described in Bottigli et al. (2004) and Golosio et al. (2014).

In improving any X-ray imaging system, it is useful to study how each variable in the imaging chain affects the X-ray image (Martin et al., 1999). If the effect of each variable is known, the variables can be optimised to improve the output X-ray image. The simulation method described in this paper can be used to understand the effect of different variables like X-ray source properties, materials, collimator width, material and thickness of the test object and the material and physical properties of the detector. The PENGEOm geometry package also gives a flexible framework to explore variables like source-to-detector distances, source-to-object distances, source-to-collimator distances, slot and beam widths and the step size between slots. These features of the simulation methods make them useful not only to study existing X-ray imaging systems but also to design new ones.

5.7 Summary

This chapter describes the simulation of the Lodox Statscan, a slot-scanning X-ray imaging system, using two test objects. The simulated images of the test objects are compared with real images using robust image quality metrics to validate the simulations. It is observed that the simulations closely model the Statscan machine, making the simulation process useful for the study of different parameters on the image quality and their optimization. The simulation system also provides flexible and easy-to-use tools for further investigations into the performance of slot-scanning systems.

Chapter 6

Applications of slot-scanning simulation

Reducing radiation dose while maintaining good X-ray image quality is the major trade-off in designing and optimizing X-ray imaging systems. The dose and the DQE, representing the image quality, can be estimated using simulations and design decisions can be made accordingly. The choice of geometry, including the source-to-detector, collimator-to-detector and the object-to-detector distances can be optimised using simulation process described in this thesis. Methods of reducing scatter, such as using anti-scatter grids or post-collimator angular rejection of photons, can also be studied with the aid of simulation. A study of scatter reduction techniques is described in Section 6.1.1. The optimal thickness and materials of filters to reduce low energy radiation can also be studied using simulation. Section 6.2 demonstrates the use of simulation to examine the effect of filtration on DQE.

6.1 Scatter reduction techniques

A study on the effects of different types of scatter on the X-ray image is described in this section. A brief overview of related work done is presented and the setup of the experiments is explained. The relationship between SPR and slot-width is investigated. The results from the experiments are discussed and compared to work done previously.

6.1.1 Background

Scattered radiation degrades the X-ray image quality by reducing the contrast and increasing the noise. Scatter-to-primary ratio (SPR), also known as the scatter fraction, is a commonly-used measure for scattered radiation. The SPR is a ratio of detected scattered photons to the total detected photons.

Monte Carlo simulations (Boone et al., 2000, Jing et al., 1998) have been used to estimate the SPR and scattered radiation in X-ray imaging systems. The SPR for a breast phantom of thickness 2-6cm ranged from 0.1 to 0.17 for slot width 4mm was quantified by (Jing et al., 1998). Boone et al. (Boone et al., 2000) investigated SPR for full-field and slot scanning digital mammography and developed the following empirical equation for the estimation of SPR in full-field digital mammography:

$$SPR = [a + b \times D^{1.5} + c \times thickness^{-0.5}]^{-1} \quad (6.1)$$

where D is breast diameter in cm $a = 2.35452817439093$, $b = 22.3960980055927$ and $c = 8.85064260299289$.

The data from Boone et al. (2000) and Jing et al. (1998) was used by (Hussein, 2008) to estimate the SPR for a slot-scanning mammography system by using a fitted equation. Using the breast thickness x as a variable the equation for SPR was estimated to be

$$SPR_{slot} = ax^3 - bx^2 + cx + d, \quad (6.2)$$

where a, b, c and d are curve-fitting coefficients and their values were provided for different breast thicknesses, x .

Several methods are available to reduce the scattered radiation in X-ray imaging systems and to decrease the SPR. Antiscatter grids and air gap techniques are used by (Barnes et al., 1980, Sorenson et al., 1980) to reduce the effect of scattered radiation. In digital X-ray imaging systems the use of slot-scanning reduces the SPR by a factor of two to three compared to other methods (Samei et al., 2005).

The SPR is directly proportional to the slot width (w) and inversely proportional to

the depth of the post-collimator slot (h), shown in Figure 6.1. Slot-scanning imaging uses a smaller detector area compared to full field imaging. Increasing the width of the slot increases the detector area used and in turn increases the scattered radiation on the detector. The post-collimator, shown in Figure 6.1, has a low angular acceptance and reduces the number of scattered photons. Figure 6.1 shows examples of two photons and their flight paths. The green lines are the paths that the photons would have taken if there was no scatter. The scattering media, usually the object to be imaged, causes the photons to deflect randomly. The red line shows a photon that lands outside the slot, and the blue line shows one that lands in the slot. Both are examples of scattered photons. The top view, shown on the right in the image, shows where the photons land on the detector. The black dot is placed in the front and top view as a point of reference. Figure 6.1 does not show all the scattered photons (only two) and does not show secondary scatter.

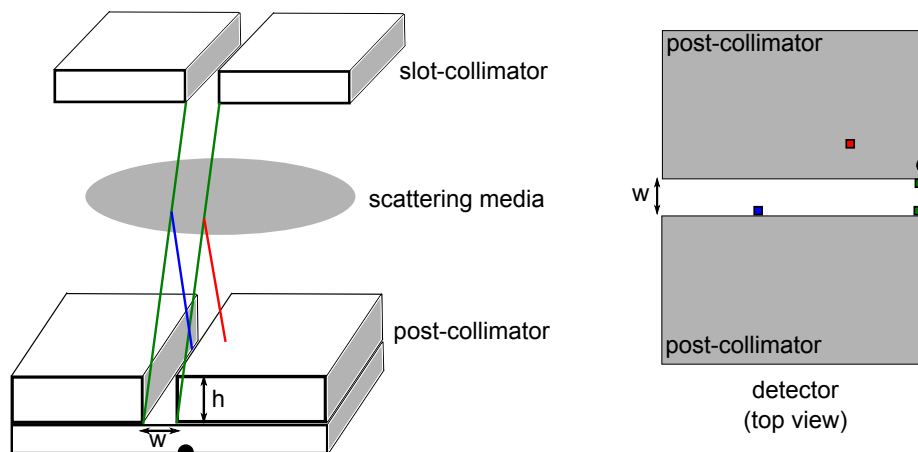


FIGURE 6.1: The effects of the depth of the post-collimator slot h and slot width w on scattered radiation. The red and blue lines show the scattered photons, outside and inside of the slot respectively, and the top-view shows where these photons landed using red and blue squares. The green lines and squares are the paths and locations of photons if there was no scatter. The black dot is placed in the top and front views for reference.

The work done by (Boone et al., 2000, Hussein, 2008, Jing et al., 1998) is based on curve-fitting and obtaining different constants to generate the SPR estimations. These constants can easily change with different experimental setups. Furthermore, there is no variable that represents the slot width in Equation 6.2, taken from (Hussein, 2008), in which the slot width-versus-SPR graphs are drawn based on the work done in (Boone et al., 2000, Jing et al., 1998). An example of a graph showing the relation between

slot-width and SPR, drawn by (Hussein, 2008) based on (Boone et al., 2000, Jing et al., 1998) is shown in Figure 6.2.

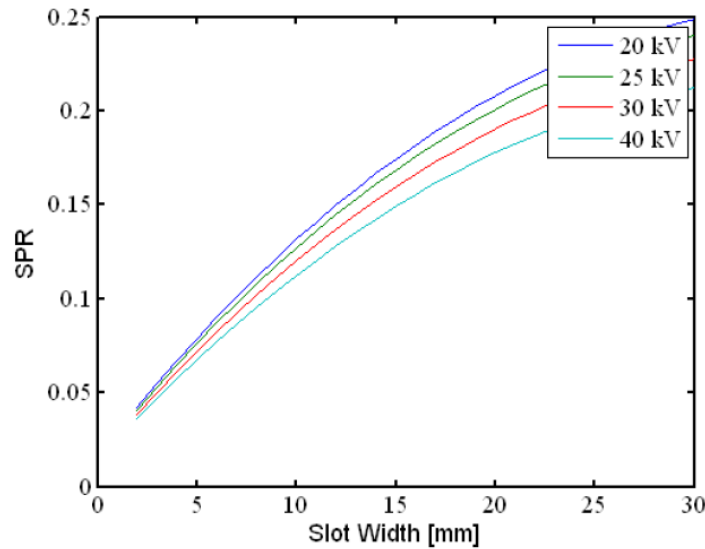


FIGURE 6.2: An example of a graph showing the relation between slot-width and SPR, drawn by (Hussein, 2008) (page 38) based on (Boone et al., 2000, Jing et al., 1998).

6.1.2 Methodology

A 3mm-thick tungsten block was simulated with and without anti-scatter grids using the same parameters. The slot-width was varied from 0.5mm to 6mm in order to see its effect on the scattered radiation. PENELOPE subroutines were used to measure different types of scatter, as described in Section 3.6, in relation to increasing slot-widths. The primary radiation was separated from the scattered radiation and the SPR was calculated.

6.1.3 Results

Figure 6.3A shows the tungsten block with scattered radiation and Figure 6.3B shows the tungsten block imaged with scatter reduction techniques. The effects of scatter can be seen in the two images, especially on the edges of the block. The scatter from all the slots is added when they are combined to form the final image and this increases the overall scatter.

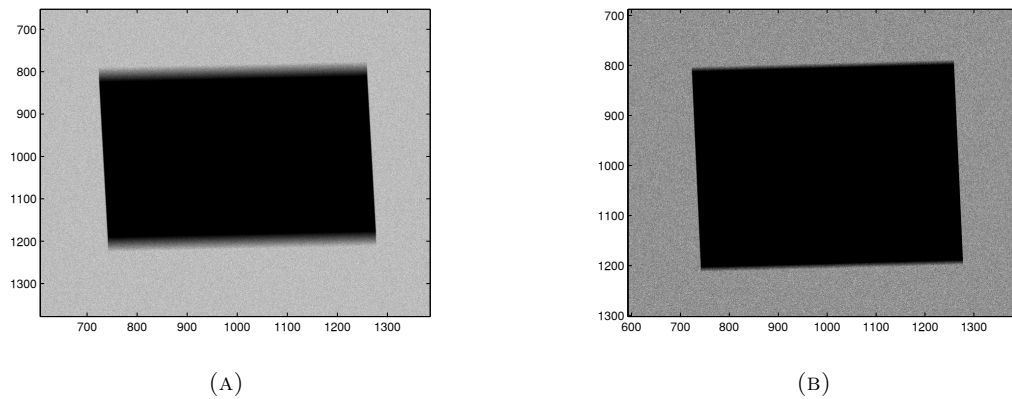


FIGURE 6.3: A 3mm tungsten block is simulated with and without the use of scatter reduction techniques. The image with scattered radiation (left) has blurry edges compared to the image with reduced scattered radiation (right).

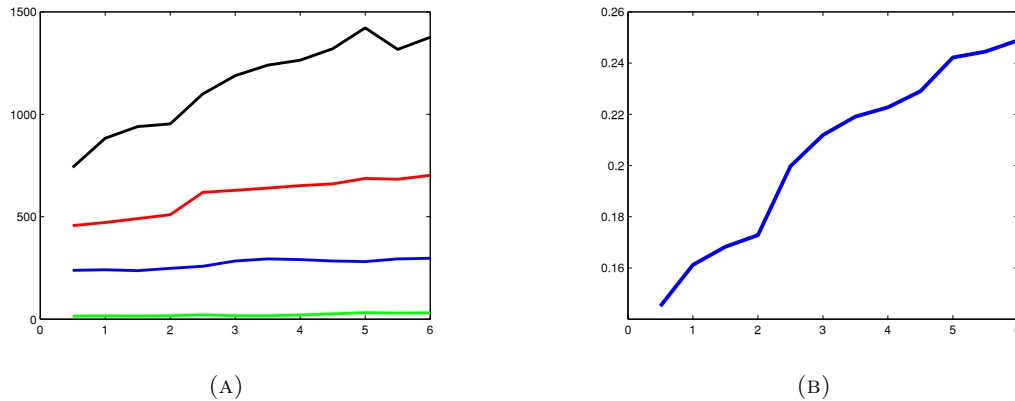


FIGURE 6.4: (A) The contributions of the different types of scatter at 90kV including Rayleigh scattering (red), Compton scattering (blue), multi-scatter (green) and secondary scattering (black) plotted against increasing slot width (in mm). The scatter-to-primary ratio versus the increasing slot width is shown in (B).

The Monte Carlo simulation process in this thesis helps in analyzing the contributions of the different types of scattering mentioned in Section 3.6. The contribution of the different types of scattering is shown in Figure 6.4A with increasing slot widths from 0.5mm to 6mm. It can be seen that secondary scatter and Rayleigh scattering contribute more than Compton scattering and multiple scattering is very low. Figure 6.4B plots the scatter-to-primary ratio for slots ranging from 0.5mm to 6mm. This graph is comparable to the graph derived by Hussein (2008) based on data from Boone et al. (2000), Jing et al. (1998) shown in Figure 6.2. Figures 6.5A, 6.5B, 6.6A, 6.6B, 6.7A and 6.7B show X-ray images of one slot 0.5mm wide, on the detector. These images are inverted, with each pixel value in the image subtracted from 1, to show the effects

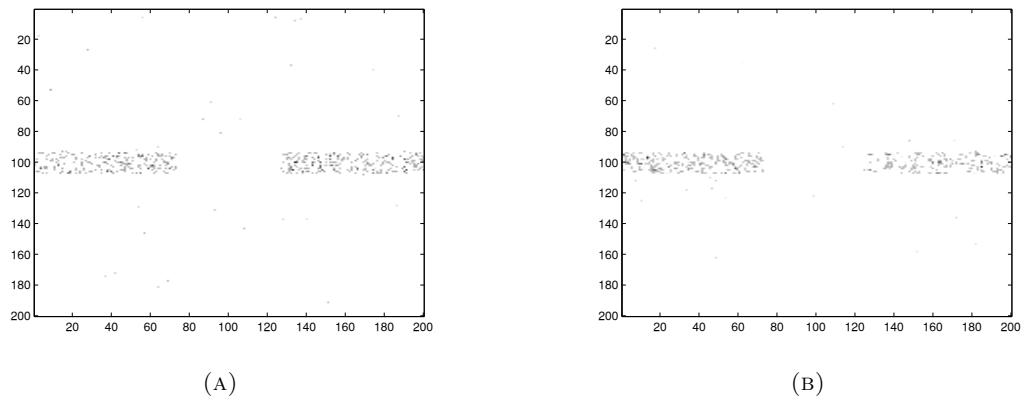


FIGURE 6.5: The contributions of Rayleigh scattering in (A) and secondary scattering in (B) in the X-ray image. These images are for one slot, 0.5mm wide with the 3mm tungsten block as the object being imaged.

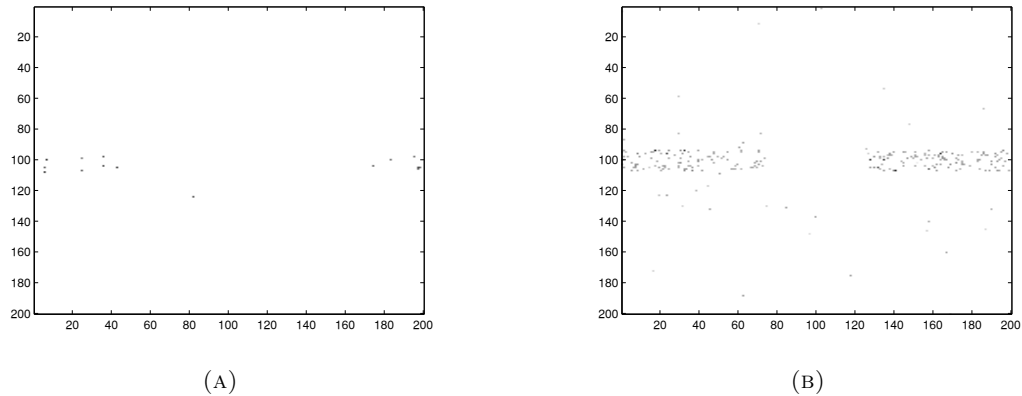


FIGURE 6.6: The contributions of multiple scattering in (A) and Compton scattering in (B) in the X-ray image. These images are for one slot, 0.5mm wide with the 3mm tungsten block as the object being imaged.

of the scattered radiation on the final X-ray image. The contributions of the different types of scattering plotted in Figure 6.4A can be seen in Figures 6.5A, 6.5B, 6.6A and 6.6B. Some scattered radiation is outside the slot, whereas most of it is contained inside it. It can be observed that multiple scattering (Figure 6.6A) and Compton scattering (Figure 6.6B) have a lower contribution to the total scatter than Rayleigh (Figure 6.5A) and secondary (Figure 6.5B) scattering. Figures 6.7A and 6.7B show the imaged slot without any scatter and the slot with both primary and scattered radiation respectively. Although the effects of scatter may be minimal in one slot, adding many slots compounds the effect of scatter in the resulting X-ray image.

The scatter profile of any imaging system depends on the imaging geometry and the

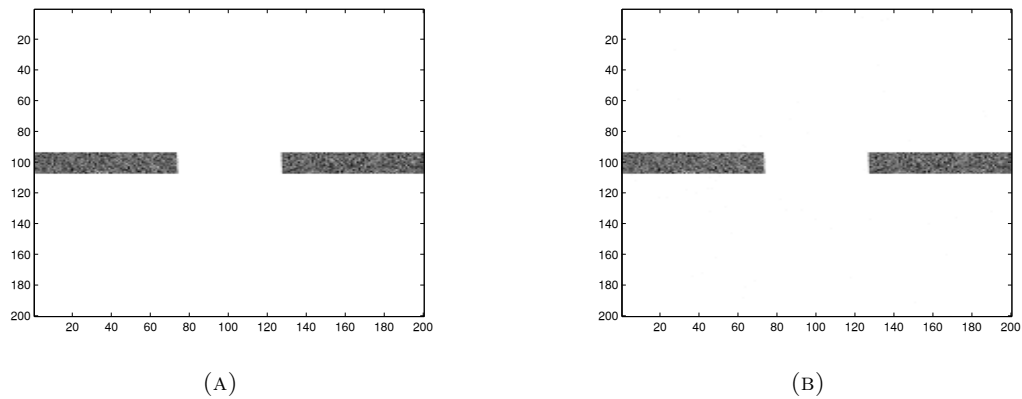


FIGURE 6.7: The X-ray image with no scattered radiation in (A), and only primary radiation and the X-ray image containing primary and scattered radiation in (B). These images are for one slot, 0.5mm wide with the 3mm tungsten block as the object being imaged.

scattering media. The slot width, as seen in Figures 6.4B, and the post-collimator play a role in the amount of scattered radiation as discussed in Section 6.1.1. The object to detector distance is another important variable affecting the scatter in a system because it dictates the distance covered by the scattered photons. The scattering medium is usually the object being scanned. In the example in this section, a simple tungsten block was used to study scatter. A more complex phantom or object will result in more scattering; the study of scatter is based on the imaging geometry and the object being imaged.

6.1.4 Discussion

The use of the simulation system described in this thesis for estimating the amount of scattered radiation is presented in this section. The effect of the use of an anti-scatter grids is shown, by comparing the resulting X-ray images and viewing the effects of the different types of scatter on the final image. The study of the effects of different types of scatter can be used to analyse which type degrades the image quality the most. Reducing the most dominant types of scatter can improve the image quality by reducing the noise power spectrum.

The effects of a change in slot-width on the resulting SPR is also studied. The graph plotted in Figure 6.4B is comparable to the one shown in Figure 6.2. Both graphs compare the effects of increasing slot-widths on the SPR. Figure 6.2 is plotted based on

the work done in Boone et al. (2000) which uses empirical equations and curve fitting. Figure 6.4B is plotted using scattered radiation measurements based on Monte Carlo simulations.

A method for the estimation of the scattered radiation and SPR based on Monte Carlo simulations is presented in this section. Also, previous work done by Boone et al. (2000) and Jing et al. (1998) is extended and the contributions of the different types of scatter radiation is studied. The use of the flexible geometry of PENELOPE also provides a way to study the effect of different phantoms and geometries on the SPR.

6.2 Filtration

Filters can be used to reduce dose in X-ray images. They filter out the low energy photons, which do not fully penetrate the human body and are absorbed in the tissue, thus increasing the radiation dose without contributing to the image quality. Filtration also degrades the image quality as it attenuates the input energy spectra. As an application of the simulation system presented in this thesis, the effect of filters of different thicknesses on image quality is studied. A brief background of the work done is presented and the experiments conducted are described. The results are discussed and compared with the work done by Perks et al. (2014).

6.2.1 Background

Entrance dose is a measure of radiation at the point where the X-ray beam makes contact with the patient, while effective dose is the radiation that enters the body taking into account the radio sensitivities of different organs (Irving et al., 2008). The effective dose is estimated by using the entrance dose as a Monte Carlo simulation which uses mathematical phantoms to represent organs (Irving et al., 2008). The main aim of using filters is to remove low energy X-rays that do not contribute to the image quality. It has been previously shown that using a 0.1mm copper filter on the Lodox StatScan can significantly lower the radiation dose while maintaining diagnostic image quality at high kV exposures (Trauernicht et al., 2012).

An imaging study done on cadavers (Perks et al., 2014) showed that using filtration reduced the dose while maintaining diagnostic image quality. A dose prediction model was developed to estimate patient doses based on input parameters. Image quality was quantitatively assessed using the DQE, by imaging a 3mm-thick tungsten block using aluminium filters of thickness 0.9mm, 1.8mm and 2.7mm. The X-ray imaging was performed using slot-scanning with the Lodox Statscan machine. The effect of the reduction in image quality due to filtration was also studied qualitatively by showing X-ray images of phantoms and cadavers to radiologists. The aim of the study was to reduce radiation dose for paediatric patients. The entrance dose was reduced by 36% on average while maintaining diagnostic image quality (Perks et al., 2014).

An explanation of the reasons for low dose in slot-scanning systems is provided in (Irving et al., 2008). The beam geometry, the low noise of the digital detector, low scattered radiation and the use of filters were the main reasons for the low dose. Aluminium and copper filters were used by (Perks et al., 2014) to reduce dose in paediatric X-ray images. Molybdenum filters were used at lower kV ratings (30 to 35kV) to study their effect on the scattered radiation in a slot-scanning mammography system by Jing et al. (1998). These studies show that the dose is reduced when filters are used.

The aim of radiography is to obtain images with adequate quality for clinical purposes with the minimum radiation dose to the patient (Martin et al., 1999). Evaluating the diagnostic quality of X-ray images is a complex task as the interpretation is dependent on a human observer; the complexity is increased further because images can be evaluated differently for different diagnoses by the same radiologist (Martin et al., 1999). The evaluation of image quality can be based on the opinion of a radiologist, making an objective evaluation difficult. This is seen in (Perks et al., 2014), where some radiologists scored the filtered images ‘equivalent’ and others scored them ‘slightly better’, in comparison to unfiltered images.

Koedooder and Venema (1986) studied the effect of 27 different filter materials on the radiation dose. A computer algorithm was developed to calculate the absorbed dose and was validated using measurements done using a Siemens X-ray machine. It was concluded that conventional filtering materials like aluminium and copper worked equally well in reducing dose compared to specialised materials suggested in previous studies,

like gadolinium. The advantage of holmium filters over aluminium filters, under the same imaging and X-ray tube conditions, was minimal. The results in (Koedooder and Venema, 1986) were also supported by experiments done in (Regano and Sutton, 1992), using earth salt solutions as specialised filters and concluded that significant reduction in absorbed dose was achieved when the X-ray tube loads were increased considerably. Under the same conditions there was no difference between using aluminium filters and specialised material filters. The X-ray energy spectrum filtered with 2.5mm to 3.0mm aluminium filters reduced dose while maintaining good image quality (Regano and Sutton, 1992).

6.2.2 Methodology

Aluminium filters of different thicknesses (0.9mm, 1.8mm, 2.7mm and 3.6mm) were placed between the X-ray source and a tungsten block, which served as a test object for the simulation. The thicknesses were chosen to be the same as the study done in (Perks et al., 2014).

The tungsten block was simulated using slot-scanning and filters of different thicknesses and the resulting X-ray images were compared using MTF, NPS and DQE. The edge test method was used to calculate the MTF, NPS and DQE. The case of no filtration was used as reference. For assessing the effect of the filters on these measures, the MTF and DQE measurements were normalised with respect to those without any filtration. This was done to study the loss of MTF and DQE due to filtration.

6.2.3 Results

The different X-ray energy spectra resulting from the filters, calculated using SpekCalc (Poludniowski et al., 2009), are shown in Figure 6.8. The low energy photons are filtered out to reduce the dose. This can be observed in the spectra, thicker filters result in greater attenuation of the X-ray energy spectrum. Dose reduction using additional filters in this slot-scanning system has previously been studied in Irving et al. (2008). The magnitude of the characteristic K lines reduces with the increase in the thickness of the filter, but they occur at the same energies. The location of the characteristic K lines is based on the anode material used, so the lines are expected to remain at the same

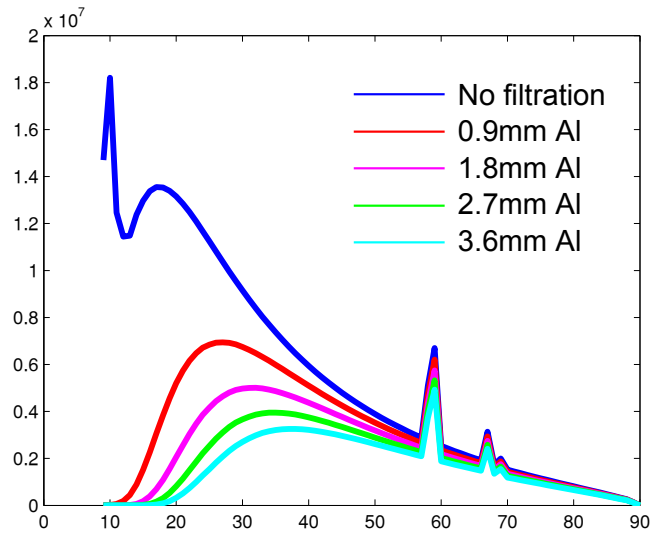


FIGURE 6.8: The changes in the X-ray energy spectrum due to the different filters. The low energy photons are filtered out to reduce dose.

locations. This suggests that the use of filters only scales the magnitudes of the energy spectra and the DQE and image quality are expected to be scaled in a similar manner.

Figures 6.9A and 6.10 show that as the thickness of the filter increases, regardless of the material used, the DQE decreases. The MTF and NPS also show similar decreases. This is expected as the thickness of the filter determines how much signal is blocked out. The decrease in scattered radiation due to filtration also reduces the noise in the system. The NPS due to filtration is reduced in a similar manner to the MTF and the DQE functions as shown in Figure 6.9B. As the thickness of the filter increases, the signal decreases and the noise power spectrum also decreases.

The shape of the DQE function represents image contrast, signal-to-noise ratio and spatial frequency behaviour. The amplitudes of the MTF and DQE functions are lower for thicker filters because the input X-ray spectra is attenuated by the filter. Using filtration only changes the amplitude of the DQE and not the spatial frequency characteristics, which are the basis for visual image quality.

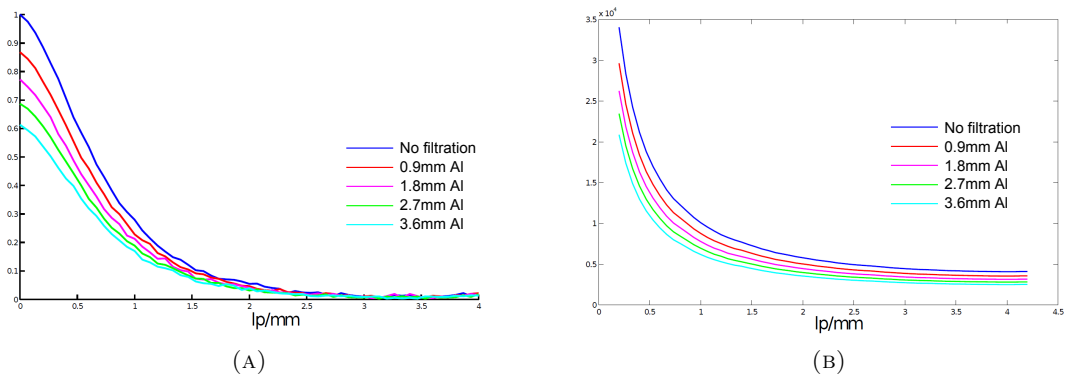


FIGURE 6.9: The modulation transfer function, shown in (A), calculated for different thicknesses of Al filters. The amplitude of the MTF decreases with an increase in the thickness, but the frequency characteristics are retained. The noise power spectrum, shown in (B), averaged over 200 overlapping sub-images. A Bartlett window is used to avoid frequency leakage and the DC offset has been excluded.

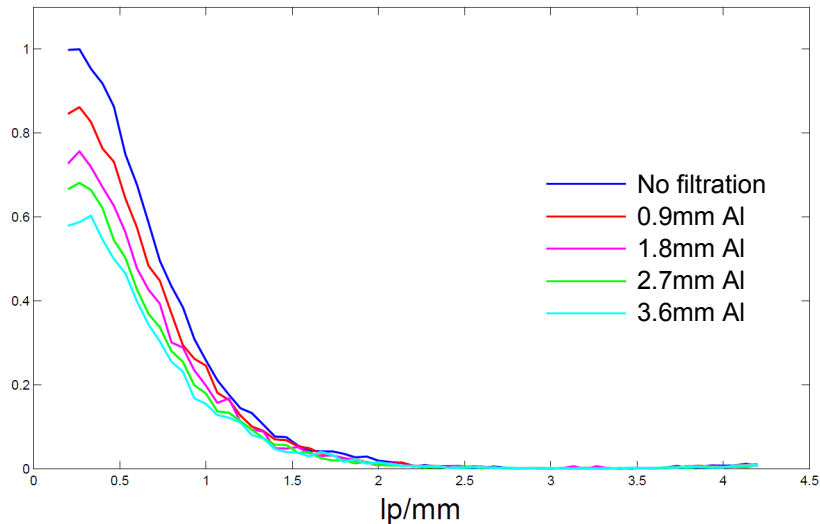


FIGURE 6.10: The detective quantum efficiency, for the different filters calculated using the MTF and the NPS. The DQE is normalised to compare the filtered image DQEs with the unfiltered image DQE.

6.2.4 Discussion

The work done in (Perks et al., 2014) reduced the radiation dose while maintaining diagnostic image quality. The experiments done to assess the image quality quantitatively were performed by imaging a test object using aluminium filters of varying thicknesses. The thicknesses used were 0.9mm, 1.8mm and 2.7mm. It was observed that increasing the thickness of the filter decreases the DQE. The same test object was simulated using the same parameters and filters in this thesis. Aluminium filters of matching thicknesses

were used. The DQE of the simulated images as shown in Figure 6.10 also decreases with increasing filter thicknesses as observed in (Perks et al., 2014). This work demonstrates the use of the slot-scanning simulation tool to show similar results to those found in an imaging study.

(Regano and Sutton, 1992) noted that aluminium filters of thicknesses between 2.5mm and 3mm maintain good image quality. The 3.6mm filter is used for simulations in this work to see the effect of filters above 3mm. Figure 6.10 shows that the DQE falls to less than 60% because of the use of this filter. This suggests that image quality may be compromised and supports the claim made by Regano and Sutton (1992) that aluminium filters less than 3mm in thickness can be useful for maintaining image quality.

Regano and Sutton (1992) and Koedooder and Venema (1986) also concluded that conventional filters work just as well as filters made from special materials like holmium and gadolinium, under the same operating conditions. Regano and Sutton (1992) used rare earth salt solutions as cheaper substitutes to specialised materials. The simulation process described in this thesis can be used to simulate specialised materials using their chemical compositions to study their effects on image quality. Materials like holmium (atomic number 64) and gadolinium (atomic number 67) are part of the PENELOPE materials database. This will enable studies of materials that are not readily available for physical experiments.

In some applications, a combination of two or more filters of different thicknesses is used (Koedooder and Venema, 1986). These types of filters can be simulated in a similar manner as shown in this section.

Chapter 7

Simulating a breast phantom on a slot-scanning digital mammography system

A tissue-equivalent breast phantom for digital mammography is simulated using the parameters of the CapeRay (Westlake, South Africa) Soteria machine, a breast imaging prototype. The simulation of this breast phantom demonstrates the use of the simulation process on a complex object with many components and materials. Validation is performed on a 3mm tungsten block that is imaged using Soteria and simulated using the Monte Carlo process described in this thesis. The Soteria slot-scanning mammography machine is shown in Figure 7.1. The system parameters for simulation of the mammography system are discussed in Section 7.1 and the mathematical breast phantom used is defined in Section 7.2. Section 7.3 explains the modifications to the penEasy_Imaging code to simulate the phantom on a slot-scanning mammography system. The results are presented and validated using MTF, NPS and DQE in Section 7.4 and Section 7.5 provides a discussion of the results and compares the work done to previous studies.

7.1 System parameters

Figure 7.2 shows a schematic diagram of a typical slot-scanning digital mammography system. The imaging geometry is presented with the source being collimated and X-ray



FIGURE 7.1: The CapeRay Soteria mammography machine.

photons passing through the object on to the detector. In mammography systems, the breast is compressed to improve X-ray penetration. The X-ray image is generated by combining the slots acquired as the X-ray source and detector move across the object while imaging. The grey region in the image shows one such slot on the detector. The X-ray source has a 90-10% tungsten-rhenium anode with a diameter of 100mm and a focal spot of 0.3mm measured at 25kV and 100mA. The tube has an inherent 0.5mm beryllium filtration and a 0.5mm aluminium filter is added. The source-to-detector distance of the Soteria machine is 650mm, the source-to-collimator distance is 82mm, and the object-to-detector distance is 13mm. The X-ray beam width is 7mm. The pixel resolution is 54 microns and a 10×10cm detector is used for simulation. The detector is operated in TDI mode.

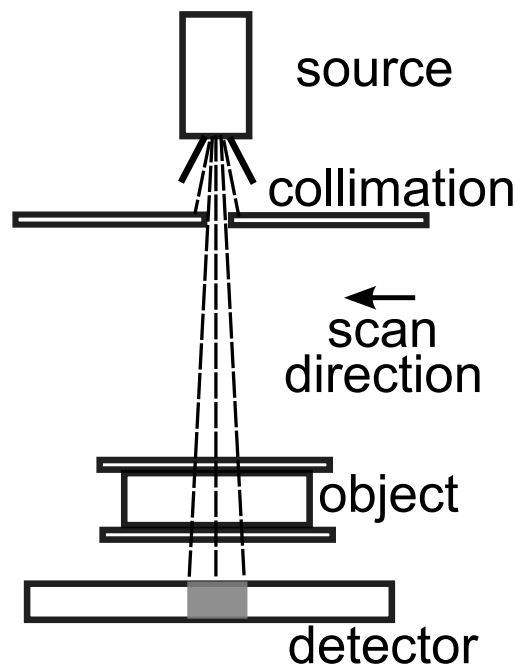


FIGURE 7.2: A simple schematic diagram of a slot-scanning mammography system. The X-ray source is collimated to create a slot on the detector, the grey region. The slot direction is coming out of the page and the scan direction is from right to left on the page. The object, a breast or a breast phantom, is compressed to improve the image quality.

7.2 Phantom definition

The definition of the tissue-equivalent breast phantom is based on the CIRS (Computerised Imaging Reference Systems, Norfolk, VA, USA) breast phantom designed for mammography (Model 011 A). A complex mathematical model for the phantom was defined using the PENGEOM package. The components of the mathematical phantom are shown in Figure 7.3. The outer body of the phantom is modelled as half a sphere with all the other components and modules inside it. The thickness of the outer body corresponds to the thickness of the breast and can be changed. The region marked as 1 in Figure 7.3 is a wedge simulating soft tissue ranging from 100% glandular to 100% adipose. The center block in the wedge models 50% glandular and 50% adipose tissue. The outer body is also models 50% glandular and 50% adipose tissue so they have the same material properties. The region marked as 2 is a set of four spheric masses of decreasing diameter. These masses are made of 70% glandular and 30% adipose tissue equivalents. The CIRS phantom has 7 spheric masses, and differs from the mathematical

model. The region marked as 3 comprising a group of Nylon strings of different thicknesses. The location and orientation of the strings in the CIRS phantom is different, but the thicknesses used are the same. The region marked as 4 are Calcium Carbonate (CaCO_3) specks of different sizes. These represent calcifications in the breast tissue. The region marked as 5 is a line pair tool to test the resolution of the image. This model is similar to the mathematical model used by Hussein et al. (2009) but is a 3D extension of that model. The models for glandular and adipose tissue are based on the predefined material files in PENELOPE. These files use the data from ICRU (1996) to model soft tissue. Other materials used for the simulation, like CaCO_3 and Nylon, are also modelled using PENELOPE's materials database. Figure 7.4 shows the different modules in the phantom viewed using *gview2d*.

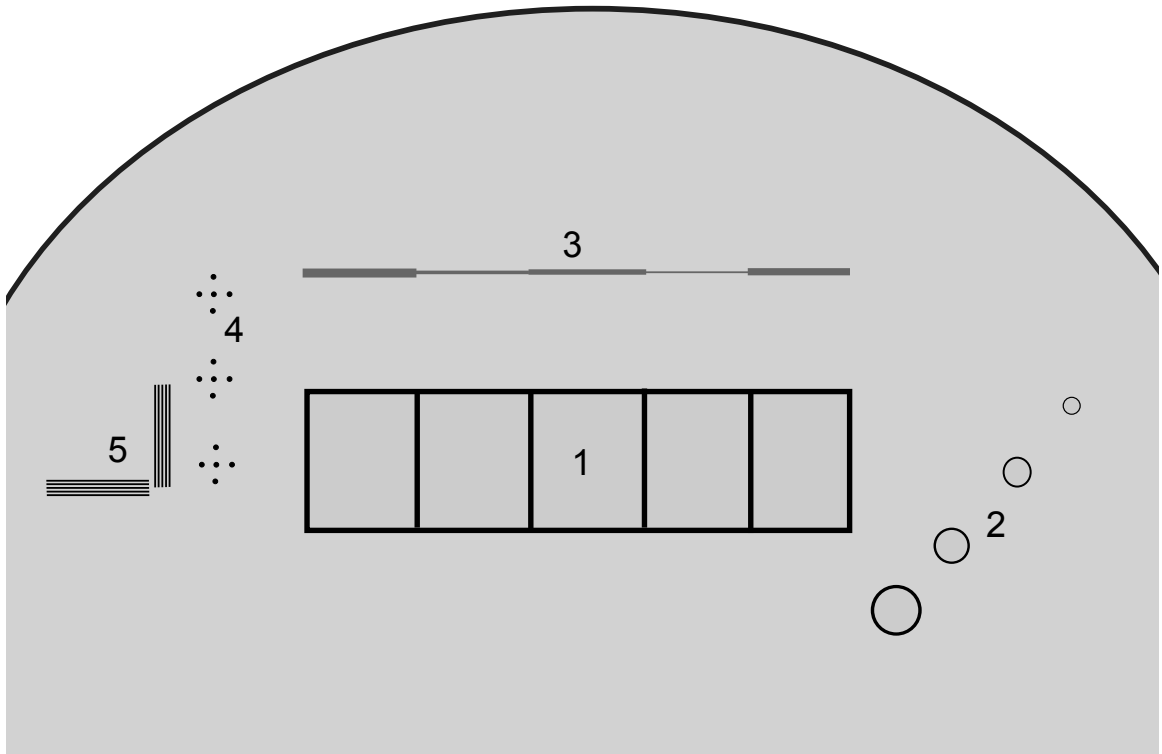


FIGURE 7.3: The mathematical tissue-equivalent phantom for digital mammography. Areas within the phantom simulating (1) 100% glandular, 70:30 glandular/adipose, 50:50 glandular/ adipose, 30:70 glandular/adipose, and 100% adipose tissues. (2) four spheric regions simulating 70:30 glandular/adipose tissue; (3)nylon fibres of different size; (4) microcalcifications of different sizes (CaCO_3); (5) line pair tools for measuring the system resolution.

This mathematical model is more complex than the aluminium wedge used in Chapter 5 as it has many components, materials and geometries. This model is a good test

for the simulation process because it is tissue-equivalent. The CaCO_3 specks can be used to test the performance of the simulation process in representing very small objects. The line pair tool provides a way to quantify the spatial resolution of the simulation process. The Nylon fibres not only provide a contrasting material but also changing thicknesses. The spheric masses are at an angle making them geometrically challenging and again test the modelling of small objects. All these components are inside an outer body and the whole model is defined in three dimensions, making it comprehensive. The *gview2d* package can be used to view the geometry of the mathematical model in all three dimensions.

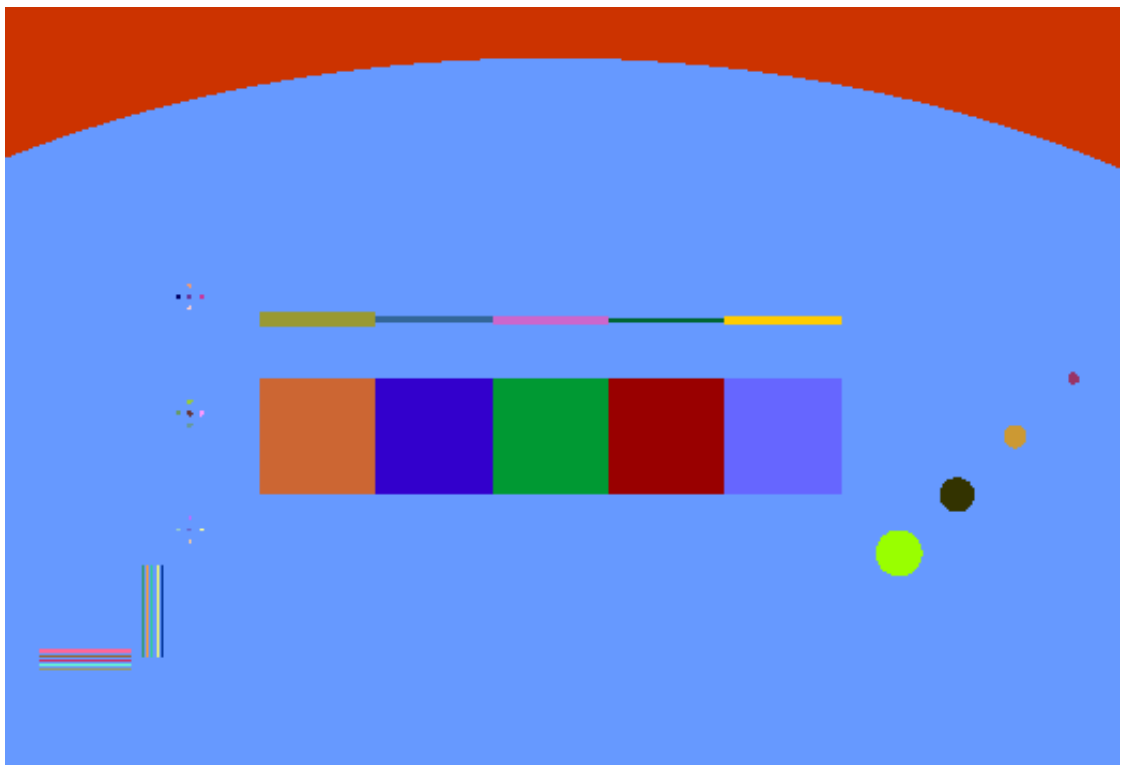


FIGURE 7.4: The tissue-equivalent phantom used simulation, viewed using *gview2d*. The different colours are used to visualise different components of the model.

7.3 Modification of `penEasy_Imaging` code

The simulations and X-ray images were taken at 28kV using the system parameters described in the previous sections. The aluminium and beryllium filters are added to the X-ray source and the energy spectrum is modelled using *Spekcalc* (Poludniowski et al.,

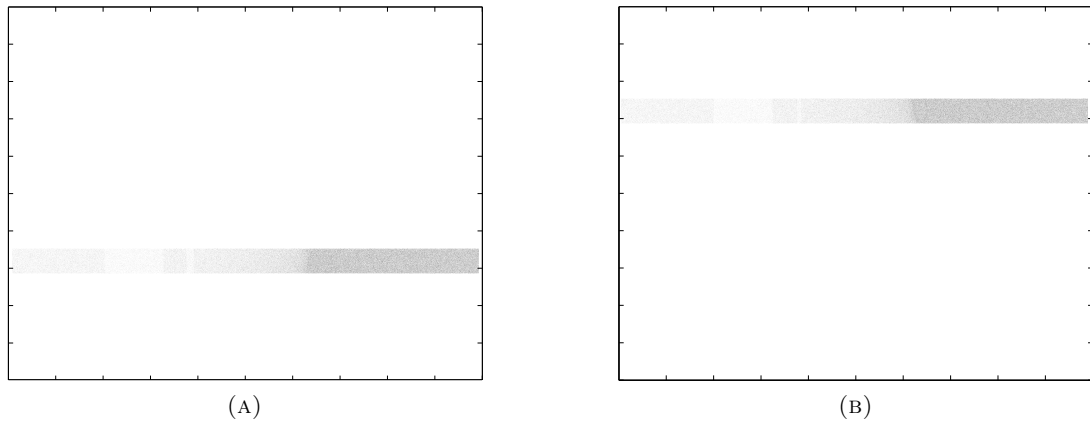


FIGURE 7.5: Examples of two imaged slots at different locations on the detector. The images have been inverted for the ease of viewing.

2009). The geometry of the system reflects that of the Soteria machine. The simulation is divided into 1000 slots covering the area of the 10×10 cm detector, with a step size between slots of 1 pixel. The simulation was run in parallel and the slots were simulated individually. Figure 7.5a and 7.5b show two individual slots with the CIRS phantom being imaged. The images have been inverted for ease of viewing.

The imaged slots on the Soteria machine are combined by filtering them and then adding them together to form the final X-ray image. A Gaussian filter is used to filter the data on the edges of each slot, effectively reducing the slot width on the detector. This filtration technique was implemented on the simulated slots using similar filters on the edges of the slots. The simulation process described in this thesis images individual slots, making it easier to filter slot data. Previous work on simulation of a mammography system done by Hussein (2008) and Hussein et al. (2009) does not allow for such filtration.

7.4 Results and validation

The raw data from the simulated X-ray image is shown in Figure 7.6. The model has been simulated including all its components and their properties. The top and bottom edges of the simulated image appear slightly low in intensity because this area is not covered by as many slots as other regions in the image. This is a common slot-scanning artefact on the edges of the image. The step wedge has been simulated correctly and the intensity of the centre block in the wedge is the same as the background because

the material properties of both regions are the same. The four blocks in the step wedge appear to be similar in intensity in the image because the difference between them is relatively smaller compared to the intensity of the background and the CaCO_3 specks. The edges of the wedge are sharp because of the filtration done on the individual slots. The

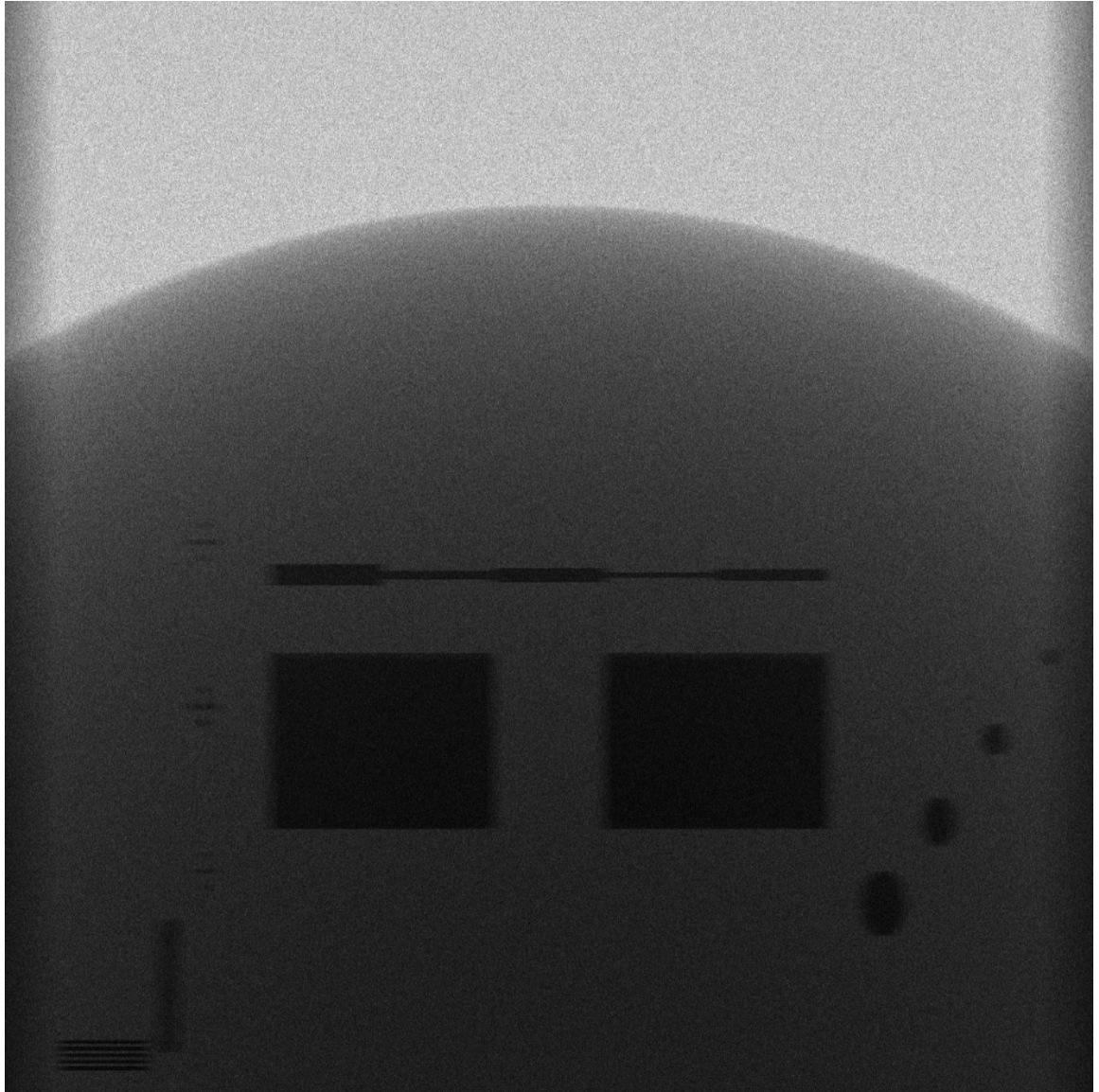


FIGURE 7.6: The simulated image of the tissue-equivalent breast phantom. All the components are visible and their positions and orientations are correctly simulated. The image displays raw, unprocessed data.

Nylon fibres are simulated correctly as shown in Figure 7.7. The difference in thickness is clearly visible and the position and orientation of the fibres are correct. The edges perpendicular to the slot direction are sharper than the ones perpendicular to the scan direction. This is due to the addition of the slots and is a characteristic of slot-scanning

X-ray imaging. Post-processing techniques are used to correct this effect, but it is visible in the raw data shown. The centres of the spheric masses shown in Figure 7.8a

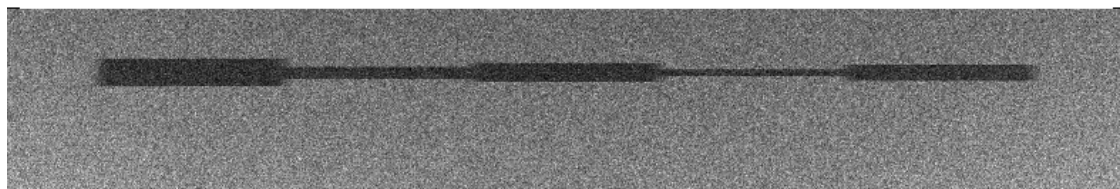


FIGURE 7.7: The location, orientation and thickness of the Nylon fibres is correctly simulated. The image displays raw, unprocessed data.

are equally spaced but their varying diameters give the impression of varying spacing between them. Although all the masses have same material properties, the larger one appears to be darker in intensity because of its diameter. These spheric masses, their location and thicknesses, have been correctly simulated. The CaCO_3 specks are clearly visible, although their edges perpendicular to the slot direction are sharper than the ones perpendicular to the scan direction. Their location and orientation in the shape of a + sign is simulated correctly. The line pair tool clearly displays the difference between the edges in the two directions. The edges perpendicular to the slot direction are sharper than the ones perpendicular to the scan direction. This is a characteristic of slot-scanning imaging and it is correctly modelled in the simulation process. The effects of sharper edges in one direction compared to the other on the MTF and DQE are discussed in Section 7.4. The results of the simulated X-ray image show that the geometry and materials are correctly simulated.

The 3mm tungsten block was simulated and imaged using Soteria to compare the two



FIGURE 7.8: The spheric masses with the same material properties but different diameters are simulated correctly in (A). The CaCO_3 specks are also clearly visible in (B). The image displays raw, unprocessed data.

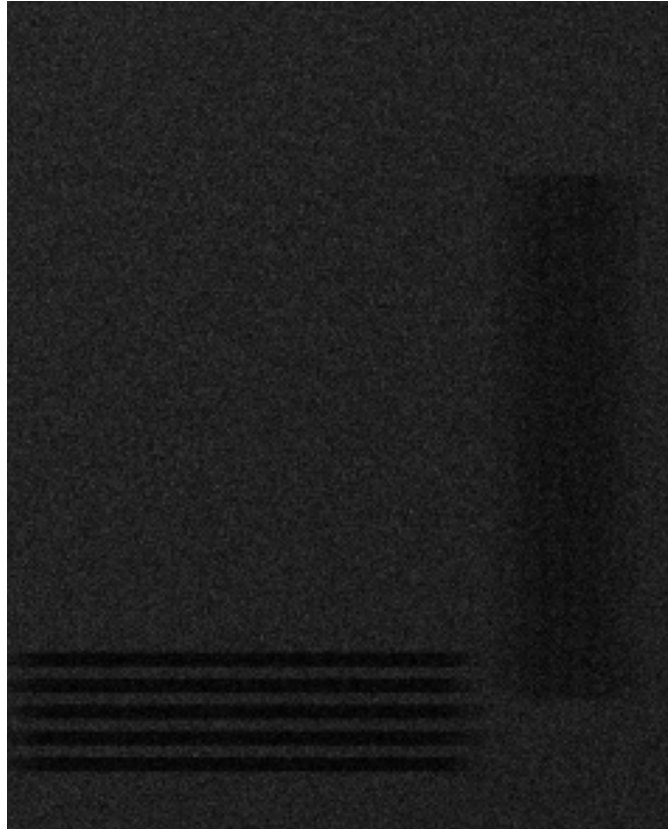


FIGURE 7.9: The simulation of the line pair tool showing the difference between the edges in two directions. The image displays raw, unprocessed data.

systems using MTF and DQE. The contrast, spatial resolution and noise characteristics can be compared using these image quality parameters. Figures 7.10A and 7.10B show the ESF and LSF functions respectively. It can be seen that the ESF of the real X-ray image (continuous) is very similar to that of the simulated image (dashed) in Figure 7.10A, with the edge in the simulation being slightly noisier. The LSF, which is the derivative of the ESF, is also similar in both the real X-ray (continuous) and simulated X-ray (dashed) images, with again the simulation being slightly noisier. The normalised MTF shown in Figure 7.11A is also comparable with the MTF of the real X-ray image (continuous) almost overlapping that of the simulated image (dashed). These results show that the transfer functions of the simulation process are similar to that of the real mammography machine and their contrast and spatial resolution characteristics match. The normalised DQE of the real X-ray image (continuous) and the simulated image (dashed) overlap each other, indicating that the noise modelling of the two systems is also consistent.

A common artefact of slot-scanning X-ray imaging is that the edges perpendicular to the

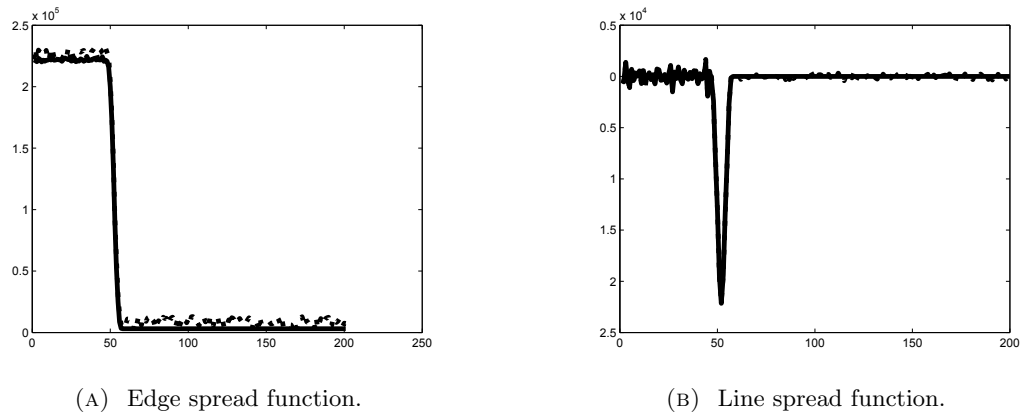


FIGURE 7.10: The edge spread functions (ESF) in (A) and the line spread functions (LSF) in (B) of the real (continuous) and simulated (dashed) X-ray images. These functions are based on experiments done using a 3mm tungsten block and the edge-test method.

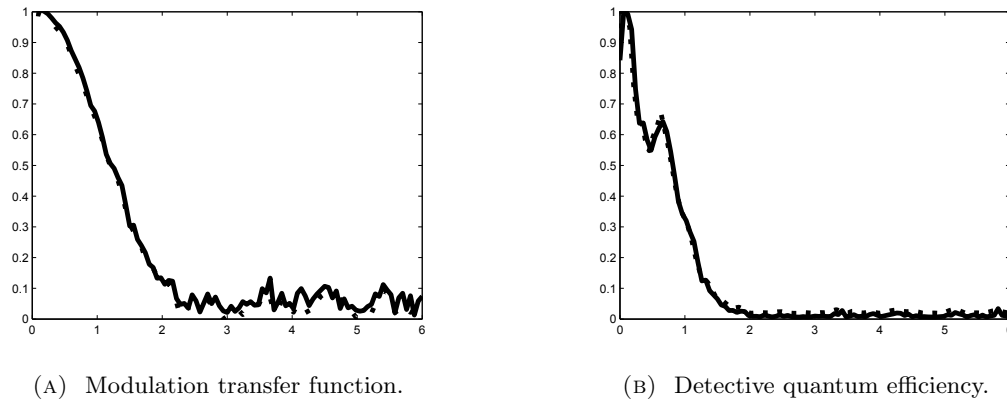


FIGURE 7.11: The modulation transfer functions (MTF) in (A) and the detective quantum efficiencies (DQE) in (B) of the real (continuous) and simulated (dashed) X-ray images. These functions are based on experiments done using a 3mm tungsten block and the edge-test method.

slot direction are sharper than the ones perpendicular to the scan direction. This results in the edge spread functions (ESFs) being different in the slot and scan directions. The line spread functions (LSFs) will also be different for the two directions. Because the edges perpendicular to the slot direction are sharper, the ESF in that direction will have a sharper fall-off compared to the other direction. This results in the LSF being steeper and the MTF being higher. The differences between the MTFs and DQEs in the two directions are minimal but the edges on the X-ray image especially at lower resolutions can be visibly different.

7.5 Discussion

Hussein et al. (2009) modelled a mathematical, tissue-equivalent breast phantom based on the CIRS phantom and simulated it using a linear slot-scanning mammography system. The work done in this thesis extends the model described by Hussein et al. (2009) to three dimensions. This extension not only enables the phantom to be used for digital breast tomosynthesis (as described in the next chapter), but also improves the scatter modelling of the imaging system. The scattered radiation can be modelled for each slot and the different types of scatter can be studied (as shown in Chapter 6). Individual slots are simulated and combined in this thesis, making it easier to study the effects of different methods to combine slots. The effect of slot related parameters like slot width, number of slots and the interval between to slots on the X-ray image quality can be studied.

Bakic et al. (2002) simulated a three-dimensional breast phantom based on a realistic distribution of tissue structures. Parameters controlling the size and shape of the model were used to consistently model images of breast phantoms based on a mammographic imaging process. The compression model described was used to model breast thickness and the images were qualitatively verified using a panel of radiologists and were found to be similar to real X-rays when viewed at a distance of 1m to 2m. In this thesis, the breast phantom modelled is based on a commercially available one, and the size and thickness of the phantom can be modified, enabling the effect of the compression model in (Bakic et al., 2002) to be studied. This thesis also provides a robust and objective validation of the simulated images by comparing image quality using MTF, NPS and DQE to those of a prototype mammography system.

The adjustable geometry and the modular nature of the code system enables the study of mammography system parameters on the final image. The work described in this thesis provides a tool to study the effect of system parameters like source voltage, collimation, filtration and slot width on image quality. It also enables investigations concerning image quality and geometric parameters like breast thickness, imaging geometry and the size of the phantom components.

The use of MTF, NPS and DQE provides an objective method to assess image quality.

Using these metrics, the effect of the change of any parameters on the image quality can be determined. In this way, various parameters can be studied in detail and optimised to improve existing imaging systems or build new ones. Binning is used as a post-processing technique to decrease the resolution of the images. This reduction in resolution in the binned image results in a lower MTF than that of the original image. The noise performance can be improved with binning and the NPS of the binned image is, in some instances, better than that of the original image especially for low frequencies (Samei et al., 1998). The DQE of the binned image will be higher than that of the original image for lower frequencies due to the improvement in NPS. On the other hand, the DQE will have a steeper fall-off making it worse for higher frequencies. The effects of binning can be different for different test cases and binning factors. These effects can be studied using the tool described in this thesis and the appropriate binning factor can be chosen.

7.6 Summary

A three-dimensional, tissue-equivalent breast phantom based on the CIRS phantom is simulated and validated using slot-scanning mammography. The simulated and real images are compared using objective image quality measures MTF, NPS and DQE. The simulation system models the different parameters specific to mammography, like breast thickness and material properties of the breast phantom. The simulation system can be used as a tool for further investigations to improve image quality.

Chapter 8

Simulating digital breast tomosynthesis

The application of the simulation process to digital breast tomosynthesis is presented in this chapter. Experiments were done with a simple test object to simulate DBT data over a large angular range. The simulations were reconstructed using filtered backprojection and the effect of changing the DBT parameters on the reconstructed images was shown. The tissue-equivalent breast phantom defined in Section 7.2 was used to simulate DBT projections over a limited angular range and the simulated data was reconstructed. The parameters used for the simulation of the breast phantom are based on those found in commercially available DBT machines. Section 8.1 discusses the methodology of the simulation of digital breast tomosynthesis and the different parameters used. The results and reconstructions using filtered backprojection are shown in Section 8.2. The results are discussed and compared to previous studies in Section 8.3. Section 8.4 summarises the chapter.

8.1 Simulating digital breast tomosynthesis

A simple rectangular block made of tungsten was used as a test object. Low-resolution X-ray images were simulated for angles ranging from 0 to 180 degrees with respect to the detector (or ± 90 degrees from 90 degrees), at intervals of 2 degrees. The simulation of a simple test object, a block in this case, was used to test system geometry, the accuracy

of the projections and to verify that the dimensions of the object were maintained in all the simulated X-ray images. The simulations were performed at a low pixel resolution. Low resolution simulations can be obtained quickly and are sufficient to image a simple test object. Another advantage of using a simple test object was to generate and test the reconstructions that would be easy to predict so that reconstructions using limited angles, sparse angles and a combination of the two could be studied. The loss of data could be assessed using the reconstructed image.

The mathematical breast phantom used for the mammography simulation was also used for DBT. The 2D projections of the phantom were simulated at different angles, ranging from ± 20 degrees from 90 degrees in intervals of 2 degrees. These values were chosen based on the values used in (Choi et al., 2012) and commercially available DBT machines. The data were simulated in a similar way to the rectangular block data, but the resolution of the projections of the CIRS phantom was 50 microns/pixel. The rectangular block data were simulated to test the geometry of the simulation system, whereas the CIRS phantom data was simulated to replicate a real-life DBT system. Figure 8.1 shows a simple schematic diagram of the DBT system. The angular width or range θ is expressed with respect to the vertical and the angular interval shown as ϕ is the interval between two projections. The number of projections depends on the angular width and interval.

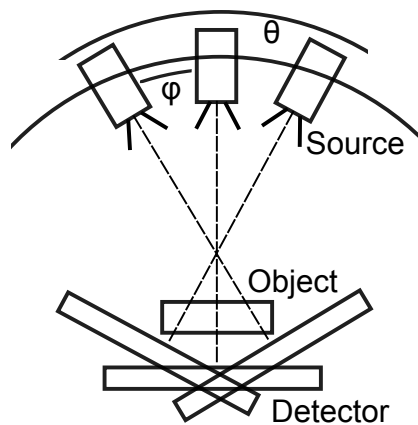


FIGURE 8.1: A simple schematic of the DBT system. The angular width is θ and the angular interval is ϕ . In case of a slot-scanning system, the source is collimated and its projection is made up of many slots, as shown in Figure 4.2.

The filtered back-projection algorithm was used to reconstruct 3D data based on 2D

projections. The back-projection algorithm was based on the inverse radon transform and back projects the angular X-ray image data along the principal axes to produce a 3D reconstruction. The back-projection algorithm was chosen because it uses all the angular data and does not involve predicting or estimating missing data. It is widely used for tomosynthesis reconstruction and is easy to implement. Median filters were used to filter the data before reconstruction because they filter all the data in an unbiased way. Total variation denoising, shown in (Reiser et al., 2006) to be effective for filtration prior to reconstruction of an analytical breast phantom, involves modifying specific parts of the data that are considered unwanted.

Image contrast was used as a measure to compare the simulations and was calculated as the difference between the means of groups of background and foreground pixels, divided by the mean of the background pixels. Corresponding groups of pixels were assessed in all the reconstructed images to keep the contrast calculation consistent.

The orientations of the planar reconstructions are shown in Figure 8.2. The planar reconstructions are named with respect to the detector, with horizontal reconstruction (dashed line) being parallel and vertical reconstruction (dotted line) being perpendicular to the detector. The locations and orientations of both the planar reconstructions are shown in Figure 8.2 in the 3D, top, front and side views. After the 3D reconstruction of the test object, the horizontal and vertical planar slices can be at any depth. The distance from the horizontal slice from the source is known as the depth of the horizontal slice. Horizontal slices are cut through the object at various depths to observe the components of the test objects at various depths.

8.2 Results

A selection of the angular projections of the tungsten block are displayed in Figure 8.3. The depth of the tungsten block is half of its length and width. As the angle of the projection increases from 90 to 180 degrees the size of the projection changes.

The reconstructions of vertical slices through the tungsten block are shown in Figure 8.4. The quality of the reconstructions decreases as the angular interval increases from

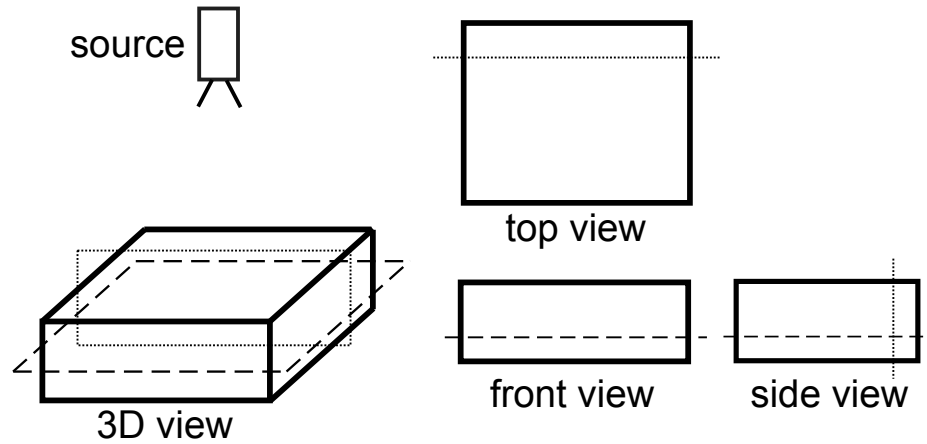


FIGURE 8.2: The horizontal (dashed line) and vertical (dotted line) planar reconstructions shown with respect to the test object and source. The planar reconstructions are named with respect to the detector. The source is shown to provide context to the orientation of the object, and its location is not drawn to scale.

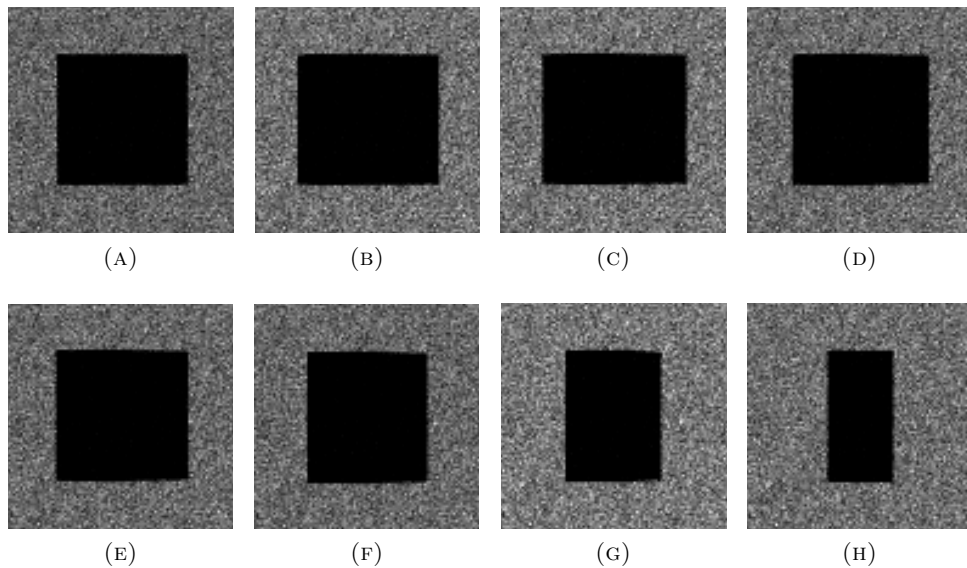


FIGURE 8.3: Some of the angular projections of the tungsten block. Simulations are done from 0 to 180 degrees from the detector. The projections shown in the images are (A) 90, (B) 105, (C) 120, (D) 135, (E) 140, (F) 150, (G) 165 and (H) 180 degrees.

2 degrees in Figure 8.4A to 10 degrees in Figure 8.4C due to the decrease in the number of angular projections used to reconstruct the planar slice. In Figure 8.4A, using an angular interval of 2 degrees, 91 projections are used to reconstruct the planar slice compared to Figure 8.4B in which 37 projections are used and Figure 8.4C in which 19 projections are used. The reconstruction artifacts seen on the edges of the reconstructed slices are periodic.

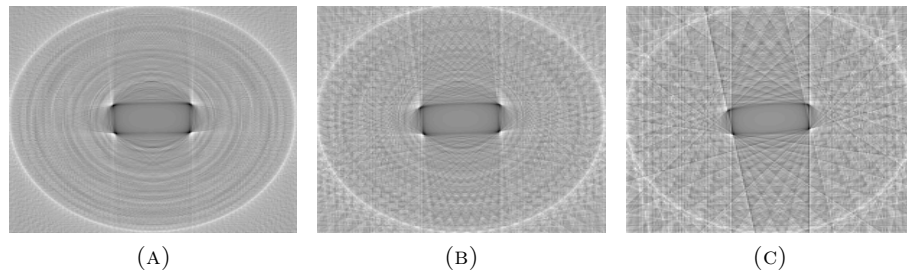


FIGURE 8.4: Reconstructions of vertical slices through the center of the tungsten block. The three reconstructions are performed using data from different angular intervals. The angular range is from 0 to 180 degrees and the intervals are (A) 2, (B) 5 and (C) 10 degrees.

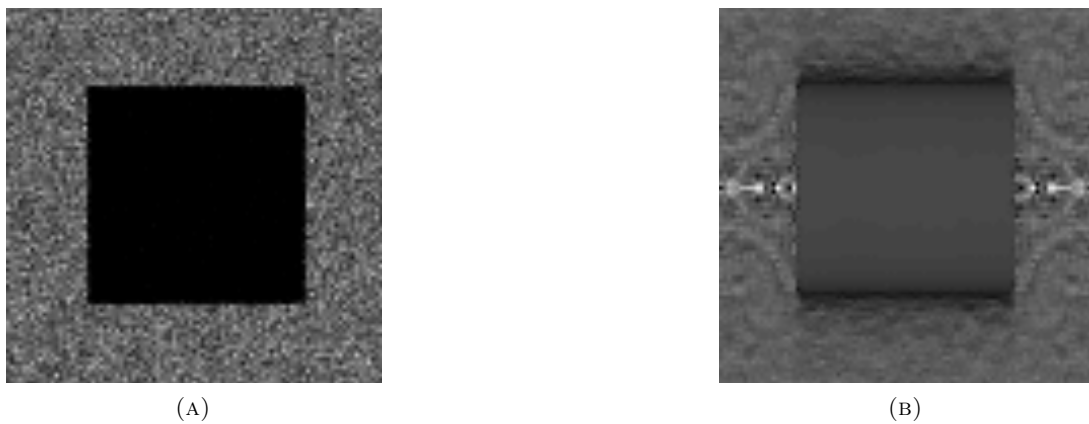


FIGURE 8.5: The top view or 90 degree projection in (A) and a horizontal planar reconstruction using filtered backprojection in (B).

Figure 8.5 compares the horizontal planar reconstruction of the tungsten block in Figure 8.5B to the 90 degree projection in Figure 8.5A. The reconstruction is performed using projections of angular range of 0 to 180 degrees and angular intervals of 2 degrees between projections. These results suggest that the simulation process can be modified to study the effects of DBT variables like angular intervals, number of projections and angular range on the resulting horizontal and vertical reconstructions.

Figure 8.6 shows a selection of angular projections of the breast phantom. Projections are simulated using an angular range from 70 to 110 degrees with respect to the detector and with an angular interval of 2 degrees. The total number of projections is 21. Figure 8.8 shows four reconstructions of the same horizontal planar slice. Figures 8.8A and 8.8C have an angular range from 70 to 110 degrees with respect to the detector and Figures 8.8B and 8.8D have an angular range from 80 to 100 degrees. The angular interval for Figures 8.8A and 8.8B is 2 degrees and for Figures 8.8C and 8.8D

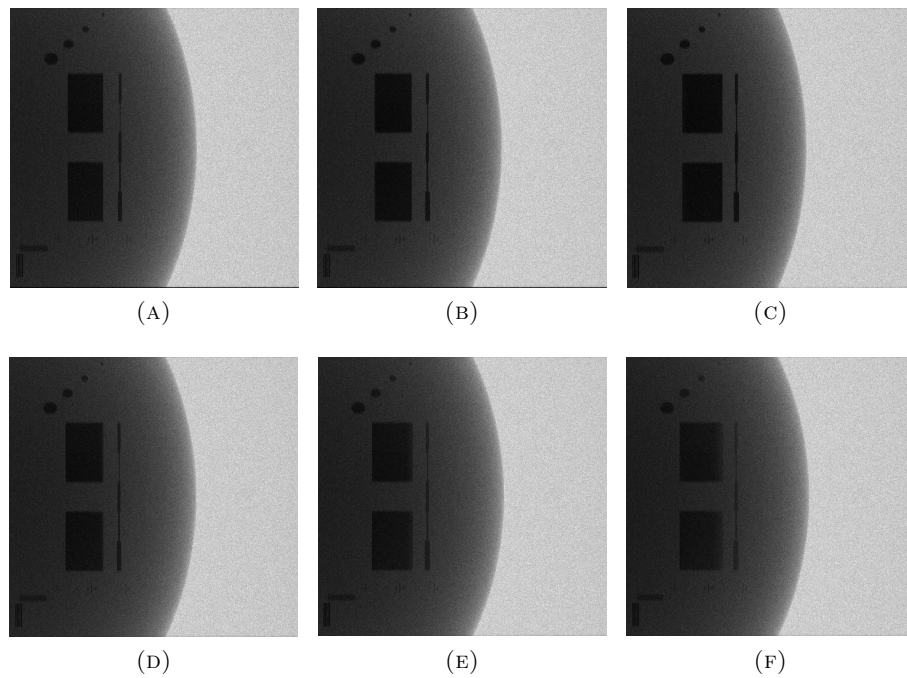


FIGURE 8.6: Projections shown in the images are (A) 92, (B) 98, (C) 104, (D) 88, (E) 82 and (F) 76 degrees with respect to the detector.

is 4 degrees. The number of projections is 21 for Figure 8.8A, 11 for Figures 8.8B and 8.8C and 5 for Figure 8.8D.

Horizontal planar reconstructed slices of the breast phantom at different depths are shown in Figure 8.7. The slice shown in Figure 8.7C is through the center of the breast phantom and shows all the components of the phantom. The slices shown in Figures 8.7A and 8.7B are through the top parts of the object. Some of the components of the objects, like the hemispheric masses for example, are not visible in these figures because they are closer to the center of the object. The outer shell of the phantom is visible in all the images. Components at different depths can be viewed using the horizontal planar reconstructions.

The image contrast measures for the images shown in Figure 8.8 are 204.6 and 199.5 for the angular range of 80 to 100 degrees and angular intervals of 2 and 4 respectively. For the angular range of 70 to 110 degrees, the contrast measures are 290.5 and 269.7 for angular intervals of 2 and 4 respectively. Figure 8.8 shows that the contrast of the reconstructions improves with an increase in angular range and a decrease in angular interval. The best reconstruction result in terms of contrast is shown in Figure 8.8A

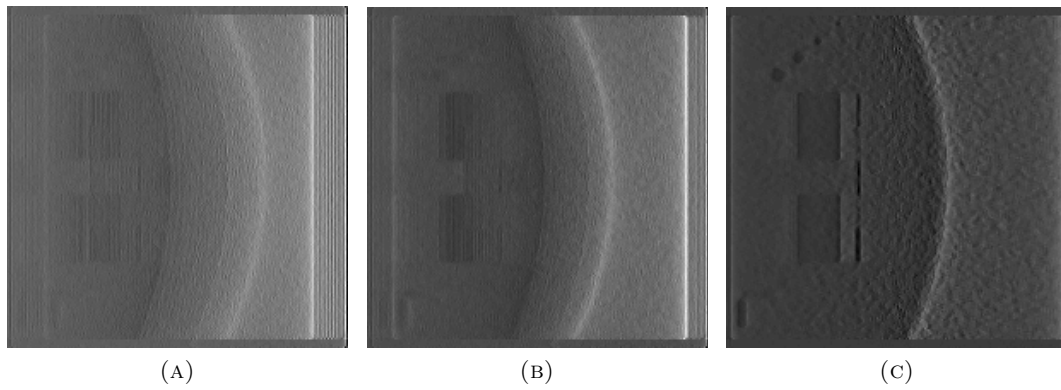


FIGURE 8.7: The horizontal planar slices at different depths.

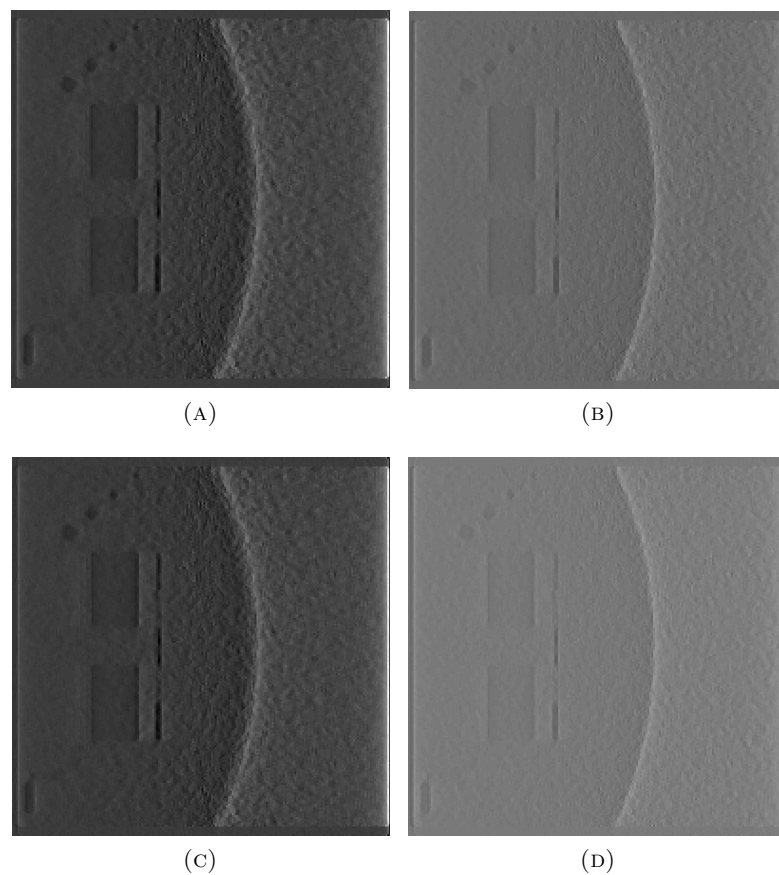


FIGURE 8.8: Horizontal planar reconstructions using filtered backprojection over angular ranges of 70 to 110 degrees in (A) and (C) and 80 to 100 degrees in (B) and (D). The angular intervals used are 2 degrees in (A) and (B) and 4 degrees in (C) and (D).

with 21 projections. The contrast of the reconstructions improves with an increase in the number of projections but the noise in the reconstructed images also increases. These observations are similar to those of Choi et al. (2012), who studied the effect of DBT parameters on the reconstructed images.

8.3 Discussion

Hussein et al. (2009) described a two-dimensional mathematical tissue-equivalent phantom based on the CIRS phantom. In this thesis, that two-dimensional phantom is extended to three-dimensions and is used for the simulation of DBT data. Using this extension, the phantom is rotated at the angles based on the angular range of the simulation. Another extension to the work done by (Hussein et al., 2009) is that individual slots are simulated so the effects of the procedure used to combine the slots can be studied.

Choi et al. (2012) studied the effect of DBT parameters, namely angular range, angular interval and number of projections, on the reconstructed images by building a prototype system and imaging the CIRS phantom using the prototype. Angular projections were acquired at different angles and intervals to study limited-angle tomosynthesis and sparse-angle tomosynthesis. Only tomosynthesis parameters were studied and mammography parameters were kept constant. The simulation tools provided in this thesis remove the need to construct a physical prototype and extend the work done in (Choi et al., 2012) to modify both mammography and tomosynthesis parameters and study the reconstructions resulting from their combinations.

Various DBT reconstruction algorithms may produce images of varying quality in the reconstructed planar slices (Reiser et al., 2006). Parameters of reconstruction algorithms may be varied to yield better vertical resolution to improve the detection of calcifications (Helvie, 2010). The simulation system presented in this thesis may be used to compare DBT reconstruction algorithms and optimise their parameters for particular imaging tasks.

Skaane et al. (2014) compared the effectiveness of using only FFDM versus using FFDM

and DBT together to improve cancer detection and found that FFDM and DBT used together improve detection rates in denser breasts. A study like that of Skaane et al. (2014), which tests the effects of certain parameters on the reconstructed image, can be performed using the simulation system described in this thesis. For example, the density of the breast phantom can be varied using its material properties, and its thickness can also be set using the phantom geometry. Simulations can be performed using different thicknesses and densities and the reconstructions based on these simulations can be studied to test improvement in image quality and detection rates.

Elangovan et al. (2014) proposed the concept of virtual trials and virtual performance as a substitute to large and representative clinical trials of FFDM and DBT. Although Monte Carlo simulation techniques were not used, two simulation chains of modelling tools were presented. These simulation chains were validated using contrast-to-noise ratios and were proposed as a tool for different kinds of breast phantoms. The work done in this thesis can also be used to simulate different breast phantoms, including some with lesions, to act as data for the virtual trials proposed by (Elangovan et al., 2014). The simulation process using Monte Carlo simulations can be used as a third imaging chain to acquire data and simulate lesions and microcalcifications. As noted in (Elangovan et al., 2014), these virtual trials will save time and resources that are needed for clinical trials. An additional advantage of such virtual trials is that the systems can be studied and optimised without patients being exposed to radiation.

8.4 Summary

This chapter describes the simulation of slot-scanning DBT data using a tissue-equivalent breast phantom and investigates the effect of parameters like angular range, angular width and number of projections. Using the simulation process, the data generated can be used to study the effects of DBT parameters on the resulting reconstructions. The simulation process can help in optimizing existing DBT systems and in making design decisions for new DBT systems. To the author's knowledge, there are no simulation systems for slot-scanning DBT.

Chapter 9

Conclusions and Recommendations

This thesis has been devoted to the simulation of slot-scanning X-ray imaging systems involving complex phantoms and geometries, using Monte Carlo methods. The work presented may be summarised as follows:

- PENELOPE and penEasy_Imaging are used to simulate slot-scanning X-ray imaging systems accurately. Each component of the imaging chain can be modified and simulated with the simulation process described in this thesis. All the components of the imaging chain can be simulated, including individual slots on the detector. This makes it easy to study the effects of noise and scatter at each stage.
- Complex phantoms, like the CIRS breast phantom, are used to show that complex geometries and phantoms with different material properties can be simulated. This makes the simulation process flexible and easy-to-use for many applications. The programs included in PENELOPE can be used to visualise the simulation geometry.
- The simulation results are compared to real X-ray images using standard image quality metrics like MTF, NPS and DQE, to validate them. The validation using different metrics proves the accuracy of the simulation process.
- The flexibility of the model in terms of geometry and material properties and the accuracy of the model based on the validation make it a useful tool for simulating

any slot-scanning X-ray imaging system. A full-body X-ray imaging system and a digital mammography system are simulated in this thesis to show the utility of the simulation process.

- Digital Breast Tomosynthesis is simulated using a 3D breast phantom and the effect of DBT parameters on the reconstructed images is shown. The flexibility of the simulation system to accommodate angular projections and different DBT geometries is demonstrated. The simulation system is easy-to-use because the basic subroutines of the system stay the same for full body X-ray simulation, mammography simulation and tomosynthesis simulation. The simulation system can act as a tool for the further study of DBT.
- The simulation of all the aspects of the X-ray imaging system, like the energy spectra, dose and scatter radiation make this a comprehensive tool to study slot-scanning X-ray imaging systems.

The flexibility of the simulation process enables its use to study any slot-scanning X-ray imaging system in detail. It can be used to optimise existing imaging systems and build new ones. Suggestions for future research based on this work are as follows:

- Dual-energy X-rays can be simulated to study dual-energy X-ray imaging systems. The two energies to be used can be optimised based on simulations.
- Performing a dual-energy X-ray in one scan is also an area of research that can be explored. This can be done by periodically changing the X-ray tube voltage or using filters to alter the X-ray energy spectrum.
- The simulation of computed tomography (CT) scans is also of interest. X-ray projections at different angles can be simulated using the simulation process described in this thesis and tomographic data slices can be reconstructed using filtered back-projection or other algorithms. The work done on tomosynthesis in this thesis can be expanded to simulate CT geometries and reconstruct CT data.
- In some cases, the detection of a specific object is desired from the X-ray. Complex and specific phantoms can be built for the simulation of these systems and the dimensions of the object to be detected can be used to decide the parameters of the imaging system.

References

- S. Agostinelli, J. Allison, K. Amako, J. Apostolakis, H. Araujo, and P. Arce. GEANT4—a simulation toolkit. *Nuclear Instruments and Methods in Physics Research Section A: Accelerators, Spectrometers, Detectors and Associated Equipment*, 506(3):250 – 303, 2003.
- S. Agostinelli, J. Allison, K. Amako, J. Apostolakis, H. Araujo, P. Arce, M. Asai, D. Axen, S. Banerjee, G. Barrand, F. Behner, L. Bellagamba, J. Boudreau, L. Broglia, A. Brunengo, H. Burkhardt, S. Chauvie, J. Chuma, R. Chytracsek, G. Cooperman, P. and Dell’Acqua A. Cosmo, G. and Degtyarenko, G. Depaola, D. Dietrich, R. Enami, A. Feliciello, C. Ferguson, H. Fesefeldt, G. Folger, F. Foppiano, A. Forti, S. Garelli, S. Giani, R. Giannitrapani, D. Gibin, J.J. Gomez Cadenas, I. Gonzalez, G. Gracia Abril, G. Greeniaus, W. Greiner, V. Grichine, A. Grossheim, S. Guatelli, P. Gumplinger, R. Hamatsu, K. Hashimoto, H. Hasui, A. Heikkinen, A. Howard, V. Ivanchenko, A. Johnson, F.W. Jones, J. Kallenbach, N. Kanaya, M. Kawabata, Y. Kawabata, M. Kawaguti, S. Kelner, P. Kent, A. Kimura, T. Kodama, R. Kokoulin, M. Kossov, H. Kurashige, E. Lamanna, T. Lampen, V. Lara, V. Lefebure, F. Lei, M. Liendl, W. Lockman, F. Longo, S. Magni, M. Maire, E. Medernach, K. Minamimoto, P. Mora de Freitas, Y. Morita, K. Murakami, M. Nagamatu, R. Nartallo, P. Nieminen, T. Nishimura, K. Ohtsubo, M. Okamura, S. O’Neale, Y. Oohata, K. Paech, J. Perl, A. Pfeiffer, M.G. Pia, F. Ranjard, A. Rybin, S. Sadilov, E. Di Salvo, G. Santin, T. Sasaki, N. Savvas, Y. Sawada, S. Scherer, S. Sei, V. Sirotenko, D. Smith, N. Starkov, H. Stoecker, J. Sulkimo, M. Takahata, S. Tanaka, E. Tcherniaev, E. Safai Tehrani, E. Tropeano, Cherniaev, E. Safai Tehrani, M. Tropeano, P. Truscott, H. Uno, L. Urban, P. Urban, M. Verderi, A. Walkden, W. Wander, H. Weber, J.P. Wellisch, T. Wenaus, D.C. Williams, D. Wright, T. Yamada, H. Yoshida,

- and D. Zschiesche. GEANT4 developments and applications. *Nuclear Science, IEEE Transactions on*, 53(1):270–278, 2006.
- A. Badal, I.S. Kyprianou, D.P. Banh, A. Badano, and J. Sempau. penMesh — Monte Carlo Radiation Transport Simulation in a Triangle Mesh Geometry. *IEEE Transactions on Medical Imaging*, 28(12):1894–1901, 2009.
- A. Badal-Soler. *Development of advanced geometric models and acceleration techniques for Monte Carlo simulation in Medical Physics*. PhD thesis, Universitat Politècnica de Catalunya, 2008.
- P. Bakic, M. Albert, D. Brzakovic, and A. Maidment. Mammogram synthesis using a 3D simulation: Breast tissue model and image acquisition simulation. *Medical Physics*, 29:2131–2139, 2002.
- M. Baptista, S. Di Maria, N. Oliveira, N. Matela, and L. Janeiro. Image quality and dose assessment in digital breast tomosynthesis: A Monte Carlo study. *Radiation Physics and Chemistry*, 104:158–162, 2014.
- G.T. Barnes, R.F. Moreland, M.V. Yester, and D.M. Witten. The scanning grid: a novel and effective bucky movement. *Radiology*, 135(3):765–767, 1980.
- S. Beningfield, H. Potogietter, A. Nicol, S. Van, G. Bowie, E. Hering, and E. Latti. Report on a new type of trauma full body digital X-ray machine. *Emergency Radiology*, 10:23–29, 2003.
- M.J. Berger. Monte Carlo calculation of the penetration and diffusion of fast charged particles. *Methods in computational physics*, (1):135–215, 1963.
- M.J. Berger and S.M. Seltzer. *Monte Carlo Transport of Electrons and Photons*. Plenum, New York, 1988.
- A.F. Bielajew and D.W.O. Rogers. PRESTA: The parameter reduced electron-step transport algorithm for electron Monte Carlo transport. *Nuclear Instruments and Methods in Physics Research Section B: Beam Interactions with Materials and Atoms*, 18(1–6):165 – 181, 1986.
- J.M. Boone. Molybdenum, rhodium, and tungsten anode spectral models using interpolating polynomials with application to mammography. *Medical Physics*, 24(12):1864–1874, 1997.

- J.M. Boone, K.K. Lindfors, V.N. Cooper, and J.A. Seibert. Scatter/primary in mammography: Comprehensive results. *Medical Physics*, 27(10), 2000.
- U. Bottigli, A. Brunetti, B. Golosio, P. Oliva, S. Stumbo, L. Vincze, P. Randaccio, P. Bleuet, A. Simionovici, and A. Somogyi. Voxel-based Monte Carlo simulation of X-ray imaging and spectroscopy experiments. *Spectrochimica Acta Part B: Atomic Spectroscopy*, 59(10):1747–1754, 2004.
- R. Brun, F. Bruyant, F. Maire, A.C. McPherson, and P. Zanarini. GEANT3. *Report DD/EE/841 (CERN, Geneva)*, 1986.
- Y. Choi, H. Park, Y. Kim, H. Kim, and J. Choi. Effect of acquisition parameters on digital breast tomosynthesis: total angular range and number of projection views. *Journal of the Korean Physical Society*, 61(11):1877–1883, 2012.
- K. Cranley, B.J. Gilmore, G.W.A. Fogarty, and L. Deponds. Catalogue of diagnostic X-ray spectra and other data. *IPEM Report No. 78*, (York: IPEM), 1997.
- M. de Villiers and G. de Jager. Detective quantum efficiency of the LODOX system. *SPIE*, 5030:955–960, 2003.
- P. Doyle, C.J. Martin, and D. Gentle. Application of contrast-to-noise ratio in optimizing beam quality for digital chest radiography: comparison of experimental measurements and theoretical simulations. *Physics in Medicine and Biology*, 51:2953–2970, 2006.
- P. Elangovan, L.M. Warren, A. Mackenzie, A. Rashidnasab, O. Diaz, and D.R. Dance. Development and validation of a modelling framework for simulating 2D-mammography and breast tomosynthesis images. *Physics in Medicine and Biology*, 59:4375–4293, 2014.
- T.R. Fewell and R.E. Shuping. *Handbook of Mammographic X-ray Spectra*. HEW Publication (FDA), Rockville, MD, 1978.
- N. Freud, P. Duvauchelle, and D. Babot. Simulation of X-ray NDT imaging techniques. *Proceedings of the 15th World Conference on Non-Destructive Testing*, (15), 2000.
- B. Golosio, T. Schoonjans, A. Brunetti, P. Oliva, and Masala G.L. Monte Carlo simulation of X-ray imaging and spectroscopy experiments using quadric geometry and variance reduction techniques. *Computer Physics Communications*, 183(3):1044–1052, 2014.

- J.A. Halbleib, R.P. Kensek, T.A. Mehlhorn, G.D. Valdez, S.M. Seltzer, and M.J. Berger. ITS version 3.0: the integrated TIGER series of coupled electron/photon Monte Carlo transport codes. *Report SAND91-1634 (Sandia National Laboratories, Albuquerque, NM)*, 1992.
- M.A. Helvie. Digital mammography imaging: Breast tomosynthesis and advanced applications. *Radiologic Clinics of North America*, 48(5):917–929, 2010.
- H. Hirayama, Y. Namito, A.F. Bielajew, S.J. Wilderman, and W.R. Nelson. The EGS5 code system. *SLAC-R-730 and KEK Report 2005-8 (Stanford Linear Accelerator Center, Stanford, CA)*, 2005.
- R. Hunt, D. Dance, P. Bakic, A. Maidment, M. Sandborg, and G. Ullman. Calculation of the properties of digital mammograms using a computer simulation. *Radiation Protection Dosimetry*, 114:395–398, 2005.
- K. Hussein. *Computer models for the design and optimization of a linear slot scanning mammography system*. PhD thesis, University of Cape Town, 2008.
- K. Hussein, C.L. Vaughan, and T.S. Douglas. Modeling, validation and application of a mathematical tissue-equivalent breast phantom for linear slot-scanning digital mammography. *Physics in Medicine and Biology*, 54(6):1533, 2009.
- ICRU. Medical imaging — the assessment of image quality, ICRU report 54. *International Commission on Radiation Units and Measurements ICRU*, 1996.
- International Electrotechnical Commission. Medical electrical equipment — characteristics of digital X-ray imaging devices — Part 1: Determination of detective quantum efficiency. *International Electrotechnical Commission 62220-1*, 2003.
- B.J. Irving. *Radiation dose measurement and prediction for linear slit scanning radiography*. PhD thesis, University of Cape Town, 2008.
- B.J. Irving, G.J. Maree, E.R. Hering, and T.S. Douglas. Radiation dose from a linear slit scanning X-ray machine with full body imaging capabilities. *Radiation Protection Dosimetry*, 130(4):482–489, 2008.
- K. Jing, W. Huda, and J.K. Walker. Scattered radiation in scanning slot mammography. *Medical Physics*, 25(7), 1998.

- A. Karellas and S. Vedantham. Breast cancer imaging: a perspective for the next decade. *Medical Physics*, 5(11):4878–4897, 2008.
- K. Koedooder and H.W. Venema. Filter materials for dose reduction in screen-film radiography. *Physics in Medicine and Biology*, 31:585–600, 1986.
- I.S. Kyprianou, G. Brackman, A. Badal, K.J. Myers, and A. Badano. An efficient depth- and energy-dependent Monte Carlo model for columnar CsI detectors. *Proc. SPIE*, 6913, 2008.
- C.J. Martin, P.F. Sharp, and D.G. Sutton. Measurement of image quality in diagnostic radiology. *Applied Radiation and Isotopes*, 50(1):21 – 38, 1999.
- P.J. Mohajer. Digital X-Ray Radiography, 16 September 2012. URL <http://pjmohajer.hubpages.com/hub/Digital-X-Ray>.
- W.R. Nelson, H. Hirayama, and D.W. Rogers. *The EGS4 code system*. SLAC, Stanford, CA, 1985.
- V. Panettieri, M.A. Duch, N. Jornet, M. Ginjaume, P. Carrasco, A. Badal, X. Ortega, and M. Ribas. Monte Carlo simulation of MOSFET detectors for high-energy photon beams using the PENELOPE code. *Physics in Medicine and Biology*, 52(1):303–316, 2007.
- D.B. Pelowitz. MCNPX User’s Manual Version 2.7.0. *Los Alamos National Laboratory*, pages 158–162, 2011.
- T.D. Perks, R. Dendere, B.J. Irving, T. Hartley, P. Scholtz, A. Lawson, C. Trauernicht, S. Steiner, and T.S. Douglas. Filtration to reduce paediatric dose for a Linear Slot-scanning digital X-ray machine. *Radiation Protection Dosimetry*, pages 1–10, 2014.
- G. Poludniowski, G. Landry, F. DeBlois, P.M. Evans, and F. Verhaegen. SpekCalc: a program to calculate photon spectra from tungsten anode X-ray tubes. *Physics in Medicine and Biology*, 54(19):N433, 2009.
- L.J. Regano and R. Sutton. Radiation dose reduction in diagnostic X-ray procedures. *Physics in Medicine and Biology*, 37:1773–1788, 1992.
- I. Reiser, E. Sidky, and R. Nishikawa. Development of an analytical breast phantom for quantitative comparison of reconstruction algorithms for digital breast tomosynthesis. (lecture notes on computer science vol 4046). 4046:190–196, 2006.

- D.W.O. Rogers, C.M. Ma, G.X. Ding, B. Walters, D. Sheikh-Bagheri, and G.G. Zhang. BEAMnrc users manual. *NRCC Report PIRS- 0509(A)revK*, 2004.
- A. Rose. *Vision: Human and electronic*. Plenum: 21-30, New York, 1973.
- F. Salvat, J.M. Fernández-Varea, and J. Sempau. *PENELOPE-2006: A code system for Monte Carlo simulation of electron and photon transport*. Nuclear Energy Agency (OECD) Issy-les-Moulineaux, 2006.
- E. Samei, M.J. Flynn, and D.A. Reimann. A method for measuring the presampled MTF of digital radiographic systems using an edge test device. *Medical Physics*, 25(1), 1998.
- E. Samei, J.Y. Lo, T.T. Yoshizumi, J.L. Jesneck, J.T. Dobbins, C.E. Floyd, McAdams H.P., and Ravin C.E. Comparative scatter and dose performance of slot-scan and full-field digital chest radiography systems. *Radiology*, 235(3):940–949, 2005.
- M. Scheelke. *System characterization of a full body slit scanning radiography machine: Theory and experiment*. PhD thesis, University of Cape Town, 2005.
- I. Sechopoulos and C. Ghetti. Optimization of tomosynthesis acquisition geometry in digital tomosynthesis of the breast. *Medical Physics*, 36:1199–1207, 2009.
- P. Skaane, B. Osteras, E. Eben, and R. Gullien. Comparison of digital mammography (FFDM) and FFDM plus digital breast tomosynthesis in mammography screening for cancer detection according to breast parenchyma density. *Radiological Society of North America: Scientific Assembly and Annual Meeting*, 2014.
- J.A. Sorenson, L.T. Niklason, and D.F. Knutti. Performance characteristics of improved antiscatter grids. *Medical Physics*, 7(5), 1980.
- K. Stierstorfer and M. Spahn. Self-normalizing method to measure the detective quantum efficiency of a wide range of X-ray detectors. *Medical Physics*, 26(7), 1999.
- C. Trauernicht, T. Rall, T. Perks, G. Maree, E. Hering, and S. Steiner. Effective dose reduction and image preservation after the introduction of a 0.1 mm cu filter into the lodox statscan unit above 110 kvp. *International Radiation Protection Association International Congress*, pages 1894–1901, 2012.

-
- M. Vilches, S. Garcia-Pareja, R. Guerrero, M. Anguiano, and A.M. Lallena. Monte Carlo simulation of the electron transport through thin slabs: A comparative study of PENELOPE, GEANT3, GEANT4, EGSnrc and MCNPX. *Nuclear Instruments and Methods in Physics Research B*, 254:219–230, 2007.
- K. Viswanathan and K. Balasubramaniam. Modeling and simulation schemes in X-ray radiography and computed tomography. *Proceedings of the National Seminar and exhibition on Non- Destructive Evaluation NDE*, 2009.
- S.J. Ye, I.A. Brezovich, P. Pareek, and S.A. Naqvi. Benchmark of PENELOPE code for low-energy photon transport: dose comparisons with MCNP4 and EGS4. *Physics in Medicine and Biology*, 49(3):387–397, 2004.
- L. Zheng-Ming and A. Brahme. An overview of the transport theory of charged particles. *Radiation Physics and Chemistry*, 41:673–703, April 1993.

Appendix A

Program structure for slot-scanning X-ray imaging

This appendix describes the modifications made to the basic PENELOPE and penEasy_Imaging program to adapt it to slot-scanning X-ray imaging and run the code in parallel over the UCT/ICTS High Performance Computing (HPC) Cluster.

A.1 Description of files

This section gives a description of some of the files used in the simulation code. For other file descriptions, the documentation of PENELOPE or penEasy_Imaging must be consulted.

A.1.1 Input energy spectrum file

The energy spectrum file defines the energy and angle dependent spectrum of the X-ray source. Any source can be defined in this file using software packages mentioned in Section 2.1. It is also possible to define different energy spectra for different angular intervals to produce spectra for filtered sources.

A.1.2 Geometry (*.geo) file

The geometry file defines the geometry of the imaging system, using quadric surfaces. The quadric surfaces can be grouped together to form modules. The positions of the X-ray source, the phantom (test object), the filter (if any) and the detector are set using this file. The orientation of each component can be set using polar and azimuthal angles. The materials of the surfaces or modules are also defined using this file. Each module is assigned a material number which corresponds to its location in the material file.

A.1.3 Material (*.mat) data file

The material data is created by means of the auxiliary program MATERIAL (part of the PENELOPE package), which extracts atomic interaction data from the database. The material data file contains the physical information, like chemical composition, mass density and mean excitation energy, for each material in the simulation.

A.1.4 Input (*.in) file

The input file is the main input file for the program, consisting of information on all other files. The number of histories, update intervals and random numbers to start each history are defined at the start of the file. The type of X-ray source (see Section 3.4) is selected and a pointer to the energy spectrum file is included. The names of the geometry and material files are included in this file and then all the tallies are listed. Tallies can be turned 'ON' based on the type of simulation and their properties can be set in this file.

A.1.5 Output (*.out) file

The output file contains information about the simulation. It acts like a report of how the simulation progressed, ended and how long it took. Any errors in the simulation will be reflected in this file. This file has the same structure as the input file, and any errors will cause the simulation to stop. The output file will only have information about the sections which executed successfully, so any errors are easy to track.

A.1.6 Image (*.dat) file

The image file is generated when the image tally is set to 'ON'. This file contains the output X-ray image, based on the input, geometry and material files. See Section 3.7 for more details on how the image is formed.

A.1.7 Dose distribution file

Dose distribution files are generated if the spatial dose distribution tally is set to 'ON' in the input file. This file contains the estimates for absorbed dose over a user-defined volume. The volume is divided into cubic, cylindrical or spherical bins, explained in Section 3.7, and the absorbed dose is written into this file.

A.2 Modifications to the program structure

The basic workings of PENELOPE and penEasy_Imaging have been extended in this thesis to simulate slot-scanning X-ray imaging systems. This section provides an overview of the modifications done to the program structure to achieve slot-scanning simulation using TDI detectors.

The input energy spectrum file is modified for the different X-ray tubes used depending on their kV and mA. The necessary spectra, with or without added filtration, were simulated using Spekcalc (Poludniowski et al., 2009) and the input file was updated accordingly. The *Bremsstrahlung* information and the characteristic K line spikes are included in the file.

The geometry file has information of all the geometric components in the system. Based on the system geometry this file was changed to modify the source-to-detector distances, object-to-detector distances and the location of the collimator. The object that was imaged was also defined in this file. For example, in the case of the aluminium wedge used in Chapter 5, the 5 blocks were defined and their location next to each other were set. Visualisations using *gview2d* were used to ensure the correctness of the geometry. The length of this file varies with the complexity of the object.

Different objects in the geometry file are assigned material numbers. These numbers correspond to the order in which the material properties have been described in the material file. The material file contains physical properties of the materials, e.g. the X-ray attenuation coefficient used in a particular simulation. If many materials are used, then this file will be longer because their physical properties need to be defined in it. The detector material properties are also defined in this file. PENELOPE has a predefined database of materials, but new materials can be synthesised using their chemical compositions.

The input file, one of the most important files, links all the files mentioned above and acts as a driver to the simulation program. The input file has different subsections that point to the input energy spectrum file, the geometry file, the material file and various tally files. The input file was modified differently for different simulations. For slot-scanning, an input file for each slot was created based on the focal spot, slot position and the location of the X-ray source. In a slot-scanning simulation, these variables are changed to mimic the linear scanning nature of the X-ray source across the detector. All the slot images were captured independently and then combined to form the final X-ray image. The order of the different subsections is critical and changing this order will result in runtime errors. This subsection order stays the same between input and output files, making it easier to track errors in the simulation.

The output file provides a report of how the simulation progressed. The different subsections are ordered in the same way as the input file, and if any subsection fails to execute an error flag is raised. The debugging process becomes easier because of the output file. This file contains all the information of the input file but also contains information about the execution of each subsection.

The image file is generated using the image tally described in Section 3.7. In slot-scanning simulation, many image files were generated based on the different input files and were numbered based on the location of the X-ray source. The number of slots, and subsequent image files, depends on the slot width and the gap between two slots in the simulation. All the image files are combined to create a final X-ray image. There are options in the input file to turn scatter radiation on or off. Turning this setting on will

create multiple image files for one slot. These files will have the information on different types of scatter. The scatter radiation files were used for analysis of scatter in Section 6.1.1.

A.3 Parallelisation of the simulation process

The slot-scanning X-ray image simulation is achieved by dividing the detector into different slots and having a different input file for each slot. These individual input files contain the input information unique to each slot, for example the location of the X-ray source. All the input files are executed independently and the slot images are derived. The slot images are combined to form the final image. The independence of the simulation of the different input files enables their parallelisation. With the help of a cluster of computers, many input files can be executed simultaneously and execution times can be reduced substantially. This reduction in execution times enables the simulation of more complex phantoms and high resolution images. Parallelisation also speeds up the correction of any mistakes in the simulation. The simulation times were reduced from a few days to a few hours.

Appendix B

PENELOPE, PENGEOM and penEasy_Imaging programs

The aim of this appendix is to describe the general structure of the PENELOPE, PENGEOM and penEasy_Imaging programs. This will help in understanding the connections between the programs and subroutines and will aid in further modifications to the code. The sequence of these programs is the same as in Appendix A, where these programs are described.

Each file in the simulation process is described using a subsection. Each subsection in this appendix is organised as follows:

- The structure of each file is defined. The structure includes subsections, variables and/or commands that are relevant.
- Details of each subsection are provided with examples. These examples will help in the modification of the files for future simulations.

B.1 Input energy spectrum file

The input energy spectrum file is organised as follows:

- A few commented lines describing the X-ray tube voltage, anode material and filtration.

- The first row of data is the number of angle bins and angular width per bin in degrees.
- The rows of data starting from the second row have two or more columns in them. The first column is the lowest energy value in the energy bin. The second column, and other columns where applicable, contain the emission probability for the corresponding energy/angle bin.
- The last row of data is the highest energy in the final energy bin; negative probabilities mark the end of the data.

An example of a 28 kVp spectrum (Mo anode with 0.03 mm Mo filtration) X-ray source input energy spectrum file is shown in Figure B.1. The columns are rearranged for ease of viewing. The data from the file can be used to plot the X-ray energy spectrum as shown in Figure B.2.

1	180.0	14.5e3	1.48654E+04	24.5e3	1.25592E+03
5.0e3	2.21674E-03	15.0e3	1.52902E+04	25.0e3	1.19056E+03
5.5e3	1.05285E-01	15.5e3	1.54756E+04	25.5e3	1.09671E+03
6.0e3	1.70869E+00	16.0e3	1.56086E+04	26.0e3	9.63145E+02
6.5e3	1.35534E+01	16.5e3	1.55769E+04	26.5e3	7.86799E+02
7.0e3	6.48429E+01	17.0e3	1.54370E+04	27.0e3	5.63630E+02
7.5e3	2.11418E+02	17.5e3	1.13900E+05	27.5e3	3.01879E+02
8.0e3	5.15410E+02	18.0e3	1.47845E+04	28.0e3	-1.0
8.5e3	1.09562E+03	18.5e3	1.43206E+04		
9.0e3	1.91825E+03	19.0e3	1.38478E+04		
9.5e3	3.03572E+03	19.5e3	3.08728E+04		
10.0e3	4.40328E+03	20.0e3	1.38096E+03		
10.5e3	5.86849E+03	20.5e3	1.27359E+03		
11.0e3	7.41386E+03	21.0e3	1.24929E+03		
11.5e3	8.91682E+03	21.5e3	1.24853E+03		
12.0e3	1.03110E+04	22.0e3	1.26053E+03		
12.5e3	1.15799E+04	22.5e3	1.28202E+03		
13.0e3	1.27082E+04	23.0e3	1.29363E+03		
13.5e3	1.35959E+04	23.5e3	1.30070E+03		
14.0e3	1.43068E+04	24.0e3	1.28963E+03		

FIGURE B.1: The columns in the input energy spectrum file for a 28 kVp spectrum (Mo anode with 0.03 mm Mo filtration). The columns are rearranged for ease of viewing.

B.2 Geometry file

The geometry file is subdivided as follows:

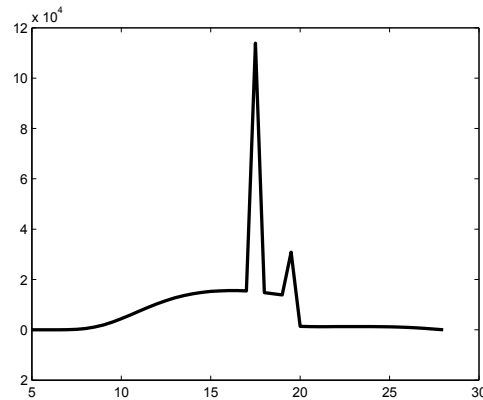


FIGURE B.2: The X-ray energy spectrum generated using the input energy spectrum file for a 28 kVp spectrum (Mo anode with 0.03 mm Mo filtration).

- The very basic element of the file is a surface. Surfaces can be planes, spheres, cylinders or other quadric surfaces shown in Figure 3.1. Each surface is given a number.
- Surfaces can be grouped together using their surface numbers, to form modules. Modules can be assigned materials, using numbers based on the order of appearance of materials in the material file. For example, six planar surfaces can be combined to form a cube module and that can be assigned a material. The locations and angles of the modules can also be set after defining them.
- The geometry file starts with the definition of surfaces, then contains the surface groupings that form different modules, and ends with a listing of all the modules in the file. If a surface is not contained in any module then it is also listed at the end of the file.

Figure B.3 shows the geometric definitions of six planar surfaces that are part of the detector layer. The modular definition of the detector layer is shown in Figure B.4. The detector layer module consists of surfaces with numbers 2011, 2012, 2013, 2014, 2015, 2016, and is assigned material number 4. The X, Y, Z shifts define the position of the module in the geometry and omega, theta and phi are used to change the angles. The module as a whole is assigned the module number 2. The listing of all the modules and surfaces at the end of the geometry file is shown in Figure B.5. The detector layer, module number 2, is included along with other modules and surfaces that have not been assigned to modules. The end of the file is denoted with ‘END’ followed by a set of zeros.


```

PENELOPE (v. 2006) Material data file .....
Material: CESIUM IODIDE (141)
Mass density = 4.51000000E+00 g/cm**3
Number of elements in the molecule = 2
  atomic number = 53, atoms/molecule = 1.00000000E+00
  atomic number = 55, atoms/molecule = 1.00000000E+00
Mean excitation energy = 5.53100000E+02 eV
Number of oscillators = 24 (E/P inelastic model)
  1  8.00000000E+00  0.00000000E+00  1.07383630E+01  0  30
  2  2.00000000E+00  1.10000000E+01  2.03951521E+01  55  30
  3  2.00000000E+00  1.30000000E+01  2.39446879E+01  55  30
  4  2.00000000E+00  1.40000000E+01  2.57269823E+01  53  30
  5  2.00000000E+00  2.30000000E+01  4.18777021E+01  55  30
  6  1.00000000E+01  5.00000000E+01  9.08137814E+01  53  30
  7  1.00000000E+01  7.58000000E+01  1.37427451E+02  55  30
  8  6.00000000E+00  1.23000000E+02  2.22796055E+02  53  30
  9  6.00000000E+00  1.62000000E+02  2.93398607E+02  55  30
 10  2.00000000E+00  1.86000000E+02  3.36830919E+02  53  30
 11  2.00000000E+00  2.31000000E+02  4.18309811E+02  55  30
 12  1.00000000E+01  6.24400000E+02  1.13062216E+03  53  8
 13  1.00000000E+01  7.30400000E+02  1.32252618E+03  55  8
 14  4.00000000E+00  8.75000000E+02  1.58443197E+03  53  7
 15  2.00000000E+00  9.31000000E+02  1.68582841E+03  53  6
 16  4.00000000E+00  9.98000000E+02  1.80715464E+03  55  7
 17  4.00000000E+00  1.06850000E+03  1.93479756E+03  0  5
 18  2.00000000E+00  1.21700000E+03  2.20370601E+03  55  5
 19  4.00000000E+00  4.55700000E+03  8.25166086E+03  53  4
 20  6.00000000E+00  4.95866667E+03  8.97793818E+03  0  3
 21  4.00000000E+00  5.27400000E+03  9.54870868E+03  0  2
 22  2.00000000E+00  5.71300000E+03  1.03449044E+04  55  2
 23  2.00000000E+00  3.31700000E+04  6.00630929E+04  53  1
 24  2.00000000E+00  3.59850000E+04  6.51603979E+04  55  1
Number of shells = 24 (Compton IA model)
  1  8.00000000E+00  0.00000000E+00  1.23813572E+00  0  30
  2  6.00000000E+00  1.26666667E+01  6.24333333E-01  0  30
  3  2.00000000E+00  2.30000000E+01  7.20000000E-01  55  30
  4  1.00000000E+01  5.00000000E+01  1.60200000E-01  53  30
  5  1.00000000E+01  7.58000000E+01  1.44600000E-01  55  30
  6  1.60000000E+01  1.59000000E+02  2.04375000E-01  0  30
  7  6.00000000E+00  6.20000000E+02  5.21000000E-02  53  9
  8  4.00000000E+00  6.31000000E+02  5.15000000E-02  53  8
  9  6.00000000E+00  7.24000000E+02  4.94000000E-02  55  9
 10  4.00000000E+00  7.40000000E+02  4.88000000E-02  55  8
 11  4.00000000E+00  8.75000000E+02  7.74000000E-02  53  7
 12  2.00000000E+00  9.31000000E+02  7.48000000E-02  53  6

```

FIGURE B.6: A part of the material file showing the material properties of Cesium Iodide (CsI).

- Image tally section: this section is used to produce radiographic images based on the detector models. The detector material, model, scatter model, location and resolution is defined in this section.

```
[SECTION CONFIG v.2006-08-01]
1e6          # NO. OF HISTORIES (<1e15)
1e30        # ALLOTTED TIME (s) (+ FOR REAL TIME; - FOR CPU TIME)
100.0       # UPDATE INTERVAL (+ FOR REAL TIME (s) < 50000; - FOR HISTORIES)
314159265   20100902   # RANDOM SEEDS: with 0 0 an external file will be used
[END OF CONFIG SECTION] # (SIGNALS THE END OF THIS SECTION)
#(rngseed.in      ) RANDOM SEEDS FILE NAME (30 characters)
```

FIGURE B.7: The description of the configuration section.

```
[SECTION SOURCE RECTANGULAR BEAM v.2010-09-02]
ON          # STATUS (ON or OFF)
2          # PARTICLE TYPE (1=electron, 2=photon, 3=positron)
energy_spectra_90kVp.dat # NAME OF THE FILE CONTAINING THE ANGLE/ENERGY SPECTRA
5.00 -30.00 0.98        # POINT FOCAL SPOT COORDINATES (cm)
0.00 1.00 0.00         # DIRECTION VECTOR, NO NEED TO NORMALIZE
1.00 8.00 0.00         # POLAR AND AZIMUTHAL APERTURE AND ROLL ANGLE (rect beam tilt) [deg]
[END OF RECTANGULAR BEAM SECTION]
```

FIGURE B.8: The description of the X-ray source section.

```
[SECTION PENGEOM+PENVOX v.2008-06-01]
(box_detector_10x10.geo ) # QUADRICS FILE NAME (30 characters), LEAVE EMPTY IF NONE
(                       ) # VOXELS FILE NAME (30 characters), LEAVE EMPTY IF NONE
2                       # TRANSPARENT QUADRIC MAT (RELEVANT ONLY IF QUAD&VOX)
7                       # GRANULARITY TO SCAN VOXELS (RELEVANT ONLY IF QUAD&VOX)
[END OF GEO SECTION]
```

FIGURE B.9: The description of the PENGEOM section.

```
[SECTION PENELOPE v.2008-02-20]
(air_water_CsI.mat      ) # MATERIAL FILE NAME (30 characters)
3                       # No. OF MATERIALS EXPECTED IN MAT FILE (0 for AUTO)
MAT  EABS(e-)  EABS(ph)  EABS(e+)  C1  C2  WCC  WCR  DSMAX  DESCRIPTION
1    5.0e3    1.00e3    5.0e3    0.03 0.03 5.0e3 1.0e3 1.0e30 Air
2    10.0e3   1.00e3    10.0e3   0.03 0.03 10.0e3 1.0e3 1.0e30 Water
3    51.0e3   51.00e3   51.0e3   0.05 0.05 10.0e3 1.0e3 1.0e30 CsI: absorbs everything (Eabs>Emax_beam)
[END OF PEN SECTION]
```

FIGURE B.10: The description of the material section.

B.5 Image file

The image file starts with a few commented lines that include the variables described in the image tally section. This includes detector model, resolution and location. The file consists of two columns of image data, while scatter radiation files have one column of data. MATLAB programs to read the image and scatter data were written for this thesis project.

एकेक युध्द माझे मी हारलो तरीही
मजला अजिंक्य केले माझ्या पराभवांनी

सुरेश भट